Karlsruher Institut für Technologie
Fakultät für Elektrotechnik und Informationstechnik

ROBUST PHOTOMULTIPLIER TUBE FRONTEND ELECTRONICS AND IN-FIELD CLUSTER NODES FOR THE SOUTHERN WIDE-FIELD GAMMA-RAY OBSERVATORY

Zur Erlangung des akademischen Grades eines

DOKTORS DER INGENIEURWISSENSCHAFTEN (DR.-ING.)

von der KIT-Fakultät für Elektrotechnik und Informationstechnik

des Karlsruher Instituts für Technologie (KIT)

genehmigte

DISSERTATION

von

Fabian Haist, M.Sc.

geboren in Freudenstadt, Deutschland

Tag der mündlichen Prüfung:	19.10.2023
Erstgutachter:	Prof. Dr. Ivan Peric
	Institut für Prozessdatenverarbeitung und Elektronik
Zweitgutachter:	Prof. Dr. Ralph Engel
	Institut für Astroteilchenphysik

DECLARATION OF AUTHORSHIP

I confirm that this thesis is my own work and I have documented all sources and material used. This thesis was not previously presented to another examination board and has not been published.

Fabian Haist / Heidelberg, 24 August 2023

ABSTRACT

In this work an electronics proposal for the full measurement chain of the next-generation ground-based gamma-ray observatory SWGO is elaborated. This project will be based on a km^2-scale array of roughly 6000 water Cherenkov detectors each equipped with multiple photomultiplier tubes (PMTs) as photosensors. SWGO will be built in South America at an altitude of over 4000 m which requires robust electronics and mechanics.

As the main topic of this thesis the development of a remote-controlled multi-channel HV device is described. The so-called PhantomHV system generates high voltage required for the operation of PMTs and shapes their output signal. It has a modular design, making it easy to install and replace system components, especially in the field. This device is evaluated, optimised and prepared for industrial production.

Additionally, a concept for refurbishing already available PMTs for operation in purified water for an engineering array has been developed.

Another major part of this work describes a concept of how to distribute, operate and maintain the electronics in the detector field. An autonomously running environmentally controlled outdoor cabinet is proposed that houses and provides power to the PhantomHV system and readout electronics in the field. Two prototypes have been built, one as a proof of concept and a second destined for a candidate detector site at 4500 m asl in the Peruvian Andes.

ZUSAMMENFASSUNG

Im Zuge dieser Arbeit wird ein mögliches Messkettekonzept für das Gammateilchenexperiment SWGO vorgestellt. Das sich in Planung befindliche Projekt (Southern Wide-field Gamma-ray Observatory) wird sich über ein km^2- Feld erstrecken und aus ca. 6000 Wasser-Tscherenkow-Detektoren bestehen, welche jeweils mit Photomultipliern (PMT) ausgestattet sind. SWGO wird in Südamerika in einer Höhe von über 4000 m errichtet, weshalb die Elektronik und Mechanik sehr robust sein müssen.

Diese Thesis beschreibt die Entwicklung eines mehrkanäligen und über Ethernet steuerbaren Hochspannungsgerätes. Das sogenannte PhantomHV System erzeugt die für die PMTs notwendige Hochspannung und nimmt eine Pulsformung deren Ausgangssignale vor. Durch das modulare Design des Systems wird die Installation und das Austauschen, besonders in rauer Feldumgebung, erleichtert. Dieses Gerät wird evaluiert, optimiert und für eine industriell gefertigte Kleinserie vorbereitet.

Darüber hinaus wurde ein Konzept für die Aufbereitung bereits verfügbarer PMTs für den Betrieb in gereinigtem Wasser für ein mögliches technologisch wegweisendes Vorstufenprojekt entwickelt.

Ein weiterer wichtiger Teil dieser Arbeit beschreibt ein Konzept für die Verteilung, den Betrieb und die Wartung der Messelektronik im Feld. Hierfür wird ein autonomer und klimageregelter Außenschaltschrank, welcher das PhantomHV System und die Ausleseelektronik in Feld mit Strom versorgt, vorgeschlagen. Zwei Prototypen wurden aufgebaut, einer als Konzeptnachweis und ein zweiter für einen potenziellen Projektstandort in den peruanischen Anden auf 4500 m Höhe.

ACKNOWLEDGMENTS

At this spot I would like to thank all people who supported me during the last years. Without the support of a number of people, this work would not have been possible.

First, I would like to thank my referees Ivan Peric and Ralph Engel for their willingness to supervise me. Additionally, I would like to thank Jim Hinton, the director of the division non-thermal astrophysics at the Max Planck Institute for Nuclear Physics in Heidelberg. Without the resources of MPIK and especially those of the Hinton division, successful prototying would not have been possible. Furthermore, the confidence in me and the opportunity to design and build prototypes independently was great.

Fundamentally for this work was the support from my supervisor Felix Werner. I would like to express my deepest sense of gratitude to Felix. His valuable advice, insightful comments and unremitting commitment to share his tremendous knowledge formed the basis of this thesis.

I am also thankful to the people from the electronics department. Here Christian Bauer, Christian Föhr and Thomas Schwab need to be mentioned as a great help with their substantial knowledge in hardware design.

Probably the biggest and by far the most important thanks goes to my whole family. My wife and daughter supported me inexhaustibly during the whole time of the thesis and made it possible for me to do this work.

CONTENTS

1

INTRODUCTION

1.1 COSMIC RAYS AND EXTENSIVE AIR SHOWERS

Cosmic rays are high-energy particles originating in cosmic accelerators in the Milky Way or nearby galaxies. Since these are charged particles, they are deflected by intergalactic magnetic fields. Gamma rays, which also originate in cosmic accelerators are neutral, so they travel in a straight line and thus give us valuable information about the cosmic ray sources and their surroundings. The interaction of cosmic rays or gamma rays with molecules in the atmoshere generate secondary particles. These interact again and again with particles in the atmosphere, producing a shower cascade. Depending on the type of primary particle, the secondary particles and the form of such an *extensive air shower* will be different [1] [2]. The particle interactions produce electromagnetic and hadronic sub-showers, with photons, electrons, and muons constituting the main measurable components on ground. Figure 1 shows the decomposition of an extensive air shower induced by a primary photon (a) and the development of secondary particles for a primary hadronic cosmic ray (b). The majority of *extensive air shower* are hadronic showers, which made up the background events for gamma-ray astronomy. A possible method to identify this background is for example detecting muons as part of hadronic induced showers [3].

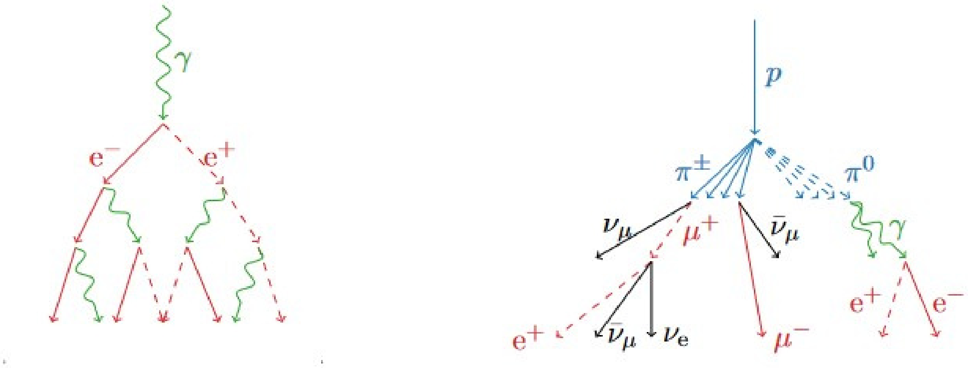

(a) Electromagnetic shower **(b)** Hadronic shower

Figure 1 Particle induced air shower with a primary photon (electromagnetic) (a) and a primary proton (hadronic) (b) [4].

1.2 CHERENKOV RADIATION

When a charged particle is moving through a dielectric medium with a velocity higher than the phase velocity of light in the medium, photons are emitted in the form of Cherenkov light. Figure 2 shows the principle behind Cherenkov radiation. The angle of the produced light cone depends on the velocity and the energy of the particle as well as the refractive index of the medium. For a denser medium, the energy threshold is lower than for a less dense medium such as air. The wavelength of the produced light is in the UV region of the electromagnetic spectrum and partially stretches into the visible range as a blue glow [5].

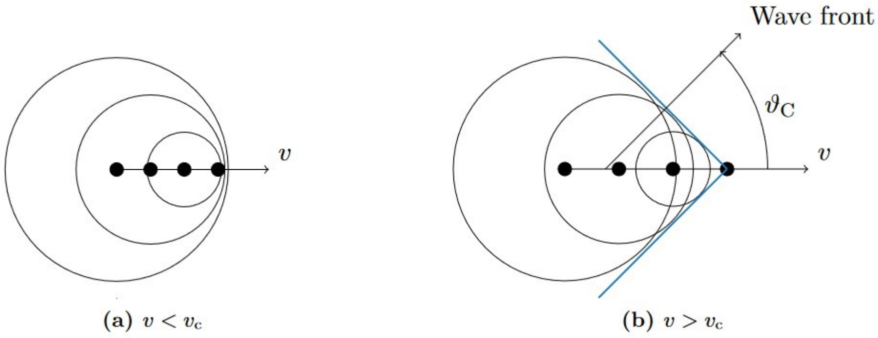

(a) $v < v_c$ (b) $v > v_c$

Figure 2 Principle of Cherenkov radiation. A particle moving through a dielectric medium produces electromagnetic waves. (a) For a particle velocity smaller than the phase speed of light in the medium, the waves will not interfere, while at a higher velocity (b) the waves can interfere constructively. The created wave front moves away from the particle propagation direction under an angle ϑ_C as Cherenkov light [4].

1.3 GAMMA-RAY EXPERIMENTS

In most ground-based gamma-ray experiments imaging atmosheric Cherenkov telescopes (IACTs) or water Cherenkov detectors (WCDs) are used. A Cherenkov telescope can be compared to a high-speed camera that is able to digitise and record images of such particle showers or more precisely the Cherenkov radiation reaching the ground. That means also that only a small portion of the sky can be observed at the same time due to a small field of view. However, this also becomes an advantage when it comes to resolution. The small field of view results in a higher resolution of the observed parts of the sky. A disadvantage is, however, the limited operation time of an imaging atmosheric Cherenkov teleskope. Only during cloudless nights with very little moonlight observations can be made.

Some opposite characteristics apply to water Cherenkov detectors. A large number of these kind of detectors form a detector array and enable a directional and energy reconstruction of air shower particles from the time of arrival and intensity. The principle structure of a water Cherenkov detector consists of a light-tight water volume with a fast light sensor inside to detect Cherenkov light (see Section 1.4). Since it is independent of the ambient

light, a continuous operation is possible. In addition, it is able to observe almost the whole sky above and thus has a large field of view compared to Cherenkov telescopes. The disadvantage, however, is a poor directional resolution. Successful international projects with water Cherenkov detectors are for example HAWC [6], LHAASO [7] and Auger [8].
For the next-generation project SWGO (Southern Wide-field Gamma-ray Observatory) water Cherenkov detectors will be used. It will be the first instrument of its kind in the southern hemisphere. This is the reason for its scientific importance, because it will complement the projects in the northern hemisphere for a more complete research of the galactic plane. Some of the possible areas of research that can be done with this observatory include, among others, Gamma-ray Bursts, Fermi Bubbles or dark matter [9]. The location of SWGO will be in the Andes in South America at a latitude between 10 and 30 degrees south and at an altitude of 4.4 km or higher. The observatory will consist of 6000 detector units distributed over approx. one to two square kilometres. Figure 3 shows different layout options with different fill factors in the inner core and the outer detector area.

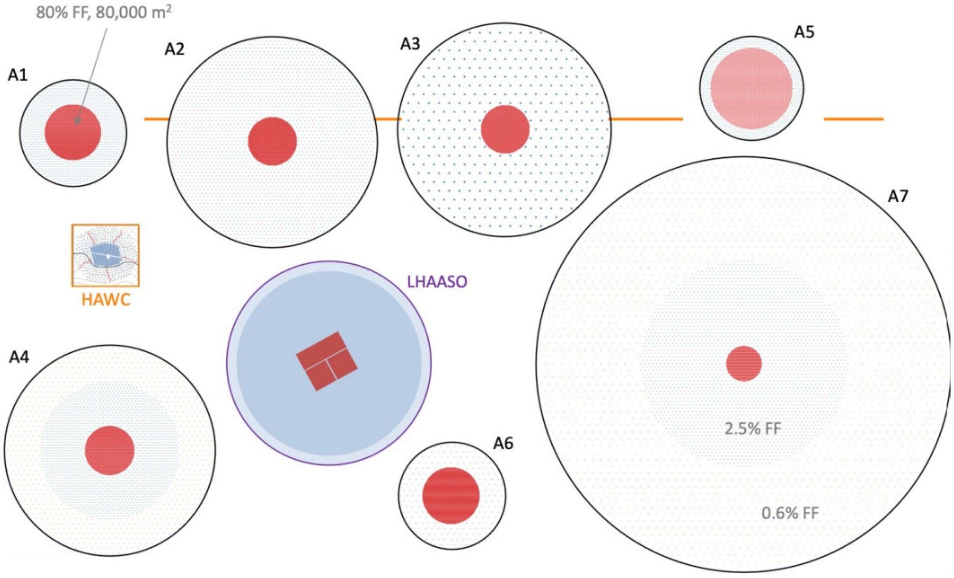

Figure 3 Potential detector layouts of SWGO with different fill factors (FF) in the core and the outer detector area. The total area is approx. 1 up to 2 km². The layouts of the HAWC and LHAASO experiments are shown for comparison [Source MPIK internal].

Different possible options for the water Cherenkov detectors design are proposed. There is the option to build up tanks made of steel or plastic and the option of having bladders floating in an artificial or a natural lake (see Figure 4). All developments and studies described in this thesis are done for SWGO.

SWGO differs from existing air shower detectors in a number of aspects. Compared to the Pierre Auger Observatory, for example, there are some design differences. Even though both experiments are based on water Cherenkov detectors and are located in the Andes. The very different

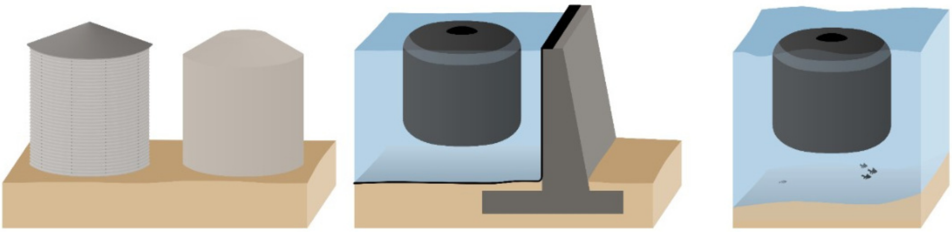

Figure 4 Detector design options for SWGO. Steel or plastic tank (left), bladder in artificial (middle) or natural lake (right) [10].

science goals lead to different design choices. The potential layout of the 6000 SWGO detector units contains a dense filled inner core and a more widely spread outer detector field which covers a total area of one to two square kilometres at an altitude of around 4500 m. In contrast, the Pierre Auger experiment with its 1660 surface detectors is spread over 3000 km² (see Figure 5) at an altitude of less than 2000 m. The widely distributed detector units enable a high observable energy range above 10^{17} eV, whereas SWGO will cover an energy range from 100s of GeV up to the PeV scale (10^{15} eV). The main scientific goal of the Pierre Auger Observatory is the detection of very rare high energy particles whose origin and production is not yet understood. The large area of the observatory increases the probablity of detecting such particles. Generally, a high altitude of an experiment reduces the energy threshold of detectable particles. The maximum measurable energy depends on the density and the area of an experiment. In addition, the design and dimensions of the individual detector units have an impact on the separation of gamma or hadron induced events.

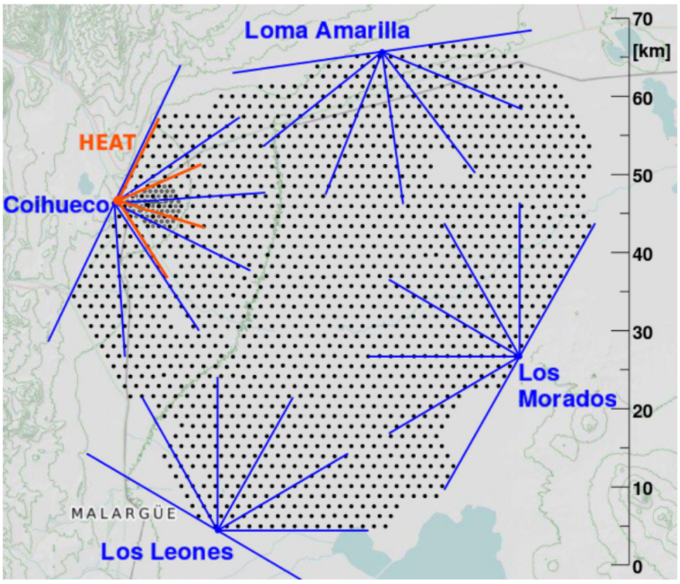

Figure 5 Detector layout of the Pierre Auger Observatory distributed over 3000 km². Each black dot stands for one of the 1660 water Cherenkov detectors. Four fluorescence detectors are placed at the edges of the area [11].

1.4 WATER CHERENKOV DETECTORS

The general design of a water Cherenkov detector (WCD) is based on a light-tight water volume with a photosensor sensitive to Cherenkov light. The water acts as the scintillator, which generates the Cherenkov radiation. The high refractive index of water compared to air maximises the effect and reduces the energy threshold. Figure 6 contains the main parts of a WCD, taking a tank as an example. The colour of the inner wall and the reflectivity associated with it has a large impact on the shape and size of a detector unit. It also has an effect on the expected light profile at the photosensor and its electronics chain. As there is always an effort to determine the nature of an air shower from either gamma or hadron particles, the WCD design will also be optimised in this respect. Some detector concepts shown in Figure 4 have already been used in previous projects. In case of HAWC, steel tanks with one light-tight bladder inside have been used. For the Pierre Auger Observatory, plasic tanks have been used for the surface detector stations. For the most recently completed project, called LHAASO, the main detector array consists of a large artificially created pool with curtain-like separation and a roof for obtaining single detector cells. This shows that there are many different technical implementations, which serve as inspiration bases for potential SWGO designs. A quite new study mostly done at MPIK (Max Planck Institute for Nuclear Physics in Heidelberg) deals with the concept of a two-cell detector unit. The so-called double-layered water Cherenkov detector contains a higher top cell for detecting mainly electromagnetic showers and a shallow bottom cell for mostly detecting muons from hadronic showers. This is based on the fact that mouns go through both cells while other particles leave their energy mostly in the upper cell. [12] For both cells a separate photodetector is required. Some parts of this work are developed and designed based on this proposal. The idea for a double PMT structure derives from this concept and is described in Section 5.4.

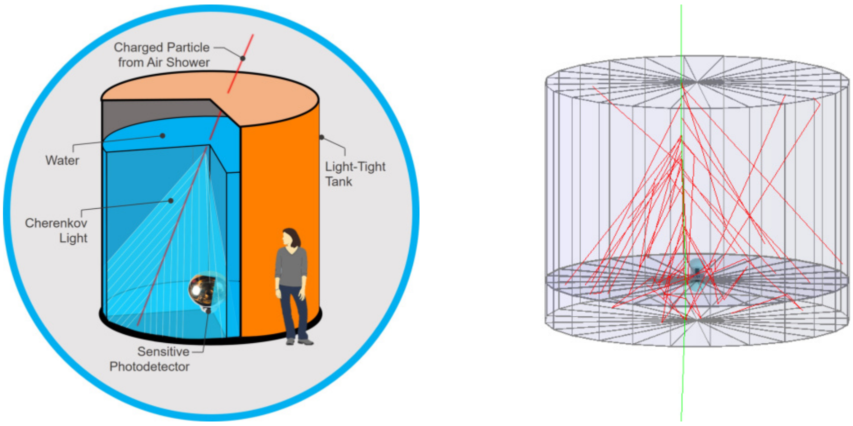

Figure 6 *Left:* General drawing of a water Cherenkov detector. *Right:* Simulated Cherenkov light in a double-layered WCD

1.5 PHOTOMULTIPLIER TUBES

1.5.1 *Principles of Photomultiplier Tubes*

Many different types of photosensors with different technologies are available nowadays. But when it comes to the precise measurement of little light and fast response, especially in science, photomultiplier tubes (PMTs) often come into play. The basic principle is based on the external photoelectric effect. In this phenomenon, electrons are emitted from the surface of metal or semiconductors placed in vacuum. Light with sufficient energy hitting this surface can strike the electrons out. The general construction of a PMT is shown in Figure 7. The light is entering the glass tube from the left side and hitting the photocathode. Photoelectrons are striked out and are accellerated to the first dynode due to an electic field. The electrons are focused to the first dynode by a focusing electrode to increase the probablity of hitting it. At the first dynode the photoelectron strikes out multiple secondary electrons. This process is repeated along the following dynodes because of electric fields between them. After all multiplication steps the secondary electrons are collected at the anode. From there the electron current is output to an external circuit. By this cascade process an amplification of up to approx. 10^8 is reached. The required electric field is generated by applying a voltage in the order of 1–2 kV between the photocathode and the anode. Since the energy of the light is inversely proportional to the wavelength, the materials of the glass, the cathode and the dynodes must be perfectly matched to each other and the application itself. This allows a more efficient measurement.

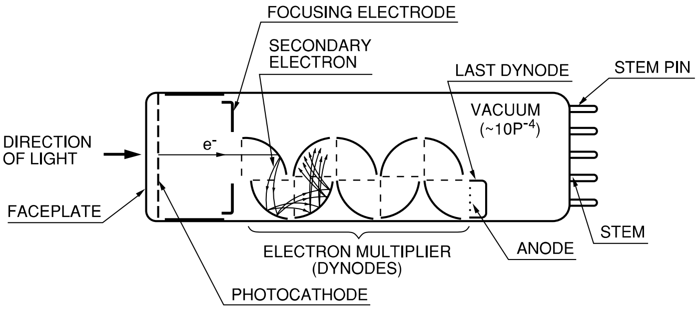

Figure 7 Construction of a photomultiplier tube [13].

1.5.2 *Operating Methods*

The working principle of PMTs is based on electric fields which accelerate electrons in vacuum. For the PMT operation a voltage gradient is set up between the photocathode, the focusing electrode, the dynodes and the anode. The simplest way is to apply a voltage-divider circuit built with resistors (see Figure 8).

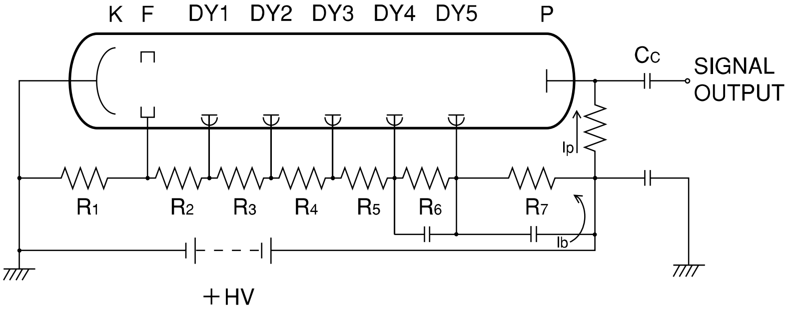

Figure 8 Schematic diagram of a voltage divider circuit with grounded cathode [13].

In practice, a high voltage from 500 to 3000 V is usually applied across the photocathode and the anode with a total voltage-divider resistance of several Mohms.

There are two different techniques to connect the high voltage to the voltage divider. One is to ground the anode and apply a large negative voltage to the cathode. This makes it easy to connect external circuits to the anode without a potential voltage difference. As soon as grounded scintillator medium or metal holder are close to the entry window of the PMT and thus close to the photocathode, the polarity of the high voltage should be changed. A small current could otherwise flow through the glass material due to its slight conductivity and damage the photocathode. To avoid this phenomenon, the second method is to ground the photocathode while the anode is applied to positive high voltage (see Figure 8). This requires AC coupling of the anode signal to obtain the PMT signal but has the big advantage that the photocathode is less vulnerable to external influences. Especially for the applications of water Cherenkov detectors a grounded cathode is a great benefit. For a remote operation of PMTs like in such a detector unit, one coaxial cable is sufficient to provide high voltage and transmit the PMT signal. Since this is connected to the anode, a separation of high voltage and PMT signal can be done on the readout side. The described approach with a base circuit containing a voltage divider with external power supply is called passive base design. This is the technique applied for the electronics concept of this work.

A completely different approach of powering a PMT is with a so-called active base. In this design, a Cockcroft-Walton voltage multiplier circuit provides the voltages across the PMT dynodes. The principle behind this kind of circuit is an AC or pulsed DC voltage which puts charge into a cascade of diodes and capacitors. For each stage of the cascade the voltage gets increased by the amplitude of the initial input voltage. Connecting different stages of the cascade to the different dynodes of a PMT leads to the required voltage gradient along the PMT. This approach has the advantage of a low power consumption because of the high resistance of a PMT. Compared to the voltage divider built with resistors where a constant quiescent current is flowing, with the Cockcroft-Walton solution almost no current is flowing. The disadvantage, however, is that active components are used on the PMT base circuit. Since the PMT would be under water in a WCD, the access to it is difficult or impossible. Hence the issue of reliability plays a major role. The approach with an active base is being investigated by another institute in the SWGO collaboration.

1.5.3 *Characteristics of Photomultiplier Tubes*

Photomultiplier tubes are highly complex devices with various characteristics. The most common and for this work mainly relevant ones are described in the following section.

- **Gain**: The ratio of the anode current and photoelectron current emitted from the photocathode is the gain (current amplification) of a PMT. It increases with increasing supply voltage until the saturation of the PMT is reached. For large area PMTs like the Hamamatsu R5912-100 the typical gain of 10^7 is achieved at a supply voltage of 1500 V.

- **Linearity**: It describes the linear relationship between the number of incident photons and the number of electrons collected at the anode (charge linearity). With a too large amount of incident light, the output signal begins to deviate from the ideal linearity. In pulse mode operation this is mainly caused by the space charge effect and the used voltage divider. The space charge can influence the trajectories of the electrons predominantly at the last dynodes due to saturation. Collection losses of electrons on the way to the anode can be the result. A high electric field, especially at the last dynodes, will help to reduce this effect. This can be achieved by a tapered voltage divider ratio. Additionaly, the structure of the dynodes and the anode are a determining factor.

- **Quantum efficiency**: The ratio of emitted photoelectrons from the cathode and incident photons is described as the quantum efficiency (QE). It is usually expressed as a percentage and depends on the photon wavelength and the material of the cathode. In most cases the QE is around 25 % but for so-called high QE models it goes up to around 35 %.

- **Transit time (spread)**: The time a PMT signal needs from the arrival of a photon at the photocathode to the output of an electrical signal at the anode is called transit time. Depending on the shape, size, operating voltage of the PMT and the trajectory influenced by these, the transit time has some jitter, the so-called transit time spread (TTS). It is typically given as the FWHM (Full Width at Half Maximum) of the probablity density function of the arrival times. For the Hamamatsu R5912 the TTS is given with 2–3 ns.

- **Afterpulsing / Pre and late Pulses**: Afterpulses occur in the wake of real signal pulses and have two main causes. There is the luminous reactions, where light is emitted by dynodes due to electron bombardment. These kind of afterpulses occur several nanoseconds to several tens of nanoseconds after the signal pulse. The second cause is the ionization of residual gases in the PMT and the positive ions generated by this. These ions return to the photocathode and produce photoelectrons which result in afterpulses. The time scale of this type of spurious pulses is usually in the order of several hundred nanoseconds to over a few microseconds. Apart from this, there are pre and late pulses in a PMT. These are also called weakly amplified photoelectrons e.g. they miss the first dynode and hit directly the second one and thus generate less secondary emission but reach the anode earlier. In case of late pulses a photoelectron may be backscattered towards the cathode, without any interaction at the first dyode, and gets accellerated by the electric field for a second hit. The time scale of the delay until the second hit at the first dynode is in the range of tens of nanoseconds. The deviation of the ideal process of secondary emission and trajectory leads to a lower charge at the anode and thus a lower amplitude and a variance in the time of arrival for the affected pulses (see Figure 9)[13][14]. The timing distribution of the shown pulses was measured as part of this work. It indicates the prompt pulses (green region) tend to have a higher amplitude compared to the late pulses (purple region). The time delay of the late pulses is measured about 40 ns. This characteristic is important for the pulse reconstruction described in Section. 4.2.1.

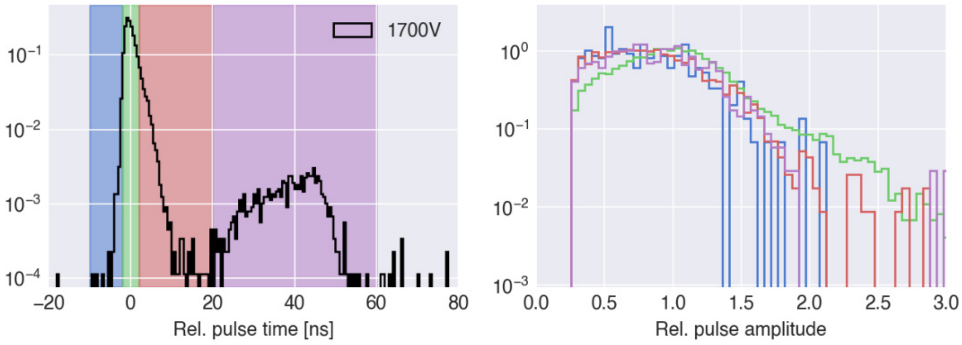

Figure 9 *Left:* Low-illumination pulse time distribution at 1700 V for the PMT R5912. The time delay between prompt and late pulses is about 40 ns. *Right:* Illustration of the slightly different amplitude spectra (normalised to the common median) in the coloured timing regions. The average illumination level was ~0.2 p.e., thus a small amount of multi-p.e. events are expected to be included, mostly in the green region.

- **Dark counts**: Even when a PMT is operated in total darkness, it still produces some short pulses similar to photoelectric pulses. These so-called dark counts are mainly caused by thermoionic emissions. The signal produced by the cathode and its thermal properties is similar to single photoelectrons and depends on the material of the cathode and the temperature. A typical dark count rate for large area PMTs like 8 or 10 inch ones is given with 4–8 kHz. After a PMT is beeing exposed to ambient light, the cathode will be excited and cause an even much higher dark count rate. This requires a cool-down period of usually several hours to recover.

2

MEASUREMENT CHAIN OF WATER CHERENKOV DETECTORS

2.1 SYSTEM COMPONENTS

The general measurement chain of a water Cherenkov detector includes a photosensor, cabling, power supply for the photosensor, digitiser and a timing system for time synchronisation across the detector array. This section describes the front-end system and does not include the network and data handling with its computing system.

Depending on the front-end structure of the system and the technology used, different components are installed and built in at different places. For the described project SWGO, there are two general approaches of opperating PMTs and readout envisaged as possible options. The two main arrangements (A and B) are shown in Figure 10. The third option is an advanced solution for the active base with integrated digitiser and is mentioned for completeness.

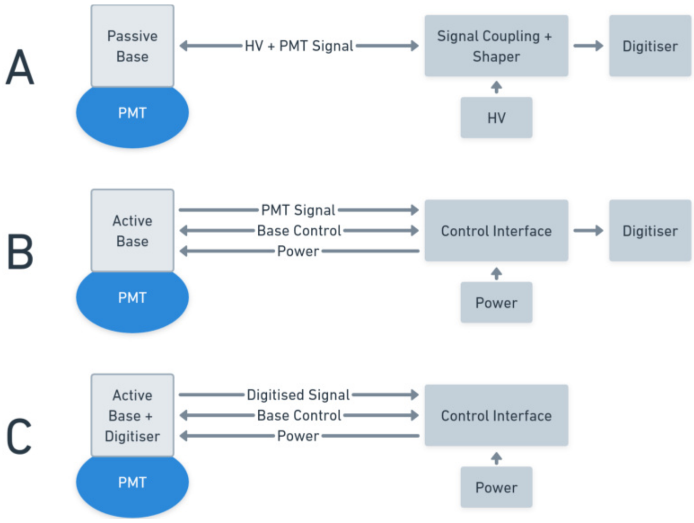

Figure 10 General scheme of a measurement chain with passive base design (*A*), active base design (*B*) and advanced active base with integrated digitiser (*C*).

The passive-base option (A) has the high voltage and the PMT signal on the same coaxial cable and has only passive components for the voltage divider on the base. Remotely a power supply, a coupling unit to separate signal from HV, and a digitiser are placed. In Section. 5.1 the design and a reliability analysis of a passive PMT base is described.

For the active base option (B) a connection for power, communication, and the PMT signal is required. Depending on the design of this solution, it may result in two cables being connected to the PMT. Remotely a power supply, a control unit for the communication with the base, and a digitiser are required. The concerns about this solution are due to the active components on the circuit being neither accessible nor replaceable. This requires especially a reliable and long-lasting electronics design with extensive testing to be considered for possible deployment.

2.2 FUNCTIONALITY OF THE PASSIVE BASE SOLUTION

The decision for developing a passive base solution was motivated by the high level of modularity due to discrete components, the simplicity of the less accessible parts, and the fact that this technique has been common practice in the past for different projects. In addition, there is a large amount of recovered passive-base PMTs from previous projects available (see Chapter 5). These units could be reused in combination with the electronics developed for this work and described in the following. Figure 11 shows the schematic of the measurement chain with a PhantomHV system and a passive base PMT. It includes a digitiser which receives a clock signal for the synchronisation of the detector units across the observatory. The data stream of the digitised PMT signal passes through the network switch on to the server via fibre connection.

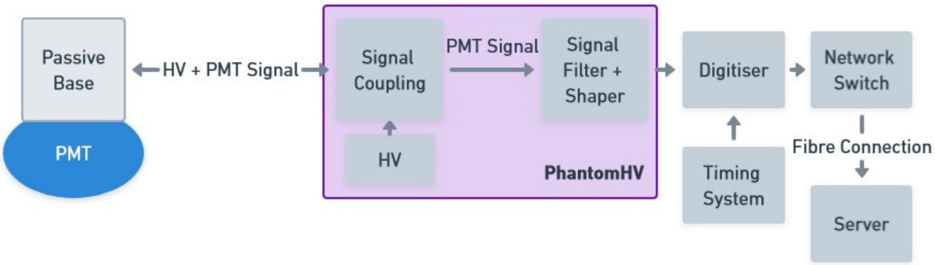

Figure 11 Schematic of the proposed measurement chain with focus on the developed PhantomHV System. It handles one passive base PMT per PhantomHV channel and has a number of options for adjusting and filtering the signal.

Figure 12 shows a photo of the measurement chain with already available components. The main part of this measurement chain is the newly developed PhantomHV system for providing HV and actively shaping the separated PMT signal. This device is a key component of this thesis and is described in detail in Chapter 3. The connected PMT R5912-100 is bought with a waterproof encapsulation from Hamamatsu. The digitiser makes use of the in-house developed high-speed ADC system called FlashCam.

FlashCam is a 24-channel $250\,\mathrm{MS\,s^{-1}}$ 12-bit ADC system (see Figure 13) which is used in several projects with thousands of channels. The FlashCam system is an FPGA-based readout system which features a versatile ADC input stage. Each of the ADC inputs is equipped with an ADC driver which

Figure 12 Measurement chain with a Hamamatsu PMT R5912-100, a PhantomHV System, a 24-channel 250 $\mathrm{MS\,s^{-1}}$ 12-bit ADC (FlashCam), a standard 10 GbE network switch, and a commercial White Rabbit slave for sub-nanosecond clock synchronisation.

can add a configurable offset voltage to the input signal for adapting it to the common mode voltage of the FlashCam system. The input common mode voltage range of the ADC driver is theoretically 0.3–2.8 V which leads to a practical usable range of 1.5 to 2 V due to the voltage swing of the differential input signal. This wide input range allows the use of signal sources like the PhantomHV system. The analogue interface to the FlashCam readout is done differentially with one RJ45 connector for 4 ADC channels [15].

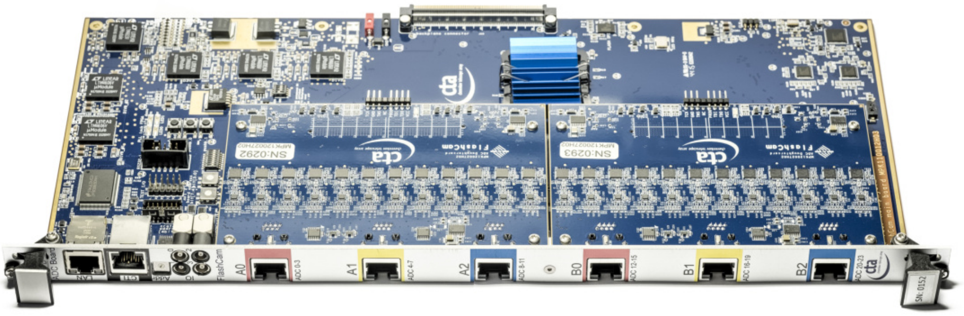

Figure 13 FlashCam readout electronics (9 RU) with 24-channels, 12-bit / 250 $\mathrm{MS\,s^{-1}}$ digitiser.

3

PHANTOMHV SYSTEM

3.1 SYSTEM COMPONENTS

PhantomHV has been conceived as a remotely controlled, modular multichannel high-voltage supply with active signal shaping. One 3 RU (rack unit) 19-inch unit can power up to 24 PMTs and actively shape their output signals. The newly developed system consists of a backplane, the Master module and up to 8 independent three-channel Pick-off modules (see Figure 14). This system has been developed as the main component of this work.

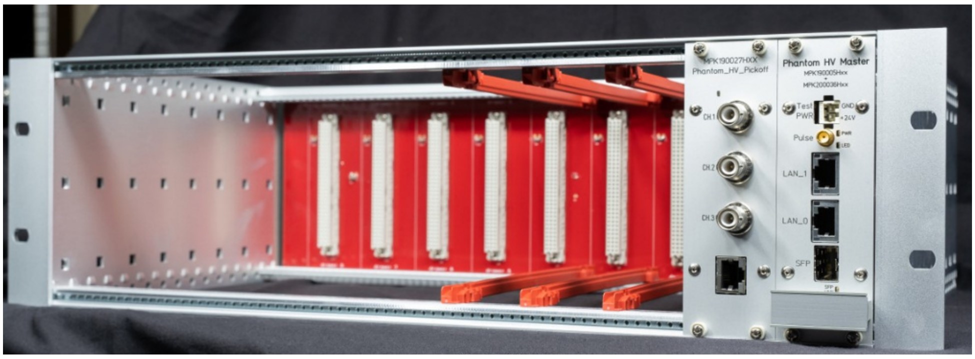

Figure 14 PhantomHV System with Pick-off and Master module in a 19-inch crate with backplane.

The Master module is based on an existing in-house developed multipurpose device called GECCO (see Figure 15). Equipped with a fiber and Ethernet connection, a microcontroller and several freely configurable IOs, the device is applicable for this purpose. It provides a point-to-point SPI connection to each of the Pick-off modules. The backplane is the connecting piece between the master and each of the Pick-off modules. It transmits supply voltage along with control signals for enabling power and measuring the current of each Pick-off module.

Due to the target region being in an earthquake zone, robust DIN connectors are used for each of the cassettes. In addition, the connectors make the cassettes hot-pluggable, because of some leading contacts which first make electrical contact to earth potential. In case of maintenance work, this aspect has the advantage that the units can be changed without switching off the system.

Moreover, there is protection against ESD (electrostatic discharge) due to the defined earth potential of the enclosure when removing or inserting units. The Pick-off module as well as the Master module are built into closed cassettes (see Figure 15). This should allow easy replacement with minimal cabling work, which is helpful for working at high altitude. In addition, it shields the high voltage components from being touched. The printed circuit boards (PCBs) are stabilised by grooves in the side panels of the cassettes. The cover plate at the top and bottom is perforated to allow cooling via forced convection: with approx. 3 W per cartridge the power density is sufficiently low such that several stacked 3 RU units can be cooled by a single 19-inch fan tray while still maintaining an acceptable temperature gradient. For the Master module the GECCO board is placed on a daughter card which fits the size of the cassettes and connects to the backplane. The estimated cost of the PhantomHV system per photodetector channel including HV generator is listed in Table 1.

Figure 15 *Left:* Front panel of the PhantomHV System. *Right:* Inhouse developed multi-purpose device called GECCO that is used as the Master module.

Element	**Procurement Costs**
2 kV DC/DC converter	130 €
Phantom HV module	75 €
Master module	15 €
Backplane	10 €
Crate	2 €
Total	**232 €**

Table 1 Summary of cost estimation for the PhantomHV system, including the rack unit for control and monitoring via Ethernet. Costs are given *per photodetector channel* and are based on small-quantity orders from 2022.

3.2 PHANTOMHV PICK-OFF

3.2.1 *Description of the Structure*

The PhantomHV Pick-off module can provide HV and shape output signals from three PMTs. In Figure 16 the assembled PCB inside of an opened cassette can be seen. The SHV connector in the front panel connects the coaxial cable of the PMT with the coupling circuit on the PCB. There the PMT signal is separated from the HV by using a capacitor in series. With the following fully-differential opamp the signal gets shaped before it is routed to the RJ45 connecter. Additional footprints for potential components are foreseen for attenuators and filters as signal shaping options. This allows further changes of the signal shaping. The RJ45 connector has 8 pins, although just 6 of them are used to transmit the three differential output signals of the board. The one separated pin pair of the connector is not used to minimize the potential crosstalk between the channels. Three silver HV generator modules from ISEG are soldered to the middle of the PCB. Further description of the HV generator modules can be found in chapter 3.3. Each HV output is filtered with a total of three RC low-pass filters in series implemented with HV capacitors. Even though the maximum operational voltage of the Pick-off module is 2 kV, all HV components have been chosen with a voltage range of 3 kV to have a safety buffer. In the upper right part of the PCB in Figure 16 the power supply with a DC-DC switcher, the microcontroller and the components for controlling and monitoring are placed. The DIN connector used for connecting the Pick-off module to the backplane has 64 pins, while the majority of them are tied to ground potential.

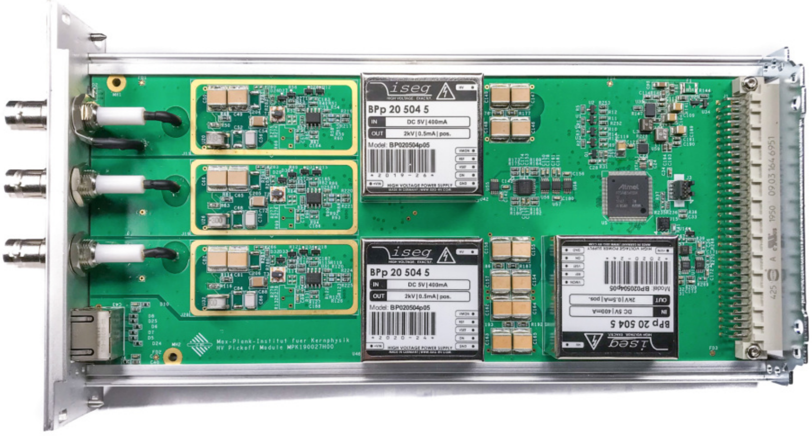

Figure 16 PhantomHV Pick-off module with 3 separately powered HV channels.

3.2.2 *Operation and Monitoring*

The PhantomHV system is addressed via Ethernet through the Master module. From there the individual commands are distributed to the respective cassette via SPI. Each PhantomHV Pick-off module is connected in a point-to-point SPI connection to the Master module. A command-line interface (CLI) is used for control and monitoring. A set of commands are required to prepare the PhantomHV system for operation. The initial step includes the firmware booting of the Master and the Pick-off module. From there on, the individual channels can be enabled and the HV set to the desired value. The common mode voltage of the signal shaper opamps can be set per drawer for all three channels combined between 0–2.5 V by the installed DAC. It is possible to flash the boot firmware ("golden code") as well as the application firmware via Ethernet. This allows a remote update of the firmware without being physically present. In addition to the 24 V power supply, also a separate 24 V interlock signal is necessary. This safety feature allows to include e.g. emergency stops, door contacts or other safety devices to enable the HV output of the PhantomHV Pick-off only if a safe condition is given.

A key feature of the PhantomHV system is the control over every single PMT channel. That includes the option of switching and setting the HV in a range of 500–2000 V. Any change in the HV output value is limited by a programmed slewing rate of $\sim$65 V/s to keep the current flow low. The HV modules are equipped with a monitoring output signal from 0–2.5 V. This is proportional to the HV output voltage of 0–2000 V. This monitoring voltage is read out by an ADC of the onboard microcontroller. The current of the whole PCB is measured with a shunt resistor in the 24 V supply voltage path. For each of the HV generator modules only the primary current at the 5 V supply voltage is measured. This is a compromise to avoid a significantly more complex and expensive current monitoring circuit on the secondary high-voltage side. A consequence of this is that the efficiency of the HV module is included in the measurement. Since the converter efficiency is not a constant over the full output range, variations must be accepted. Damage to the cable or the PMT can be detected by comparing the measured current to the predicted current caused by the base resistance. Deviations in the order of percent are not important here, but rather the possibility of detecting the extremes like a short circuit caused by e.g. water in the PMT base circuit or an interrupted cable. Due to the design of three independent channels per drawer, such failures can be isolated and do not impact operation of the other channels.

3.3 COMPARISON OF COMMERCIALLY AVAILABLE HV CONVERTERS

The HV generator is one of the core elements of a PhantomHV Pick-off channel. It transforms the DC 5 V to the required DC high voltage of up to 2 kV. There are different kind of HV generators available on the market.

Some of them have a load dependent output voltage without an integrated control circuit. For these kind of modules an external control loop and thus additional components on the PCB would be required. An additional feature of some HV generators is an integrated current measurement for the HV output current. When it comes to costs, the prices for different HV modules range from approx. 150 € to 300 €. In Table 2 available HV generator modules are shown.

Manufacturer	**ISEG**	**CAEN**	**HVM Tech.**	**HVM Tech.**	**EMCO/ XP-Power**
Model	BP020504p05	A7526P	UMHV0520	SMHV0520	A20P-5
Output voltage	2 kV	2.6 kV	2 kV	2 kV	2 kV
Output current	500 µA	500 µA	250 µA	500 µA	500 µA
Output ripple	<20 mVpp	<10 mVpp	<40 Vpp	<200 mVpp	<6 Vpp
Cost (@quantity)	88 € (>200)	140 € (>2000)	155 $ (>100)	208 $ (>100)	85 € (>50)
Regulated	Yes	Yes	No	Yes	No
Notes	Shielded U-Monitoring	Shielded U/I-Monitoring	Small housing No filtering incl.	Small housing U/I–Monitoring	Small housing No filtering incl.

Table 2 Overview of potential HV power supplies for the use on the PhantomHV Pick-off module (as of January 2020).

The products from ISEG and EMCO have been tested in practice during this work (see Figure 17). The main striking feature and the decisive disadvantage was the lack of regulation of the EMCO generator. Driven by the low output voltage ripple and the integrated control circuit the decision was made to use the HV generator module BPS from ISEG for the first prototype. The output voltage can be controlled from 500 V to 2 kV with an analog control voltage from 0 to 2.5 V. It is a shielded print module for PCB mounting with the dimensions 40 mm x 40 mm x 20 mm. For monitoring the actual output voltage, a separate pin with the monitoring voltage (0–2.5 V) is included. This signal is measured by the onboard microcontroller. There is no current measurement available in the mentioned HV module from ISEG. Another factor in the decision-making process of the HV module, is the positive experience with the manufacturer during past scientific projects.

3.4 SIGNAL SHAPER EVALUATION

Analog signal shaping is an important step in the signal chain. In case of PMT signals e.g. bandwidth and amplitude of a signal can be modified by a shaper and so matched to the readout and digitiser. To achive some degree of freedom and flexibility in the signal shaping, an active shaper is applied. An operational amplifier (opamp) enables first of all a gain greater than one. A fully-differential amplifier can be used to improve the noise immunity of the signal line to the ADC. Another reason for using an opamp is the concept of operating the opamp partly in saturation to extend the dynamic range of the system. Above a certain input amplitude at the opamp, the output amplitude will stop growing linearly, slowly saturate, and then reach the peak output voltage. The output signal will only grow in width from then on. Hence, in the saturated regime, the integral or width of the saturated output signal may be used to recover the original timing

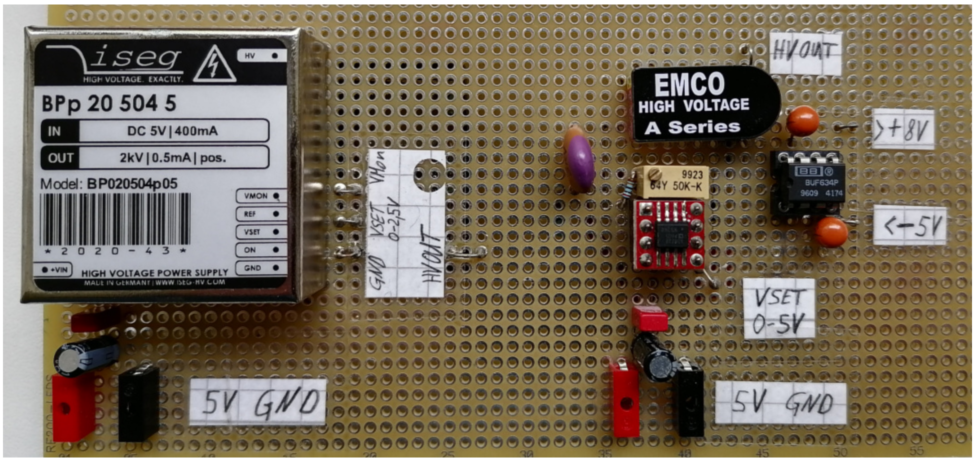

Figure 17 Test of HV generators from ISEG and EMCO. The EMCO generator does not have a control circuit which is why this was tried to be implemented in a simplified way. The control circuit for getting a load independent output voltage could not be solved with reasonable effort.

of the rising edge and the pulse charge based on the signal width using look-up tables from lab measurements. A balanced-Pi attenuator is used to match the saturated amplitude of the shaped differential signal to the ADC input range. Otherwise, the ADC input would eventually go into saturation before the shaper opamp would. However, this would miss the point of the concept of controlled saturation. Since saturation is not the intended operating region of an opamp, it is not specified in the datasheets. For this reason, the suitability of candidate parts for this concept had to be tested.

For the evaluation of candidate opamps a test board was designed (see Figure 18 and Appendix A). It includes three different opamp models with the same HV input circuit to ensure equal conditions. The two fully-differential opamps LTC6404-2 (Linear Technologies) and ADA4930-1 as well as the single-ended opamp AD8000 (both Analog Devices) are assembled on the test board. For the AD8000 only a pseudo-differential transmission of the output signal would be possible. Table 3 shows some of the main specifications of the different opamps under test.

Figure 18 *Left:* Assembled Opamp Test Board with three different opamps. *Right:* Front panel with SHV connectors for PMT and for HV supply. RJ45 socket for output of the shaped signals to the ADC. Banana sockets in red and black for connecting 24 V board operating voltage.

Component	Bandwidth	Slew Rate	Input Voltage Noise
LTC6404-2	600 MHz	700 V/μs	1.5 nV/$\sqrt{Hz}$
ADA4930-1	937 MHz	3400 V/μs	1.2 nV/$\sqrt{Hz}$
AD8000	477 MHz	2700 V/μs	1.6 nV/$\sqrt{Hz}$

Table 3 Listing of some main specifications of potential operational amplifiers for the use as signal shaper in the PhantomHV Pick-off module. All numbers are given for a 2 V output signal and a 5 V supply voltage [16][17][18].

The AD8000 is a single-ended opamp and therefore does not have a common-mode output voltage. Since the PMT output pulse is bipolar at the shaper input, the opamp input is biased with an offset voltage of around 2.5 V at 5 V supply voltage. This leads to a shaper output signal of half the operation voltage at rest without an input pulse. This matches the pseudo-differential signal to the digitisers input level. Measurements with this opamp showed an oscillation of the PMT pulse signal at the output. It may have been caused by the bias voltage applied to the input, which may not be sufficiently stabilised and has the voltage regulator as a limiting component. Therefore, the AD8000 will not be investigated further, and the focus will be on the favoured fully-differential candidate opamps. Figure 19 shows PMT pulse shapes for different light intensities for the two fully-differential opamps under test. The plots show pulses in the linear region and in saturation. The dark blue plotted pulses are deeply saturated ones, which show significant differences in their pulse shape for the two test devices. While the LTC6404-2 reaches its maximum amplitude and only gets wider from there, the ADA4930-1 has smaller bumps delayed depending on the height of the input pulse and the saturation. It reaches its maximum amplitude only gradually and not as clearly and abruptly as the LTC6404-2. Because of this well-behaved saturation, the LTC6404-2 is used as the candidate opamp for the PhantomHV Pick-off module. The schematic of the entire circuitry with shaper and signal pick-off can be found in Appendix B.

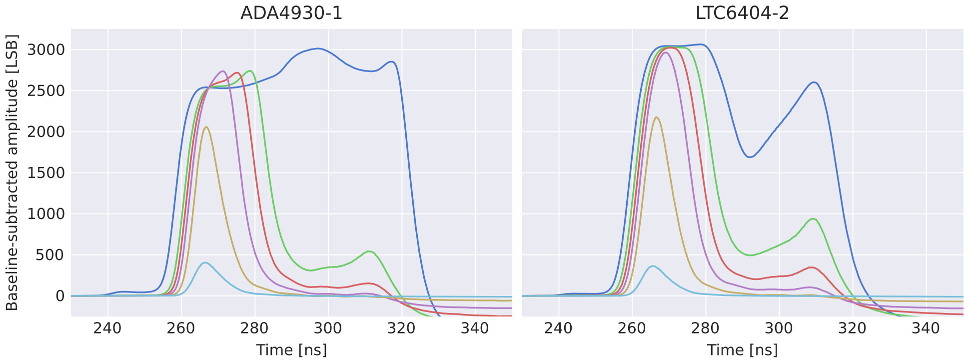

Figure 19 Pulse shapes for different light intensities reaching into saturation. *Left:* AD4930-1 *Right:* LTC6404-2

The recorded pulse shapes in Figure 19 could be plotted just for a single pulse, but this would not be representative on the fast edges and the general shape due to the 250 MS s^{-1} ADC system. For this reason, an algorithm developed for the FlashCam system is applied to reach a subsampling resolution like in the plotted pulse shapes in Figure 19. This enables more detailed information, especially at the fast edges, like it would have been digitised at a higher sampling rate. The principle behind that is based on a free-running ADC and laser trigger and the fact that the FlashCam ADC clocks are synchronised to better than 30 ps. A detailed description of this approach can be found in Appendix C.

3.5 RELIABILITY TESTS

The PhantomHV system is tested in a climate chamber to verify its functionality within reasonable climate conditions. Even though the system is intended to be operated in an environmentally-controlled cabinet, during the test it is exposed to a wider climate range. For the test a 19-inch crate equipped with a PhantomHV Master and two PhantomHV Pick-off modules (6 channels) are placed in a climate chamber (see Figure 20).

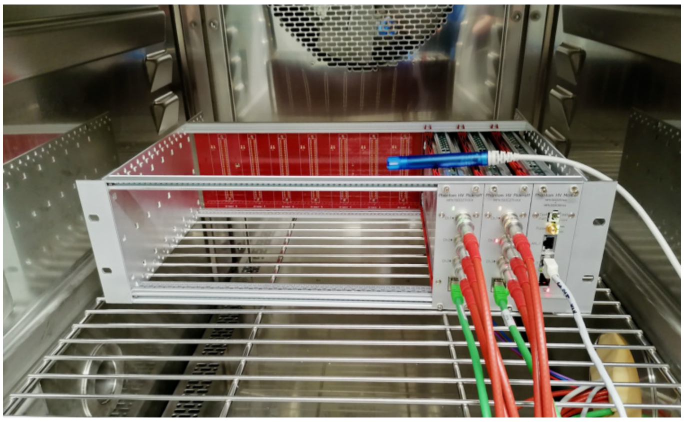

Figure 20 Climate chamber tests of a six-channel PhantomHV system loaded with 10 Mohms per channel.

The temperature and relative humidity is measured by an external reference sensor. The actual high voltage and current for each of the channels is measured by the PhantomHV itself. Every channel is loaded with 10 Mohms, which leads to the expected maximum current at a set voltage of 2 kV. Additionally, the output signal of every channel is connected to an ADC (FlashCam) outside the climate chamber to detect possible transients caused by high voltage arcs. The climate chamber is cycling the relative humidity within one day from 0 % r.H. to 100 % r.H and back. At the same time the temperature is cycled five times from -10 °C to 50 °C. The programmed cycle generated many combinations of temperature and rel. humidity during the approx. 2 weeks measurement period. The recorded phase space is shown in Figure 21 (left). The whole PhantomHV system is periodically turned off and on to test the starting procedure with booting and ramping up HV. Figure 21 on the right shows the HV monitoring with a long and short power-off period per cycle. The long power-off period should simulate a cold start scenario by giving all components time to adapt to the applied environmental conditions.

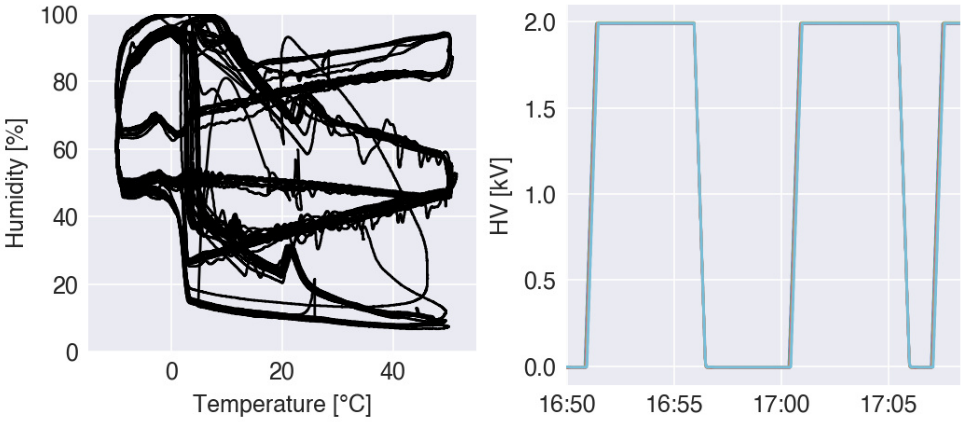

Figure 21 *Left:* The covered phase space of the programmed cycle (the climate chamber is not capable of producing a dry environment at sub-zero temperatures). *Right:* The HV measurements during a sample cycle showing one long and one short power-off period per cycle.

While no failures were observed, these tests revealed a too small clearance that despite conformal coating resulted in high-voltage arcs at the maximum operational voltage (2 kV) and extreme humidity (above 90 % r.H). Figure 22 shows that the pad of the PCB was unnecessarily large and in addition the housing of the HV module is too close to the output pin. This causes HV arcs against ground potential of the housing. The manufacturer of the DC/DC converters has revised the packaging already and offers the new version with an increased clearance. In another project, it turned out that the conformal coating used here (Plastik 70 from Kontakt Chemie) might not meet the requirements. Therefore, a different product is being tested (ELPEGUARD SL 1307). Furthermore, a PCB revision is being planned to reduce the pad size, and include a humidity sensor as an additional safeguard which limits the operational range of the HV module. The existing 18 channels are currently being modified to improve their humidity tolerance and tested in a climate chamber before being redeployed in the corresponding lab setups or field tests.

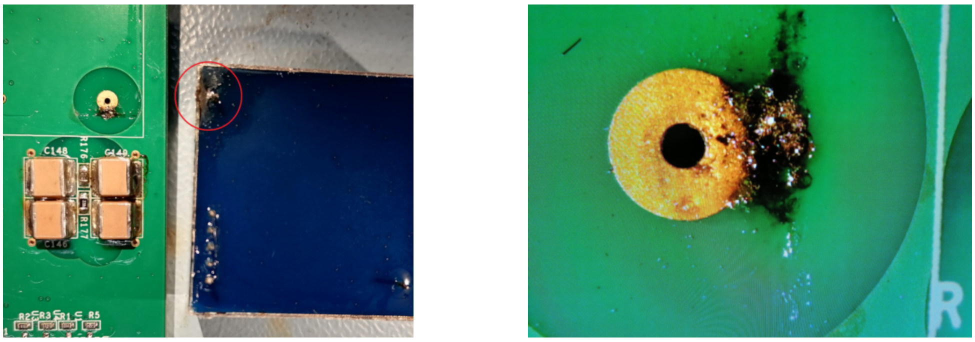

Figure 22 *Left:* Too small clearance of the highlighted HV output pin and the housing of the HV module. *Right:* Burnt spot at the pad of the HV output due to HV arcs.

A different test is still required to ensure functionality at high altitudes. At the proposed project sites at altitudes above 4000 m asl the air pressure will be around half the atmosheric pressure compared to sea level. This leads to a reduction of cooling by convection due to the lower air density. An even more important aspect is the reduction of the minimum possible gap between HV components without generating HV arcs. This relation is described by Paschen's law (see Figure 23). It describes the breakdown voltage between two electrodes in a gas as a function of distance and pressure [19]. For air with a pressure of 0.5 atm (at ~5000 m asl) and a voltage of 2000 V the minimum air gap is around 1.5 mm. Comparing this to the minimum gap at sea level for the same voltage of around 0.3 mm shows the large effect of air pressure on this. This was taken into account in the design of the PCB of the PhantomHV Pick-off module. Nevertheless, the functionality is planned to be confirmed experimentally in a low-pressure test chamber.

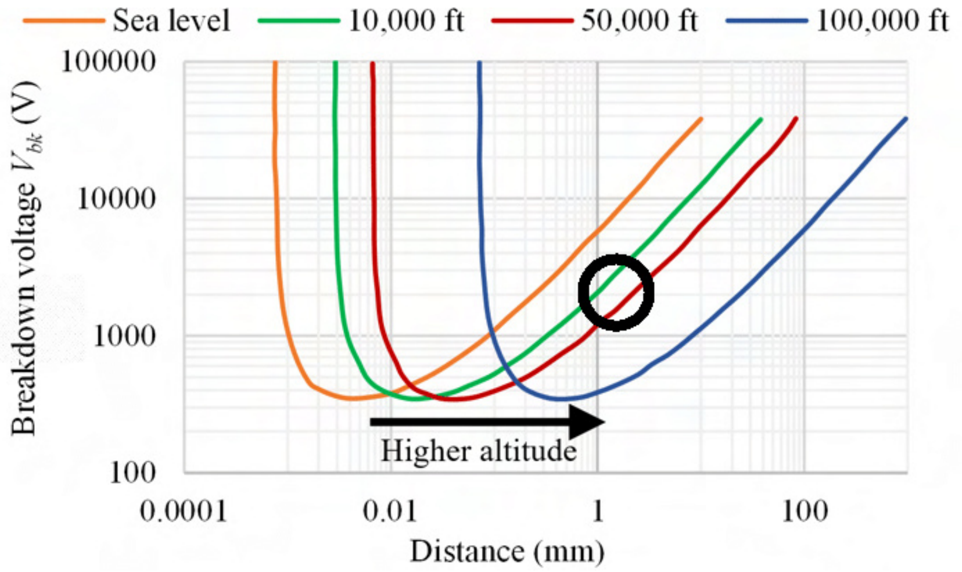

Figure 23 Paschen's law for different altitudes and the resulting minimum distance. For 2000 V and a altitude of ~5000 m (~16400 ft) the minimum distance without HV arcs lies in the marked region between the green and red curve with 1–2 mm. The figure is taken from [20].

4

PHANTOMHV PERFORMANCE AND OPTIMISATION

This chapter describes the characterisation of the measurement chain which is based on the PhantomHV system in combination with the FlashCam ADC. Since there are several parameters to vary, there are numerous combinations to test. This includes the capacitance of the pick-off circuit to separate the PMT signal from the HV, the input filter of the opamp, and the HV applied to the PMT. Which combination works well, or which performance can be achieved at all with the proposed system, is determined on the basis of the calculated charge and time resolution. In addition, the behaviour of the shaper opamp in saturation and the resulting charge recovery for extending the dynamic range is tested. The PMTs are illuminated by sub-nanosecond laser pulses injecting between 0.2 and 100,000 photoelectrons (p.e.) per pulse. Figure 24 shows the schematic of the PhantomHV front-end circuit with pick-off and high voltage feed-in. The schematic of the whole circuit diagram with signal shaper can be found in Appendix B

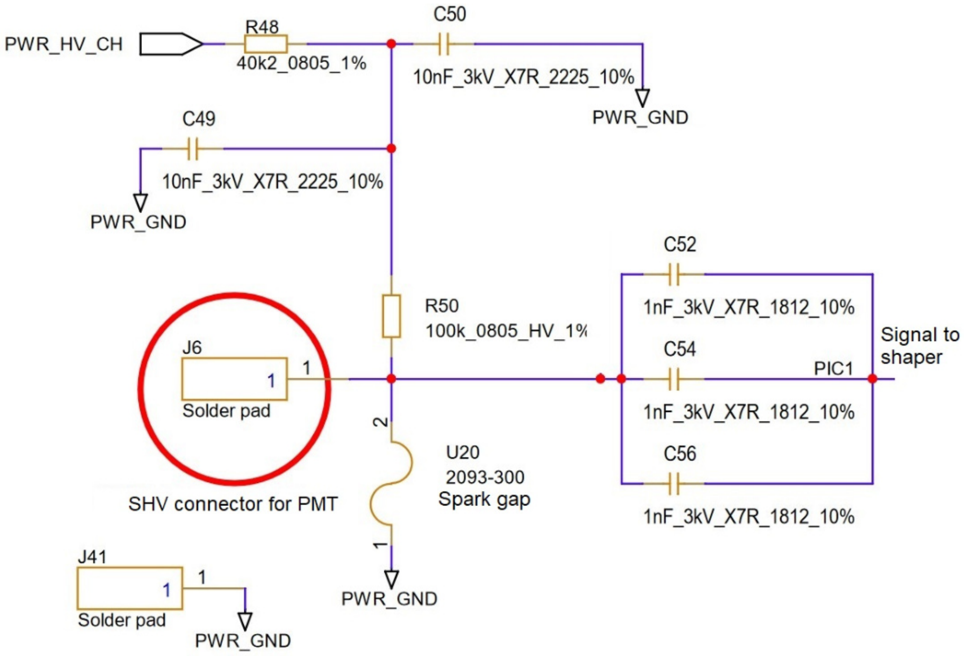

Figure 24 Schematic of the Pick-off circuit to separate HV and PMT signal

4.1 MEASUREMENT SETUP

The measurement setup consists of a PicoQuant PDL 800-D 398 nm diode laser which is triggered by a Siglent SDG6022X pulse generator. Its output light signal is a sub-nanosecond pulse which is much narrower than the typical transit time spread of the operated PMTs of about 3 ns. Consequently, the time profile is dominated by the PMTs. The laser head and two 8-inch PMTs from Hamamatsu Photonics are mounted in a dark container. The two PMTs are a $\sim$25-year old R5912 with custom base and a $\sim$5-year old R5912-100 in waterproof housing, both with passive bases. The distance between laser and PMTs is approx. 4 m. The laser output is attenuated by a remote-controlled OD4 filter wheel. A beam splitter behind the filter wheel diverts 50 % of the attenuated beam to a NIST-calibrated monitoring photodiode with network readout. The other half hits a holographic diffuser to evenly distribute the light onto the PMTs under test. The PMTs are connected via $\sim$30 m RG-58 coaxial cables to a PhantomHV system outside the container. As an initial setting the separation of the PMT signal pulses from the high voltage is done with a 3 nF HV capacitor while the operational amplifier for shaping the signal has a voltage gain of 2. The signal is transmitted differentially to a FlashCam 24-channel $250\,\mathrm{MS\,s^{-1}}$ 12-bit ADC via standard Cat. 6a cable. For matching the saturated amplitude of the shaped differential signal to the ADC input range a balanced-Pi attenuator with 10 dB is used. A schematic of the measurement setup and photos from the inside of the darkbox container are shown in Figure 25. The third PMT in this photo is not part of the tests.

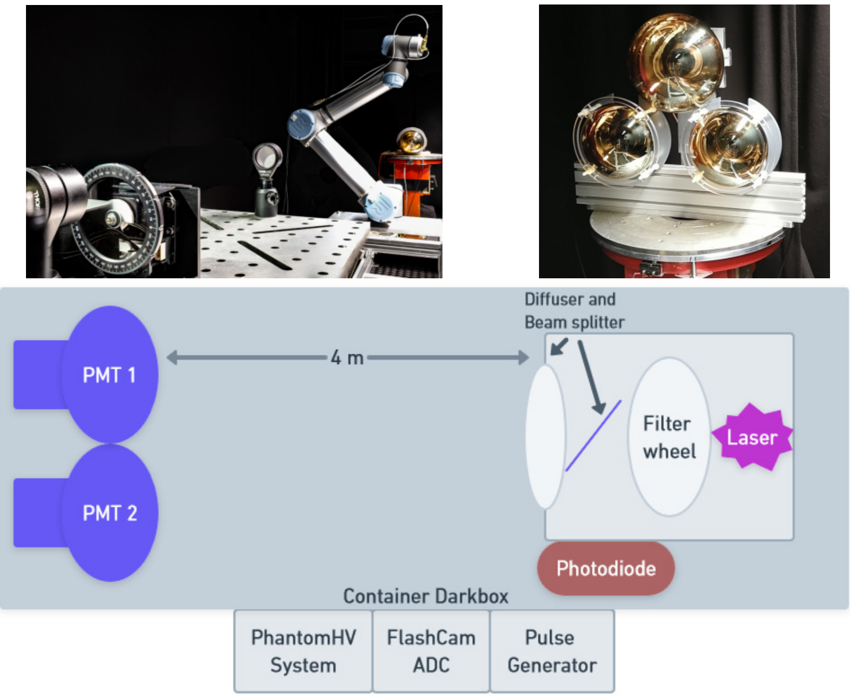

Figure 25 Photos and a sketch of the measurement setup inside and outside the darkbox container.

4.2 PULSE RECONSTRUCTION

4.2.1 *Gain Calibration Method*

For the characterisation of the single photoelectron (SPE) response, first a low-illumination amplitude spectrum at the maximum chosen HV of 1700 V is obtained and a multi-photoelectron spectrum as shown in Figure 26 is fitted to it. The existing fit consists of a convolution of Gaussian electronics noise distribution with two truncated normal distributions[1] that model the weakly and normally amplified photoelectron signal distributions. The individual charge contributions are weighted by the respective Poisson mass function.[2] This results in a narrow noise peak called pedestal and a well-recognisable SPE peak next to it. As the gray fitted 1 p.e. line indicates, the pulse height distribution is not symmetrical to the mode of the 1 p.e. hump. It has a part which streches into the pedestal.

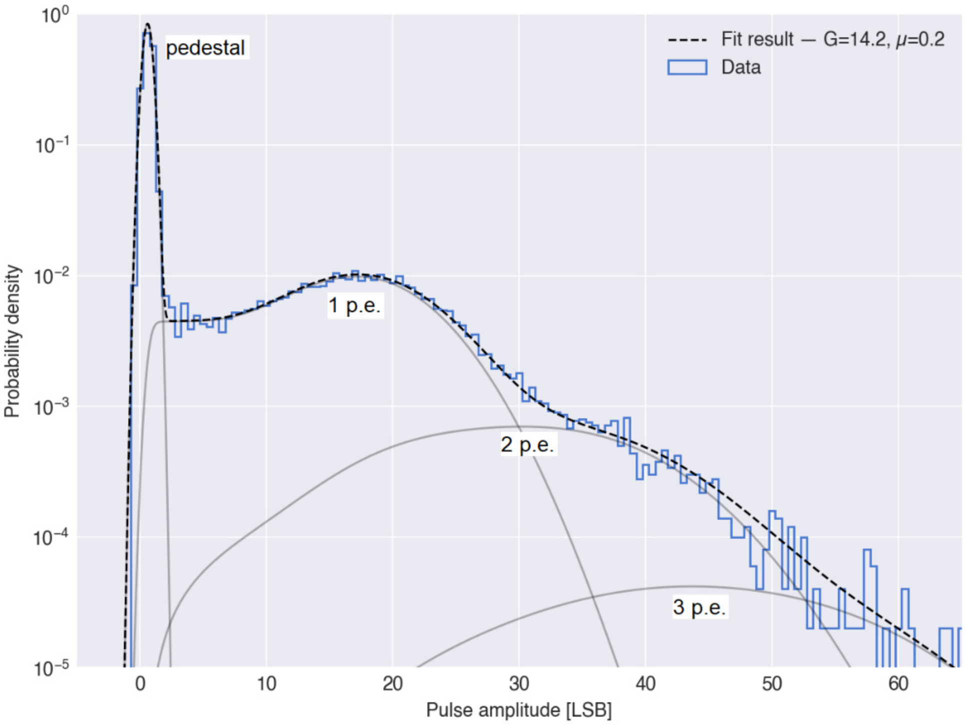

Figure 26 Measured low-illumination amplitude spectrum at 1.7 kV (blue histogram) and multi-photoelectron fit (black-dashed line) with average single p.e. amplitude $G = 14.2$ LSB/p.e. and average illumination level $\mu = 0.2$ p.e. The contributions of individual photoelectrons are shown as solid grey lines.

Different mechanisms like pre and late pulses (see Section 1.5.3) contribute to this. This particular applied fit also models the weakly amplified photoelectrons and thus works best for large gains.

The properties of the single p.e. model are then used as an input to cross-check another method to obtain the gain at lower HVs. There the mode

---

[1] `https://en.wikipedia.org/wiki/Truncated_normal_distribution`

[2] `https://en.wikipedia.org/wiki/Poisson_distribution`

of the dark amplitude spectra is estimated and rescaled based on the ratio between mode and mean of the 1700 V SPE model. While mode is the most frequent value in a set of data values, e.g. in a histogram the hump, the mean is the average of the measured amplitudes or specifically here the pulse charges. Figure 27 shows dark count spectra for different HVs with marked modes. Rescaling them leads to reasonable matching of the dark count charge distributions independent of the HV. The great advantage of the dark count spectra method is that no additional light source is required for collecting pulses and generating the spectrum. Once the SPE spectrum is characterised in the lab or with a flasher in a detector, the mode to mean ratio is known for further calculations. There are also other calibration methods such as the Zero-Poissonian method or using photon statistics which are not discussed here.

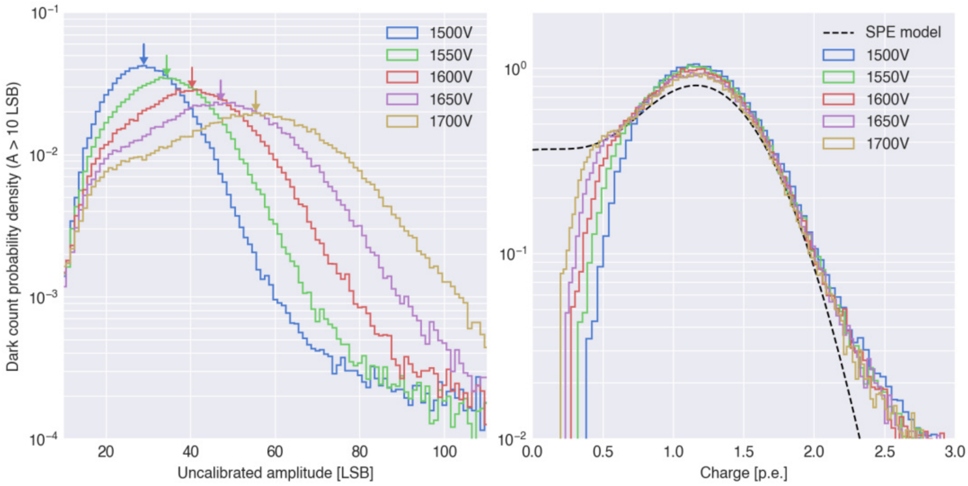

Figure 27 *Left:* Pulse height distributions from dark counts measured with a trigger threshold of 5 LSB and effective analysis threshold of ∼10–15 LSB. The modes found by Gaussian Kernel Density Estimation are marked with arrows. *Right:* Rescaling the histograms on the left by their mode/1.16 (to account for the shift between mode and mean) shows reasonably matching dark count charge distributions. The 1700 V SPE model is shown as black dashed line for comparison.

4.2.2 *Saturation Recovery Using Inverse Electronics Function*

Depending on PMT gain, charge pulses beyond ∼250 p.e. (at 1700 V) or ∼500 p.e. (at 1500 V) would be clipped by the ADC's dynamic range of 12-bits, impacting the charge and leading-edge timing reconstruction. Therefore, an operational amplifier in the PhantomHV Pick-off module produces a well-defined saturation curve. The evolution of the pulse shapes towards saturation for different injected charges is shown in Figure 28.

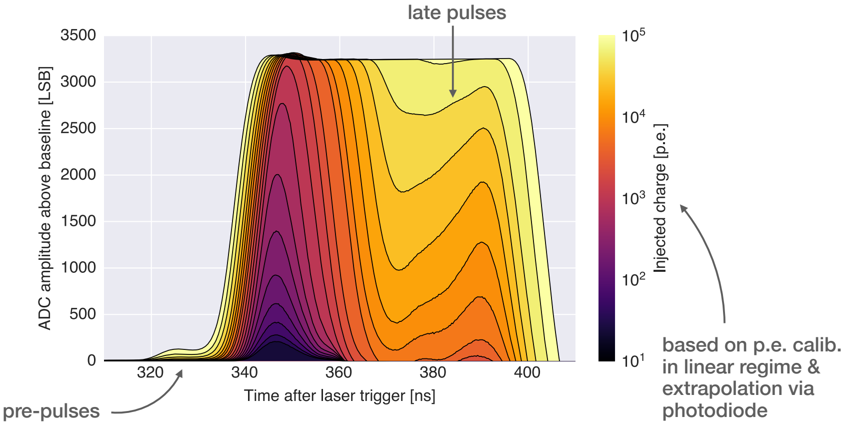

based on p.e. calib. in linear regime & extrapolation via photodiode

Figure 28 PMT pulse shape for injected charge over 5 orders of magnitude. Saturation occurs from a pulse height of about 3300 LSB. Pre and late pulses are indicated.

To recover the charge and timing information in the saturated regime, the end-to-end transfer function of the electronics chain is characterised and inverted using the following method:

- in the linear regime, the photodiode power is related to the average measured pulse amplitude (pulse integral incl. main and late pulses) using a linear fit. This is used to predict the average pulse amplitude in the saturation regime by using the photodiode readings.
- to allow recovery of the pulse amplitude (integral) in the saturation regime the inverse transfer function of measured pulse amplitude vs. predicted pulse amplitude is modelled by using a quadratic spline, see Figure 29 (right panel)
- to allow correction of the nanosecond-scale time slewing observed in the transition to saturation, the measured slewing curve as a function of recovered pulse height is modelled by using a quadratic spline, see Figure 29 (left panel)

By calculating the two recovery splines as a function of pulse height (in LSB) they are independent of the PMT gain at first order. Second-order effects such as changes in the single p.e. pulse shape with HV are visible mostly near the transition into saturation, e.g. at the peak of the time correction. Further second-order effects such as dependencies on the light time profile are to be studied in dedicated measurements.

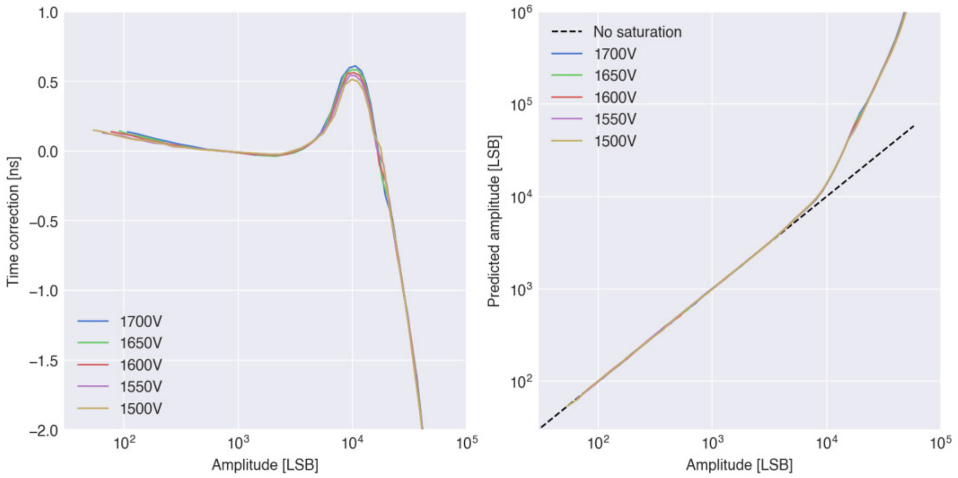

Figure 29 *Left:* Measured time offset vs. pulse amplitude and interpolation model. *Right:* Predicted pulse amplitude vs. measured pulse amplitude and interpolation model.

4.2.3 *Time and Charge Resolution*

Based on the previous calculations the time and charge resolutions are determined from the saturation recovered pulses. The resolutions serve as comparison parameters for different setups, PMTs, and signal processing chains. Figure 30 shows the time and charge resolutions given as the RMS value, and as the optimum the unavoidable Poisson fluctuations of $\sqrt{Q}$. Both time and charge resolution are dominated by the properties of the PMT up to a few hundred p.e.. Beyond that, in the deeply saturated regime, time resolution better than 100 ps and charge resolution better than 10 % are maintained up to ∼100,000 p.e. injected charge, which likely exceeds the dynamic range required for SWGO.

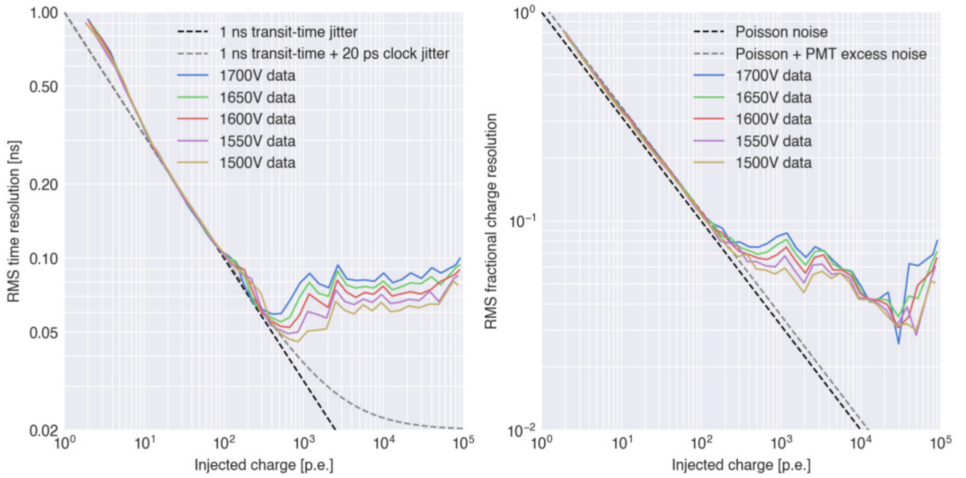

Figure 30 RMS time resolution (left) and charge resolution (right) up to ∼100,000 p.e. after saturation recovery.

4.3 OPTIMISATION OF THE ANALOG SIGNAL CHAIN

4.3.1 *Input Circuit Configurations*

The analog signal chain of the PhantomHV Pick-off module features several adjustment options to modify the pulse shape. The way to find the optimal configuration for a given measuement chain depends somewhat on detector properties like e.g. the detector dimensions and thus the light time profile at the PMT. Since these decisions are not made yet by the SWGO collaboration, no final optimisation of the electronics can be done. Instead, a parameter space of potential configurations is demonstrated.

Figure 31 shows pulse shapes for different configurations of the input circuit. The decoupling capacitor is varied between 3 nF and 12 nF. In addition, there are configurations containing an RC low-pass filter applied between the decoupling capacitor and the shaper opamp. The cut-off frequencies under test are 10 MHz and 20 MHz. In the left plot of Figure 31 the main difference in the pulse shape for the linear regime (non-saturated opamp) can be seen between the configurations with and without an applied low-pass filter. With a lower cut-off frequency the PMT pulse gets broader and lower in amplitude as well as the pulse rise time gets less steep. The decoupling capacitance turned out not to play a major role except that a higher capacitance reduces the undershoot. In the right part of the plot saturated pulses are shown. There the impact of the low-pass filter is visible as the smearing and merging of the prompt and late pulses.

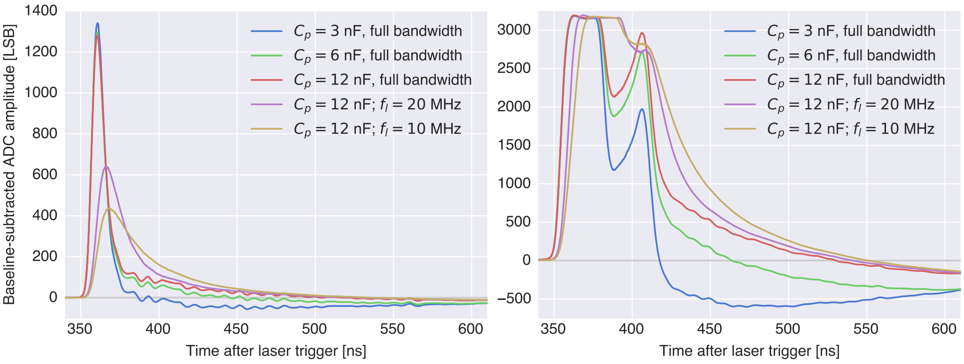

Figure 31 Pulse shapes for different configurations of the input circuit. The pulse integral of the illuminated PMT R5912 is the same for all curves per plot. The pulse shape of configurations with a low-pass filter show a smaller amplitude and a broader pulse compared to them without. This effect is more pronounced the lower the cut-off frequency of the filter. Increasing the decoupling capacitance leads to a reduction of the undershoot.

Figure 32 shows the resulting time and charge resolution for the described configurations under test. For the charge resolution no significant difference can be observed between the different configurations. The situation is different for the time resolution, because there the operation without a low-pass filter has advantages below ∼1000 p.e.. Depending on the required dynamic range and the expected pulse frequency of the final water Cherenkov detector design the optimal configuration can be selected.

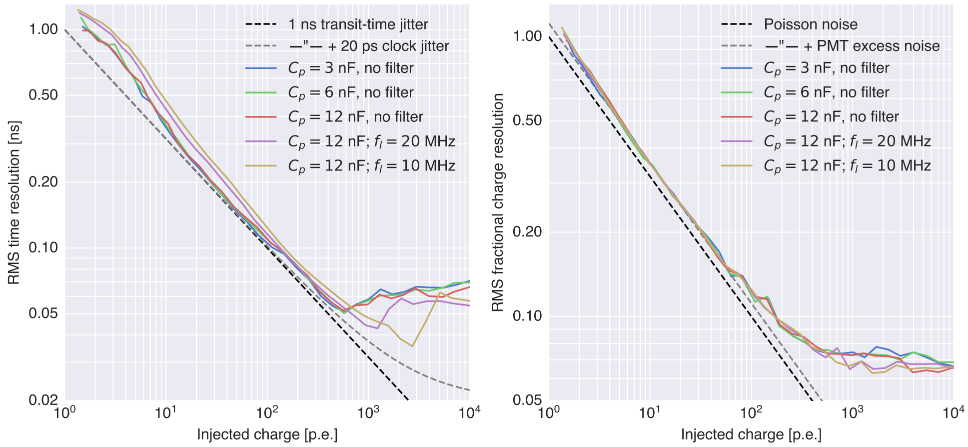

Figure 32 Time and charge resolution for different input circuit configurations. Below ∼1000 p.e. the time resolution is worse for the filtered inputs compared to the non-filtered ones. Beyond 1000 p.e. the filtered inputs are doing better which is caused by the lower amplitude of the pulses and their later saturation point. For the charge resolution negligible improvement in saturation recovery as well can be observed.

In case of a high repetition rate it may be benificial to select a high decoupling capacitance in combination with the full bandwidth to get a narrow signal pulse with a small undershoot to minimise the overlap of consecutive pulses. The measurement described here gives an overview of how the different parameters influence the final resolution results. Summarising, one can say that the results for the different configurations are only very small. The hardware configurations as well as the signal reconstruction can still be optimised based on the final needs. Therefore the results shown provide a starting point for further optimisation steps.

4.3.2 *Crosstalk*

Crosstalk describes the interference between different cables, wire pairs or circuits due to unintended coupling. These unintentionally induced signals cause errors in data transmission or, like in this specific case, lead to wrong trigger signals. In the signal analysis problems could occur caused by faulty event trigger signals. For this reason, this particular case is investigated for the proposed measurement setup. The crosstalk between the different channels of the PhantomHV Pick-off module is tested by inserting a large PMT signal one after the other into each channel. The laser rate is set to 10 kHz at an intensity of around 230 p.e., which covers almost the whole linear region of the shaper without saturation. This maximises the cross-talk into the trigger signal (which, due to its differential DSP filter is sensitive to high-frequency components). Triggering is done on the respective other channels to detect potential crosstalk signals. The trigger level therefore is set to 4 LSB, which is slightly above the noise level of the ADC. Table 4 shows the trigger rates for each channel. Channel 0 seems to be without any interaction with the other channels while channel 2 and 3 have a slight coupling to each other. The crosstalk trigger rate there is less than 4 % and thus within an acceptable level considering the high intensity of the inserted pulse and therefore low rate of occurrence in the detector.

Trigger rate	**Insert Channel 0**	**Insert Channel 2**	**Insert Channel 3**
Channel 0	–	0 Hz	0 Hz
Channel 1 (open pin pair RJ45)	9,5 kHz	10 kHz	10 kHz
Channel 2	5 Hz	–	228 Hz
Channel 3	0 Hz	390 Hz	–

Table 4 Trigger rates of crosstalk between the PhantomHV channels.

A further and almost more important aspect about this study is the amplitude of the crosstalk. Since any kind of unintentional pulse-like signal would be negative for the measurement, this has to be prevented or kept at a minimum. Therefore, the signal amplitude induced from another channel is also analysed similar to the trigger signals.

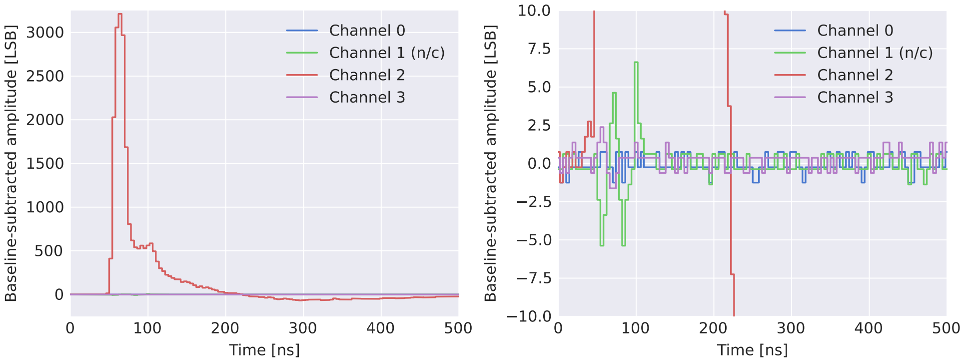

Figure 33 Crosstalk measurement of the PhantomHV Pick-off module. *Left:* Large ∼3000 LSB PMT pulse on channel 2. *Right:* Crosstalk measured on the other channels is less than 1 ‰. Channel 1 is the pin pair of the RJ45 connector which is not connected

Figure 33 shows a large ∼3000 LSB PMT pulse as input for the middle channel (Channel 2) of the PhantomHV Pick-off module. A closer look at the amplitudes of the other three channels shows small pulses as crosstalk caused by channel 2. The ratio of the maximum amplitude of channel 3 compared to input pulse is around 0, 8 ‰. The green signal curve of channel 1 shows the unconnected pin pair of the RJ45 connector. Its crosstalk is significantly larger, which confirms the decision not to use this pin pair.

4.4 HF OPTIMISATION OF THE INPUT CIRCUIT

The initial and also current input circuit of the Pick-off module includes besides the coupling capacitor also a transformer with the ratio 1:1.33 (TRS1.33-1T-75+ from Mini-Circuits). This is a remnant of the HAWC circuit which was used to match the impedance from 75 ohms of the cable to 100 ohms of the readout system. This transformer acts as a balun and has the advantage of providing out of the unbalanced PMT signal a balanced output towards the readout respectively the shaper. The disadvantages of this component, however, are the influence on the frequency response and the dependence and poor availability on a single part. The range of adjustment possibilities without this component would be significantly expanded and modifications of the frequency response could be implemented mainly with resistors and capacitors. It is therefore advisable to remove this component without any losses in terms of signal quality and termination. A possibility could be to operate the shaper opamp with a single-ended input circuit. However, this must also include an adjustable termination for at least 50 and 75 ohms impedance. The resulting circuits shown in Figure 34 are both based on the opamp LTC6404-2 and are terminated to 50 ohms.

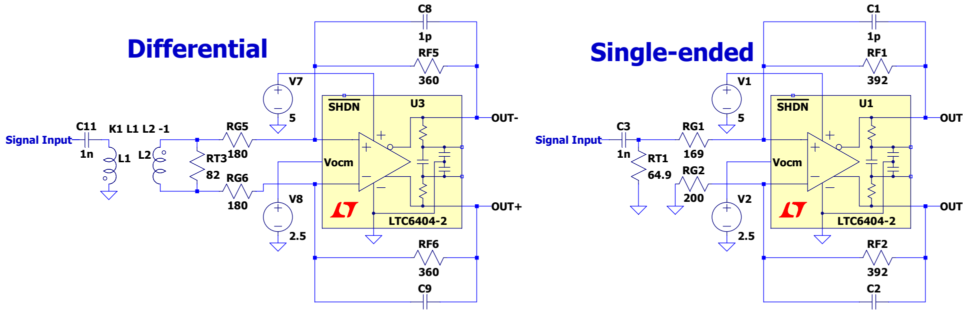

Figure 34 Schematic of the differential (with transformer) and single-ended input circuit (without transformer) under test with the opamp LTC6404-2

Test measurements with the two different input circuits and a PMT R5912 connected to it showed an almost identical pulse shape for both of them (see Figure 35). At the same pulse height, the undershoot of the differential variant is slightly larger than that of the single-ended one. To compensate a small difference in the amplification of the two channels under test, the data of the single-ended circuit is divided by a factor of 1.2 for matching the histograms and thus the pulse heights. The deviation in gain is not crucial and can be calibrated out or certainly be fine-tuned. Another feature which applies to both, is a quite small reflection ∼250 ns after the PMT pulse. This matches the expected roundtrip pulse transit time of the 25 m coaxial cable attached to the PMT. Since the termination of both circuits is done with resistors, of which the values show tolerances and deviations from calculations due to availability by nominal values, missmatches can occur. This requires some effort to find a suitable configuration of resistors to eliminate or minimise the signal reflections even further.

For a more detailed understanding of the high-frequency (HF) characteristics of the input circuits a network analysis is performed. For this purpose, the network analyser ZVL from Rohde & Schwarz is used to measure the reflection coefficient (S11 in terms of S-parameters) of the different input circuit configurations under test. This shows how well the system is terminated over the tested frequency range or in other words how much of the input signal is reflected. Figure 36 shows the measured S11 parameters for the differential (blue) and the single-ended (green) input circuit over a wide

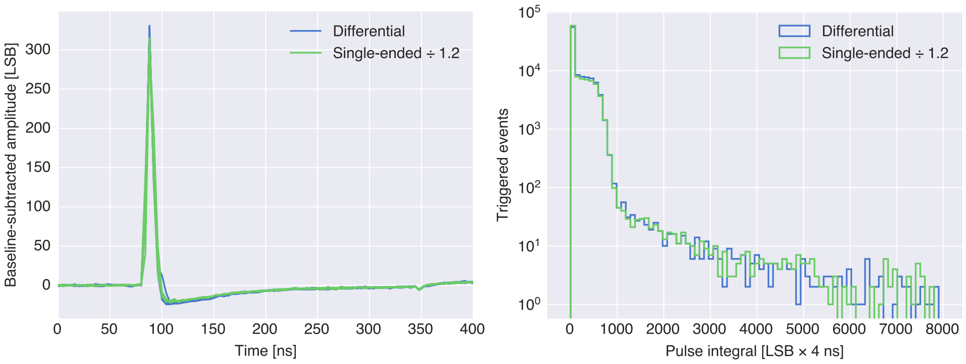

Figure 35 Comparison of the PhantomHV Pick-off with differential and single-ended opamp circuit. The single-ended circuit comes without transformer. Measured are dark counts of a PMT R5912 at 2 kV in a closed cardboard. *Left:* Pulse shape with a matched amplitude of around 300 LSB. *Right:* Histogram of pulse integrals

frequency range. The measured range is selected based on the intended measurement chain with the 250 MS s^{-1} FlashCam ADC and its built-in anti-aliasing filter. The bumps at around 150 MHz in Figure 36 (right) turned out to be caused by the piece of cable which connects the SHV socket in the front panel of the drawer and the PCB. By touching this cable while measuring, significant changes in the frequency response can be observed. This needs to be changed to a more stabilised connection, which could be solved by using a small upright PCB as connection between socket and main PCB. The lowest reflections are measured at 40 MHz where both circuits have their minimum in return loss and thus the best impedance matching. While the differential circuit has a reflection at this frequency of -40 dB, the single-ended circuit has around -25 dB. Expected is a lower reflection for the single-ended circuit compared to the differential one because of the missing transformer. Since it is measured different, it seems a missmatch of the single-ended version causes a higher level of reflection. The 3 resistors which are involved in the termination are more prone to deviations, and so a missmatch, than the one termination resistor in the differential circuit. The resistor values need to be adjusted experimentally to achieve the best possible impedance matching. Additionally, there are still the parasitic capacitances and inductances in the signal path, which can hardly be avoided. These parasitic elements will be the dominant effects in the end.

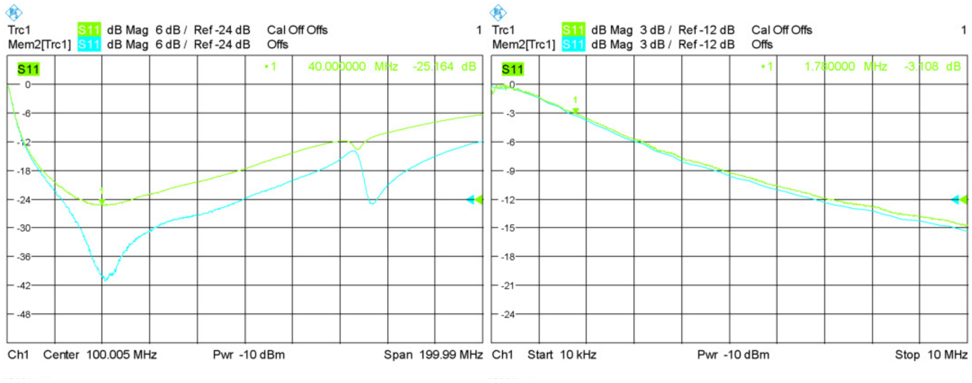

Figure 36 Frequency analysis of the reflection (S11 parameter) at the Pick-off circuit for the differential (blue) and the single-ended (green) variant. *Left:* For the differential circuit with transformer the frequency response (1 MHz – 200 MHz) shows dips in the return loss. *Right:* The frequency response in the lower region (10 kHz – 10 MHz) shows the expected high-pass filter characteristic of the decoupling capacitor (1 nF at 50 ohms) for both circuits equally.

5

PMT IMPLEMENTATION

For the measurement of Cherenkov light and as a main component in a WCD highly sensitive (single)photon detectors such as silicon photomultipliers (SiPMs) or photomultiplier tubes (PMT) are required. The SWGO reference design contains a submerged PMT facing a light tight water volume to detect generated photons. For this reason PMT and cabling need to be entirely waterproof. For the mass procurement it may be convenient to buy fully potted PMTs from industry to avoid engineering and evaluation of materials. However, the development described in the following is mainly driven by the fact that around 100 recovered 8-inch PMTs (Hamamatsu R5912) are locally available from a planned project from the late 1990's which was not realised. These could be used for SWGO and would especially help to build prototypes without long delivery time for purchased PMTs. These recovered PMTs come as a bare glass tube with thin electrical leads. Besides developing the encapsulation scheme and the voltage divider base, testing the functionality and performance of these 20 year old PMTs is essential. A second source of recovered PMTs is from the former neutrino experiment Double-Chooz, from which 250–400 pieces of the 10-inch PMTs (Hamamatsu R7081) are available. They have been operated in scintillator oil which is why they have a potted base and enclosure with a cable attached to it. Here the focus lies on testing water compatibility of the potting and selected materials.

5.1 BASE DESIGN

A PMT needs a specific voltage taper along its dynodes to accelerate and multiply the generated photoelectrons. In the case here, the photo cathode is connected to ground while the anode is connected to a positive high voltage of up to 2000 V (see Section 1.5.2). The dynodes in between those two need a specific voltage taper to achieve e.g. a given timing characteristic, amplification and noise figure. These parameters depend on the internal geometry of the dynodes and field-forming structures. For the base design the recommendations of the manufacturer are followed and relied solely on SMD components. This has the advantage that SMD components can be assembled by machine and also have a smaller footprint. The assembled bases are soldered to the electrical leads of the PMT.

The voltage divider circuit is derived from recommendations of the current model of the Hamamatsu R5912-100. Datasheets back from the 1990's vary slightly from the current version (see Table 5). The differences in the taper are at the first and the last six dynodes. Whether there were modifications of the internal PMT geometry which would lead to different properties is uncertain. The schematic of the designed PMT base is shown in Figure 37. A proper functionality of the combination of the old PMT version and the current base circuit is confirmed by test measurements (see section. 5.2).

Electrode	C	DY1	F2	F1	F3	Dy2	Dy3	Dy4	Dy5	Dy6	Dy7	Dy8	Dy9	Dy10	P
Ratio New	16.8	0	0.6	0	3.4	5	3.33	1.67	1	1.2	1.5	2.2	3	2.4	
Ratio Old	11.3	0	0.6	0	3.4	5	3.33	1.67	1	1	1	1	1	1	

Table 5 Comparison of the recommended voltage taper for the old and the new Hamamatsu R5912 8"PMT

The highest voltage of the taper is applied between the photocathode and the first dynode. The used SMD resistors have the package size 1206 and thus a maximum operating voltage of typically 150–200 V. The resistor connected between ground and the first dynode at which the highest voltage in the divider of around 800 V is applied, is replaced by four resistors in series (R1–R4). For the capacitors C5 and C6 which are placed between ground and maximum high voltage, SMD ceramic capacitors with a maximum operating voltage of 3 kV were chosen. These capacitors stabilise the operational voltage of the PMT. The capacitors C1–C4 and C7 are placed at the last dynodes to stabilise the voltage at the most stressed dynodes and provide charge for forming of especially large signal pulses. The components C6 and R20 are forming the termination of the system by means of a high-pass filter for blocking DC voltage. Depending on the connected coaxial cable and readout system either 50 ohms or 75 ohms are assembled. A proper impedance matching on PMT and readout side will improve signal quality by reducing ringing of reflected signal pulses. The 100 ohms resistors at the last dynodes act as damping resistors to also reduce ringing of fast output pulses with rise times less than 10 ns. Additionally, the lowpass of R19 and C5 will reduce potential noise from the high voltage supply [13]. Since there are many different potentials in the layout of this PCB, fulfilling the clearances is crucial. For this purpose, a matrix of mutual clearance constraints for different parts with different potentials has been applied. The result can be seen in the layout of the PMT base design in Figure 38.

Additionally, all components on the PCB are coated with conformal coating to reduce the influence of dust and moisture. The two holes in the middle of the PCB serve as strain relief to fix the coaxial cable to the PCB.

Since the schematic of the base circuit is quite simple and the number of components is relatively low its reliability is expected to be high. This is confirmed by a reliability analysis using the standard Siemens SN 29500 in a dedicated calculation tool (ReliaSoft). As input for this calculation the type of component, the power dissipation, operation and rated voltage as well as the temperature of every component are applied. The component temperature is a very important factor for the reliability analysis of components or a system.

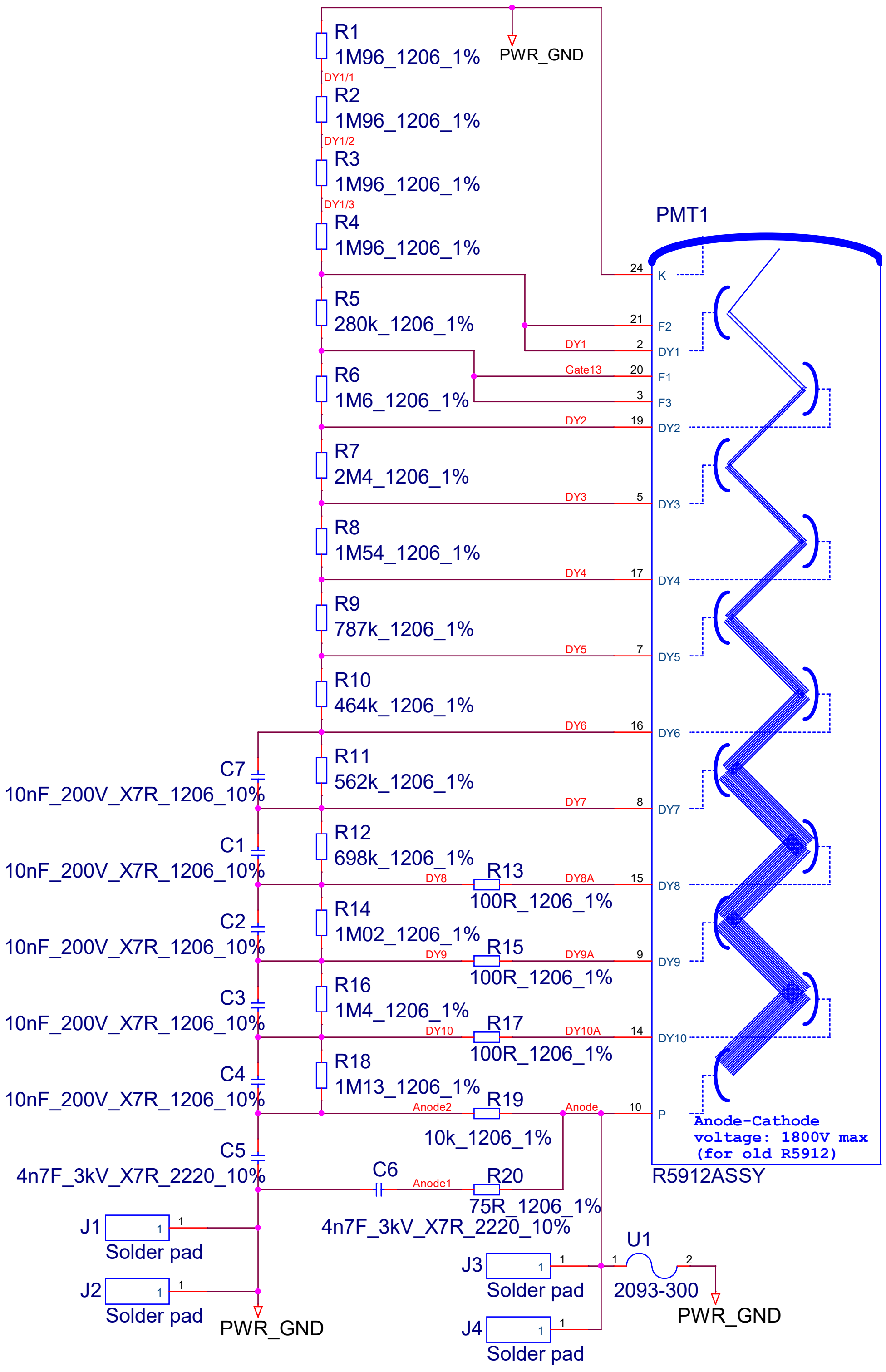

Figure 37 Schematic of the new designed PMT base with SMD components. The photocathode is connected to ground while the positive high voltage is connected to the anode.

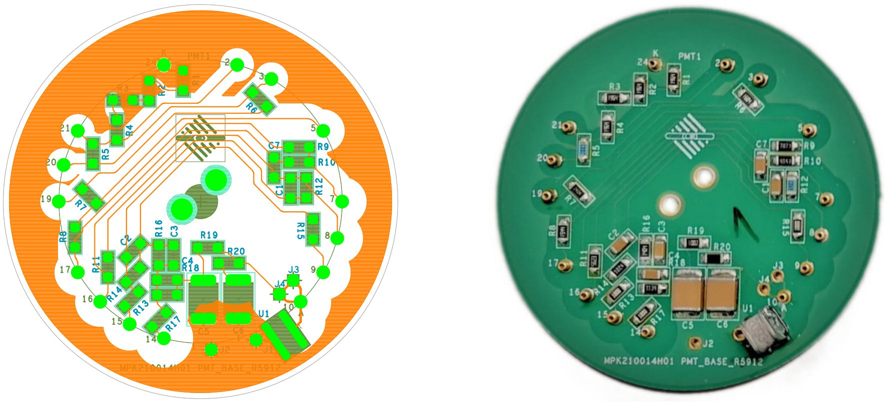

Figure 38 *Left:* Layout of the SMD base with mutual clearance constraints (PCB diameter of 66 mm). *Right:* Newly designed SMD base assembled with a gas discharge tube in the lower right part.

The calculated MTBF (Mean Time Between Failures) for the designed PMT base with about 30 passive SMD components is 7186 years at 15 °C and 10668 years at 5 °C component temperature. Referring these numbers to the expected ∼12000 PMTs of SWGO would result in roughly one failure per year. From this perspective, it is more likely that another part of the measurement chain has a failure. Since the base is potted and soldered to the PMT it is much more difficult to exchange this part compared to other components of the measurement chain. The calculated numbers also show that with a lower surface temperature the reliability can be extended. This would presumably be given by the positioning in the cold water volume with an expected temperature slightly above 4 °C.

5.2 BASE EVALUATION

The choice of the most suitable PMT base circuit has a strong impact on the performance of the whole measurement chain. The linearity and the rate stability as well as the timing are of major interest here and are values for comparison. Under test are three different PMT bases while two of them differ only in their assembly variant. There is the self-designed base PCB with SMD components that is based on the circuit recommended by Hamamatsu (see Figure 37). The two assembly variants have a total resistance of 14 Mohms on the one hand and 20 Mohms on the other. For both variants, the voltage distribution ratio along the dynodes is the same. In addition, there is a gas discharge tube (GDT) between the anode and ground to protect the system from voltage transients much higher than the maximum operation voltage. These could originate, for example, from lightning strikes in the surrounding area. The third PMT base is an existing one from the HAWC experiment. It is designed with through-hole components and has a total resistance of 20 Mohms. The circuit differs from the other two bases mainly at the last dynodes and the anode. The ratio of the voltage between the last dynode and the anode is half of that of the SMD base. Additionally it does not have a blocking capacitor in parallel to this resistor. Two different bases are shown in Figure 39.

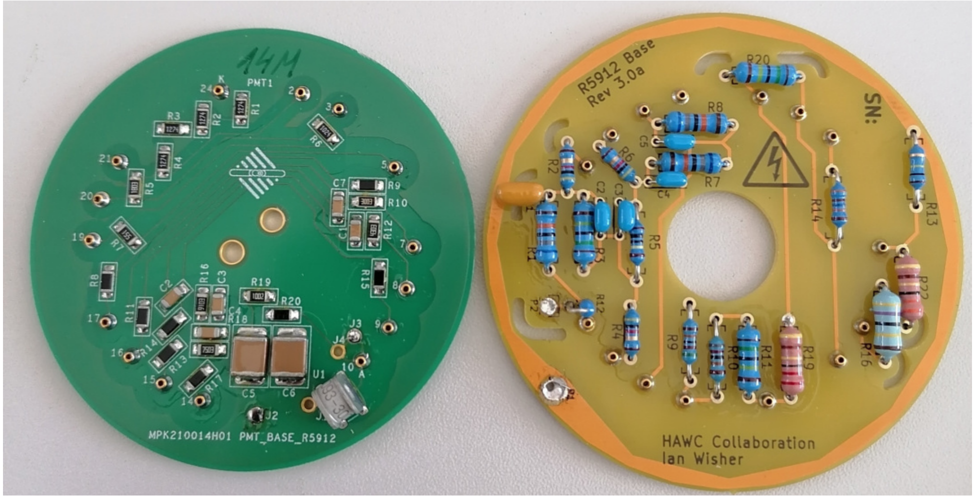

Figure 39 Assembled PMT bases with spring sockets for a fast attachement to PMT leads. *Left:* New designed SMD base with gas discharge tube (PCB diameter of 66 mm). *Right:* HAWC base with through-hole components.

The measurement took place in the dark box described in section 4.1. The different PMT bases were plugged into a recovered Hamamatsu PMT R5912 one after the other. To avoid soldering each base to the PMT leads, spring sockets were used on all bases. For each of the measurements a R5912-100 was used as a reference PMT in parallel. The procedure contained sets of different laser intensities while the PMT supply voltage was increased.

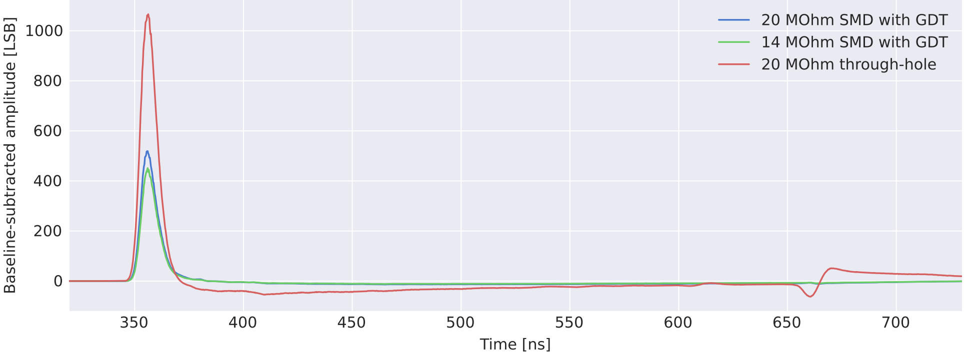

Figure 40 Pulse shapes of the different PMT bases under test. The 20 Mohms through-hole base used in HAWC shows a significant reflection.

The pulse shapes shown in Figure 40 are for all three devices under test almost equal. Even with the gas discharge tube on the SMD base the signal shape is not affected. The main difference is that the signal amplitude of the HAWC base is nearly twice as large as that of the SMD base. The reason for this is the missing termination in the HAWC base circuit. This leads to twice the amlitude compared to the SMD base but also causes large reflections on the signal line.

An impedance mismatch is not intended, as reflections are to be avoided with regard to the signal processing and the potential errors that would occur in the pulse reconstruction.

The second aspect which is investigated is the rate stability of the different circuits. The rate stability describes the behaviour of the output pulses after light-intensive input signals with a high repetition rate. For the measurement here the laser pulse keeps the intensity constant at a laser rate of 50 kHz, while the integral of the output pulses for the different bases vary strongly. For exaggerating the effect, the laser is set to few thousand photoelectron pulses. For the HAWC through-hole base already after 2 pulses the output integral starts to decrease dramatically whilst the other two circuits last 5 and 10 times longer (see Figure 41).

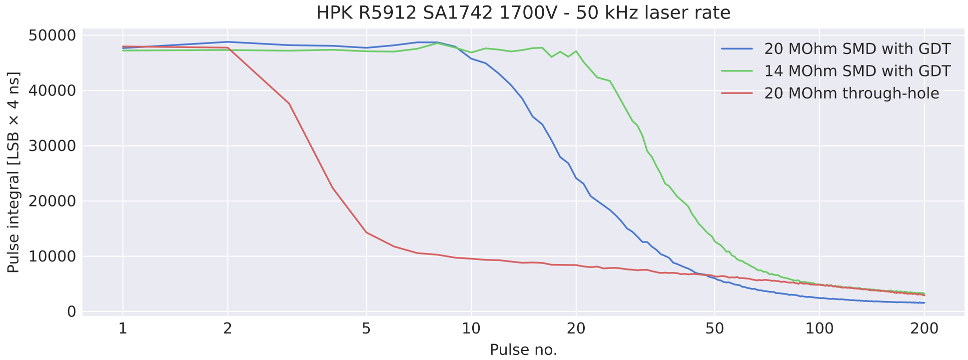

Figure 41 Rate stability of 3 different PMT base options.

The assembly variant with 14 Mohms is doing two times better than the one with 20 Mohms. This can be explained in the time to recharge capacitors on the base which increases as resistance increases. At a high pulse number above ∼50 events, the deviation between the blue and the red curve in Figure 41 should be caused by the higher amplitude of the through-hole base due to the missing termination. The trade-off for the bases is between power consumption and rate stability. A higher total base resistance leads the a reduction in bias current and thus lower power consumtion. In this case, the reduction would be around 30 %, but would have the drawback of less rate stability. Depending on the geometry of the detector volume and the reflectivity of surfaces, consequently, a higher rate stability may be required for possible larger, rapidly successive pulses. As long as the final WCD design has not been decided, the recommended base resistance of 14 Mohms will be implemented.

5.3 PMT POTTING

5.3.1 *Enclosure and Potting*

For getting the PMT waterproof an encapsulation around the PMT leads and the connected base is necessary. This means that the two critical contact points are between encapsulation and PMT glass tube respectively between encapsulation and coaxial cable. The concept for this contains mainly standardised components made of PVC-U. The focus is on low machining effort in the production of the individual parts. The encapsulation consists of a tube with an outer diameter of 110 mm and the matching end cap (see Figure 42). The end cap has a filling hole at the top, which is closed with a M25 blind screw after filling in the potting compound. A second hole with a M16 thread is on the side for the cable gland. The end cap is glued to the tube with a special adhesive for PVC-U. The connection between the PMT glass and the PVC-U tube is done with the adhesive DOWSIL 3145 RTV [21]. This adhesive and sealant cures at room temperature and has high tensile strength and elongation. It has been used in the HAWC experiment and has proven suitable. To maximize the contact surface of the glass, the end of the PVC-U tube has a phase of 45°. The encapsulated volume with the PMT leads and the base PCB soldered to it is potted with ELASTOSIL RT 625 A/B from Wacker Chemie AG [22]. It is a two-component silicone rubber for the encapsulation of electronic components. It vulcanizes in closed systems at room temperature and has a low viscosity in the uncured state. Since it is flowable, it is easy to fill in and spreads evenly around the leads and the base. When cured, it has high tensile strength and elongation, which helps prevent damage due to the different expansion coefficients of glass and PVC-U. For a bubble-free result, the two mixed components has to be put into a vacuum chamber for a few minutes to get the air bubbles out before it is poured in the encapsulation. After all described production steps have been carried out, the final result looks like shown on the right in Figure 42.

Figure 42 *Left:* Drawing of a Hamamatsu R5912 with encapsulation. *Middle:* Parts for the PMT encapsulation made of PVC-U. *Right:* Photo of a potted R5912 with encapsulation and cable.

5.3.2 *Cable*

The cable of a PMT is a small but not insignificant item which must be investigated. Because of the fast PMT pulses with rise times in the nanosecond region, a coaxial cable is required for the connection of HV and the PMT signal. Another electrical specification the cable must fulfill is the maximum operation voltage of 2 kV. In the application of a water Cherenkov detector the cable must first of all be waterproof. In addition the outer jacket of the cable needs to be robust against weather and mechanical stress e.g. caused by gravel when a desert-like environment is assumed for the detector site. A suitable cable would be the coaxial cable Belden YR29304 which is used in several other experiments with similar requirements like for example HAWC or the neutrino experiment Daya Bay [23]. It would fulfill the mentioned specifications but unfortunately this cable is not available. The number of available potential candidate cables is very small and even an extensive search could not bring up more. The only one found is the SC-Aqua Marinex 0.6/3.7 (600-0241AQ) from the manufacturer Sommer Cable. It has an impedance of 75 ohms and the geometry of a RG59 coaxial cable. The big advantage and unique selling point is that it is UV resistant and specified for permanent use under water (saltwater resistant). The outer jacket is of made of polyurethane (PUR). However, there is no specification for the required PMT supply voltage of up to 2 kV. Since other types of coaxial cable are specified for this operation voltage, it should be possible by the RG59 geometry to withstand that voltage. For this a test setup was built up to measure the leakage current between the core and the shielding of the coaxial cable. Therefore the high voltage insulation tester JP30A from Danbridge was used. The cable under test is 4 m long and fitted with a SHV connector on one end and insolated at the other one. The used test voltage of DC 5 kV was applied for several tens of minutes. The measured leakage current was below the resolution of the measurement device which is ±50 nA.

As part of section 5.5 the cable was also put into a barrel of water to investigate the behaviour within. There the two ends of the cable were led out to the lid of the barrel while 4 m cable were submerged in water (see Figure 43). After repeating the measurement of the leakage current during a period of one and a half years in water, no difference could be detected compared to the initial measurement. This shows that in principle the cable can withstand the necessary voltage of 2 kV and this even under the influence of water. In addition, the outer jacket and the insultation of the cable are not affected by being permanently underwater. This at least is confirmed with regard to an unchanged leakage current of the cable insulation. The certification of the cable for required voltage stability has been requested, but unfortunately not completed yet. Since the cable performed well even beyond the required maximum voltage, it will be used for the first prototypes.

5.4 DOUBLE PMT STRUCTURE

The concept of one candidate tank design for a water Cherenkov detector provides one upward and one downward facing PMT in a double-layer design (see section 1.4). This design might have advantages in mechanical aspects due to a combined mounting. For that reason a double PMT structure made of PVC-U was designed by the construction department (see Figure 44). It contains a holding structure for the 10-inch PMT as well as for the 8-inch PMT. Both are designed according to the same scheme, but dimensioned for the respective PMT size. For mounting it in the detector

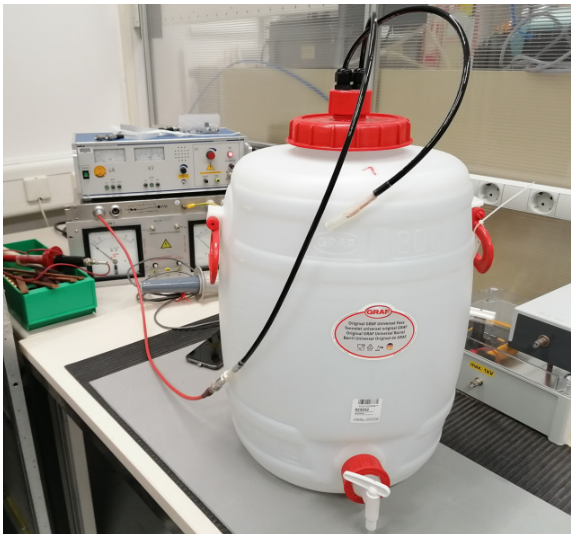

Figure 43 High voltage test of 4 m SC-Aqua Marinex coaxial cable submerged in water.

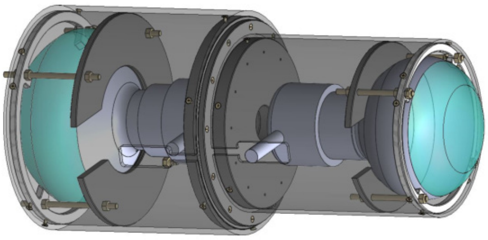

Figure 44 Technical drawing of the double PMT structure based on two individual holders for PMTs.

tank several fastening points are provided on the outside of the holding structure. Figure 45 shows a fully assembled double PMT from the side and submerged in water.

One issue of submerging PMTs in water is the high buoyancy due to its large volume. The buoyancy of an object follows the Archimedes' principle which says that the buoyancy force is equal to the weight of the displaced fluid. In the case of the two different PMTs assembled in the double PMT structure the weight is 17.5 kg. Putting this unit into water showed that around 3–4 kg were missing to achieve a stable vertical floating state. A large part of the buoyancy sits far down in the structure with the 8-inch PMT causing it to tip into a horizontal position. To compensate the missing weight, a clamp sleeve made of A4 stainless steel with a total weight of 5 kg was designed and produced. The clamp slave is made of a 5 mm thick metal sheet to avoid corners and edges that would be difficult to clean. This approach of a clampable weight replaces previous attempts with several thinner metal layers on top of each other. Finally by adding the additional weight to the lowest point of the holding structure a stable condition is

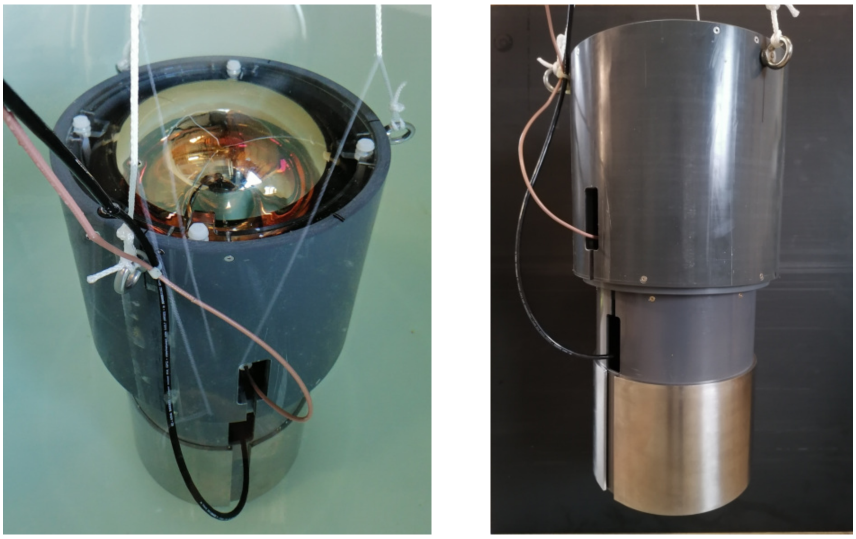

Figure 45 Double PMT structure with a 10-inch PMT facing upwards and a 8-inch PMT facing downwards.

reached. The three ropes which are holding the structure in place are loaded with roughly 2 kg in total. The total weight of the assembled double PMT structure with clamp sleeve weight is around 23 kg.

A rough cost estimation for the double PMT structure is listed in Table 6. For a small quantity of about 10 pieces, the costs without labour and machining are 200 € per piece. The stainless steel weight accounts for half of the costs. The high costs for labour and machining can be reduced by producing a larger quantity of the single pieces for the double PMT structure.

Item	**Costs**
PVC Tube for 10-inch PMT	20 €
PVC Tube for 8-inch PMT	10 €
PVC plates	45 €
Polycarbonat plates	15 €
Weight A4 steel	100 €
PA threaded rods with screws	10 €
Labour and Machining costs 4 h	400 €
Total	**600 €**

Table 6 Summary of cost estimation for a double PMT structure. Costs are given per unit and assuming small quantity and 2023 prices.

5.5 WATER QUALITY MONITORING

In a water Cherenkov detector the produced Cherenkov light is of interest. Before this light is collected by a photosensor, it usually travels some meters through water. From that perspective the lowest possible attenuation in water at the specific wavelenghth should be aimed for to maximise the photo detection efficiency and thus the detector signal. Moreover, the detectors are built for use of over several years and contamination in water can damage the detector components over time. These reasons mean that a stable water quality is needed. The materials chosen for the detector should not dissolve in water over time and contaminate it. In order to gain knowledge in this subject, a test setup was built to investigate the behaviour of different materials in water. The transmissometer used here is from Seabird Scientific, C-star, CST-2092PV which uses laser light with a wavelength of 410 nm along a path length of 25 cm. It gives out among others the reciprocal of the attenuation length in meter, the so-called attenuation coefficient. The different water samples are stored in white plastic barrels with a water volume of 30 l. They are food-safe commercial containers made of polyethylene. Their opening lid is big enough to insert the transmissometer for the measurement. The measurement setup with the samples stored in barrels can be seen in Figure 46. The interval of the measurements varied between once and twice a month. In the procedure, the transmissometer is immersed in one barrel after the other, with cleaning its surface with lint-free wipes in between. In addition, the conductivity of the water samples is measured with the conductivity meter G1420 from Greisinger. It has a conductivity range from 0.00 to 20.00 μS with an error of ± 1 % of the measured value.

Figure 46 Measuring station for the water quality measurement with the samples stored in barrels. The transmissometer stands next to the notebook.

The samples under test range from screws to plastic foil for bladders to PVC components and many more. Described here are only some relevant materials for the PMT encapsulation and PMT supporting structure. The water used for the different samples was mainly reverse osmosis water, which builds the basis in terms of attenuation length due to its treatment. Additionally, for some samples filtered water is used, because this kind of water would be way easier to provide in the later project. In Table 7 the measurement results for the attenuation coefficient $\lambda(1/m)$ and conductivity $\sigma(\mu S)$ for the mentioned time period are shown. The important value is the attenuation length λ_i, which gives the last or most recent measured value. In Figure 47 the attenuation coefficient over time for some of the measured materials is plotted.

Material	λ_i	λ_f	$\sigma_i(\mu S)$	$\sigma_f(\mu S)$	**Start Date**	**Last Date**
Tap Water	0.54	0.8	-	-	18.05.2021	14.07.2021
Filtered Water (control)	0.379	0.353	-	-	18.05.2021	14.02.2023
Reverse osmosis Water (control)	0.079	0.117	8.22	8.14	18.05.2021	14.02.2023
A4 screws	0.03	0.214	8.42	7.67	18.05.2021	03.03.2022
A2 screws	0.028	0.157	8.14	7.83	18.05.2021	22.08.2022
PMT support PVC	0.033	0.147	8.26	8.16	18.05.2021	03.03.2022
Coaxial Cable 600-0241AQ	0.06	0.273	9.35	9.31	15.07.2021	14.02.2023
Plug Phoenix 1415207	0.065	0.46	6.98	7.35	10.03.2022	10.06.2022
Plug RS 211-6794	0.065	0.695	7.49	8.12	10.03.2022	04.05.2022
Plug HPM25 BK080	0.059	0.175	7.02	6.52	10.03.2022	10.06.2022
Common Shrinkable Tube	0.059	0.126	7.02	6.39	01.04.2022	14.02.2023
PTFE Shrinkable Tube	0.08	0.090	8.45	7.73	14.06.2022	14.10.2022
RT-375 Shrinkable tube	0.079	0.121	8.7	7.77	14.06.2022	14.02.2023
PMT R5912	0.065	0.306	7.04	5.12	08.02.2022	14.02.2023
PMT R7081MOD-ASSY	0.062	0.155	7.45	6.31	08.02.2022	14.02.2023

Table 7 For all materials tested, the beam attenuation coefficients (λ) and conductivity (σ) as they were measured on the first date the material was added and the last measurement date. Unless otherwise stated, the materials are housed in reverse osmosis water.

All results must be viewed critically, as the ratio of the amount of water in the barrels to the sample size can deviate extremely from the later detector. One example is the coaxial cable where 4 m cable put into the 30 l sample compared to the later detector volume which requires the same cable length but at a water volume of approx. 10^3 times more.

Figure 47 shows for most of the samples an increase of the attenuation coefficient in the initial measurement phase (∼3–6 month). From there on the changes seem to slow down and converge to an stable seeming value. The measurement results of the self-potted PMT R5912 in the plot (Figure 47b) shows a drastic increase of the attenuation coefficient after the first measurements. This may have been caused by impurities in the water or residues on the PMT. As a result, the water was replaced and the surface of the PMT was cleaned. This explains the short peak of the green curve right at the beginning of the measurement.

The results of the stainless steel screws (Figure 47c) did not meet the expectations. In literature A4 grade stainless steel is described as more robust against water and especially seawater compared to A2 grade due to its added Molybdenum. The measurement results here show the opposite of the expectations. To verify the first result, new samples of the two types of screws has been prepared and measured. After 3 months in water the

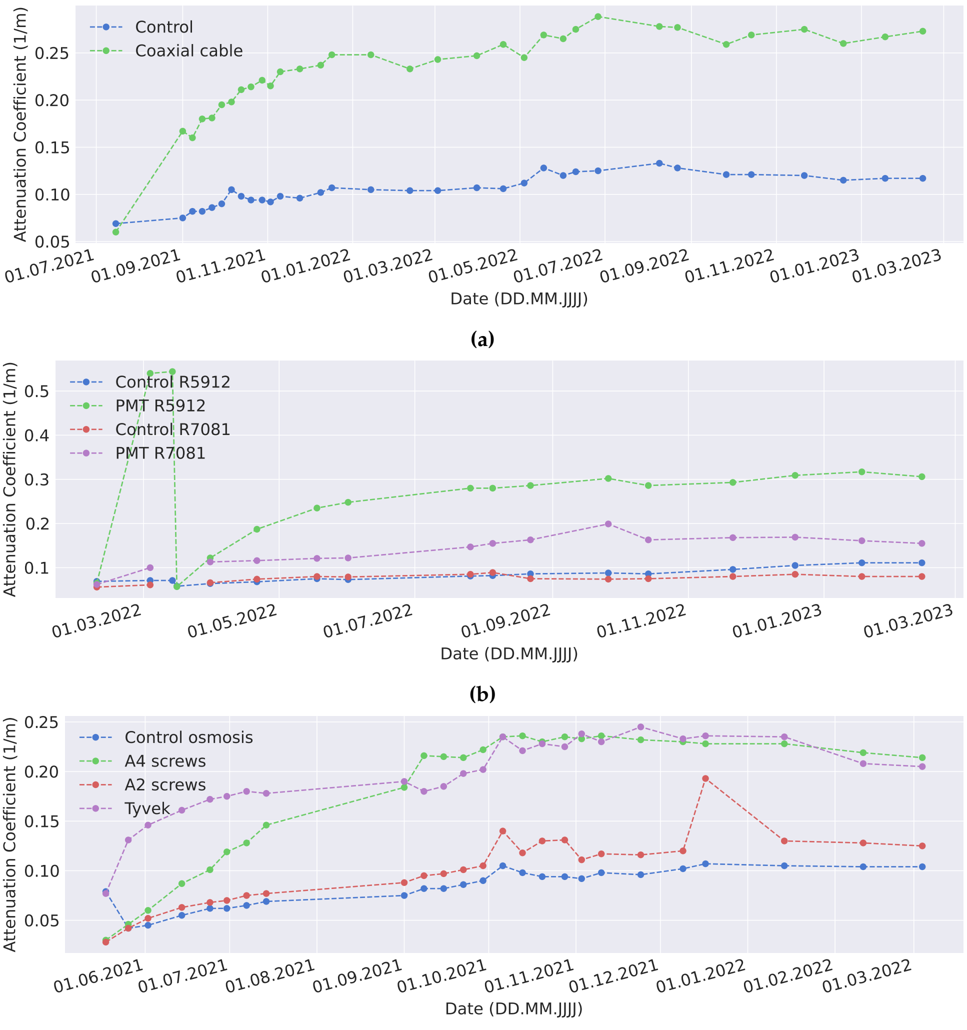

(a)

(b)

(c)

Figure 47 Attenuation coefficient of osmosis water over time for the (a) coaxial cable Aqua Marinex, (b) the PMTs R5912 (self-potted) and R7081 from Double Chooz (c) some other materials related to the detector mechanics. For the plot (b) the water of the self-potted PMT R5912 was changed after 3 measurements due to a quite strikingly bad attenuation length.

two different screws behave almost the same within 3 % in terms of the attenuation coefficient.

This example shows clearly that there are some uncertainties in the measurement. By putting the transmissometer from barrel to barrel for each measurement, contamination could still occur despite cleaning in between. Nevertheless, the measurement helps to identify very conspicuous materials and to generate a kind of short list. In the described study, a number of materials were identified that are assumed to show good properties in water. This long-term measurement is still ongoing and provides a very helpful and presumably unique data set for future decisions on materials.

6

DATA ACQUISITION NODE

In this chapter the concept and the implementation of prototypes for a so-called data acquisition node (DAQ) or field node are described. The cabinet provides necessary infrastructure and environmental control for the measurement electronics which collects the physics data. First, the concept behind the DAQ node with its hardware components is covered. This is followed by a description of the operational states and the associated failure modes. Additionally, the reliability of the system is analysed with a proposal for a maintenance plan. Finally, a field test planned in Peru is presented.

For the project SWGO around 6000 detector units are planned, which, depending on the design, would result in 12,000 PMTs. From this number a sensible dimensioning of the electronics nodes is required. A trade-off between cable length, labor for cabling and the offset costs for an outdoor cabinet must be found. However, since the exact design of SWGO and its parts has not been defined yet, only assumptions can be made for building prototypes. A reasonable number of channels per cabinet are around 140–170, taking into account a maximum cable length to the PMTs of approx. 50 m. A total of 168 PMT channels could be covered with the manageable number of 7 PhantomHV systems and one crate of FlashCam ADCs.

6.1 PROTOTYPE DAQ NODE

A suitable outdoor cabinet for housing and protecting all measurement electronics is required. In order to enable trouble-free operation the whole system should be ideally independent of external environmental influences. A comprehensive concept for the environmental control system is therefore very important. To achieve this degree of freedom, a variety of devices must be deployed. Probably the most important feature is that the DAQ node itself is able to operate always in a safe condition, even if it is not accessible via network. It must be able to operate self-sufficiently in order to avert possible damage of any kind. Besides environmental control, the cabinet provides commonly needed infrastructure: power, slow control and monitoring, and Ethernet network.

6.1.1 *Outdoor cabinet*

The outdoor cabinet offers protection against external influences so that the sensitive measurement electronics can be operated safely for a long time. Expected on site are rough environmental conditions such as seismic activities, high UV exposure, precipitation in combination with a wide temperature range and strong winds. All this illustrates the relevance of a stable and solid outdoor cabinet. A first proposal aims to rely on the expertise of suppliers for the energy, telecom and transport sectors to provide an outdoor cabinet with the following specifications:

- double-walled, four-door outdoor enclosure with rain canopy and earthquake reinforcements providing an IP55-rated sealed environment
- plinth with removable side panels to feed in cables
- modular EMC feed-through panels in the doubled-up floor
- combined drainage & pressure valve to drain any condensation and prevent under- and overpressure
- cut-out in one door for a cooling unit (see section 6.1.3)
- two inner ∼28 RU 19-inch racks with profile rails on front and back, ∼80 mm depth and optional L brackets for fixing long and heavy components

Note that the eventual dimensions will depend on the final electronics design and channel count per DAQ node (although a low centre-of-mass will help against damage from seismic activities). It is therefore desirable to work with companies that provide customised solutions from the start. Cabinets from two such companies have been obtained: (see Figure 48):

- Rittal, an internationally-acting manufacturer of electrical enclosures that provides the CS Toptec outdoor cabinet series in several configurations of width, depth and height.
- Häwa, a German company that specialises in custom-designed, low-volume enclosures, that customised an existing heavy-duty, stainless steel seismic cabinet design according to the requirements.

Figure 48 Two prototype DAQ nodes operating next to the SWGO test tank at MPIK, Heidelberg. *Left:* Rittal CS TopTec cabinet with Blue e+ KG chiller; *middle:* Myself for scale (∼1.9 m high); *right:* custom-made Häwa cabinet and Seifert air-to-air heat exchanger unit.

As the cable feedthrough, the IP55-rated Icotek split EMC cable entry frames in the floor panels of both cabinets are used. Up to 10 cables of diameter up to 17 mm can be fed through one frame. The shielding of any cable may be connected to the housing's potential to divert any electromagnetic pick-up. Since the final design or the number of PMTs per cabinet is not decided yet, a first proposal includes around 140-180 PMTs operated by a single cabinet. This results in many cables that have to be fed into and managed within the cabinet. Therefore, a plausibility test was carried out with a bundle of cables to confirm the possible cable laying. Figure 49 shows the dummy terminal to imitate the interface for the coaxial cables of the PMTs. Shown is a total of 48 cables which would correspond to two fully equipped PhantomHV systems.

Figure 49 *Left:* Front view of the cable routing inside a cabinet with 19-inch rack. On the left half the cables are fed from below and on the right half from the back. *Right:* Photo of the cables fed in a single bundle from the back of the rack to each half of the PhantomHV dummies.

6.1.2 *Power and Auxiliaries*

The internal power distribution and slow control is entirely based on standard commercial off-the-shelf (COTS) components, specifically:

- Dehn DSH TN 255 FM[1] lightning current and surge arrester for 230 V single-phase TN systems with remote signalling contact
- PULS CP20.241-R2-C1[2] 24 V DC power supplies with wide-range 100–240 V AC inputs, conformal coating and N+1 redundancy without an additional module
- WAGO 750-8211/040-000[3] PFC200 programmable logic controller (PLC) with wide operating range, two 10/100BASE-T and two 100BASE-FX Ethernet ports, and a modular, extensible field bus system for analogue and digital I/O modules
- Gude 8031-2 Power distribution unit (PDU) with power, current and voltage monitoring for its 8 IEC C13 outputs (max. 10 A). Two temperature and rel. humidity sensors are optionally connected. The operation temperature is only 0–50 °C.

The resulting power budget of a fully equipped electronics cabinet is listed in Table 8. With 4 power supplies, 480 W each, the total power consumption of the maximum load, where all devices are running on 100 %, could be covered with a power buffer remaining. For a N+1 redundancy, where one unit could fail without any effect on the operation, an additional power supply unit must be installed. That all devices are running at the same time at 100 % is very unlikely and thus the provided power is sufficient. For the prototype described here, the required power is lower because the maximum number of channels is not utilised. For this case, a total number of 4 power supplies including redundancy is sufficient.

Component	**Quantity**	**Power Consumption per Channel**	**Total Power Consumption**
PhantomHV	168	0.85 W	142.8 W
FlashCam ADC	168	1.1 W	184.8 W
PLC with I/Os and Sensors	1	–	100 W
Air-to-Air Heat Exchanger	1	4 x 106 W Fans + 2 x 200 W Heater	824 W
Fan Tray	3	3 x 45 W	405 W
Dehumidifier	1	-	50 W
Total			**1706,6 W**

Table 8 Power consumption of a fully equipped field node (168 channels) with environmental control. All numbers given at 100 % duty cycle.

---

[1] https://www.dehn-international.com/store/p/en-DE/F42828/appl-opt-combined-arrester-dehnshield-type-1-2-for-three-phase-tn-s-systems-?product=P909702

[2] https://products.pulspower.com/en/cp20-241-r2-c1.html

[3] https://www.wago.com/global/plcs---controllers/controller-pfc200/p/750-8211_040-000

An exemplary power distribution scheme is shown in Figure 50. Note that the design of the power distribution is modular enough to be adapted to, e.g., lower-voltage AC or DC power networks if considered beneficial. Many components could be easily replaced by other suitable and available industry-standard parts.

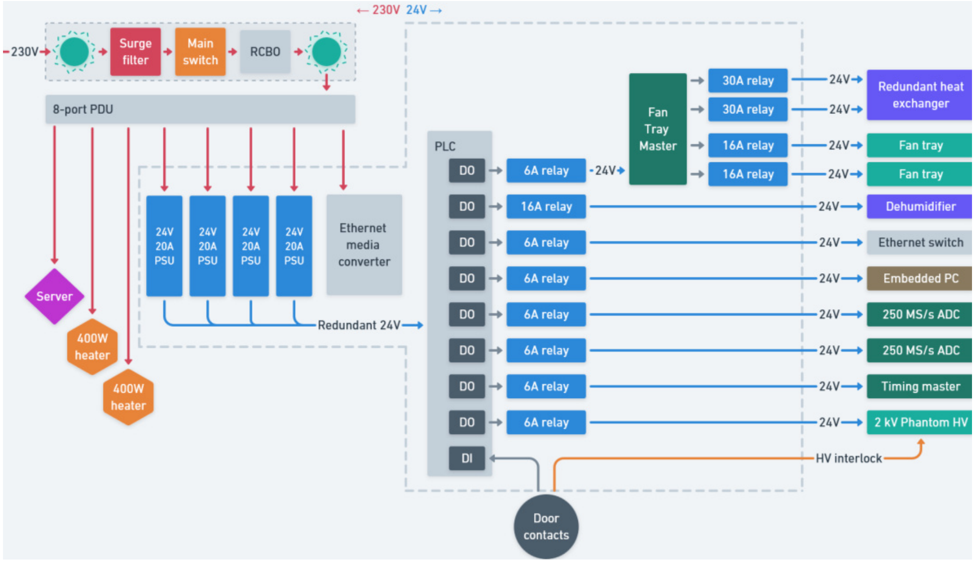

Figure 50 Power distribution scheme with a 230 V section on the left and a 24 V section on the right

For reasons of clarity and production, the mentioned components are located in a control box called PAX (Power and Auxiliaries). This box has a height of 60 cm with 4 DIN rails mounted, which can be seen in Figure. 51. In it, from the lowest to the highest DIN rail, there are 4 power supplies and the media converter, current sensors for each power supply and solid state relays, a clamping block for power distribution, the PLC with fuses and the GECCO-based fan tray master. In addition to the PAX box, there is also a separate 2 U box for the 230 V components like the main switch, indicator lights and RCD (Residual current operated circuit-breaker with overcurrent protection). By mounting all power related components in boxes, they can be prefabricated and tested before being installed in the outdoor cabinet. The separation of 230 V and 24 V components is intended to allow a better overview of the system and thus increase safety.

For an effective monitoring several different sensors are needed in the DAQ node (see Table 9). There is a combined sensor which measures the rel. humidity as well as the temperature. To detect potential water ingress from the outside or condensation from the dehumidifier there is a leakage sensor on the floor of the cabinet. In order to detect a possible defect of the lightning protection surge filter, it is equipped with a signalling contact. Since the monitoring of the power supplies is important for trouble-free operation the output current of each supply is measured. Additionally, DC-OK signals of all power supplies and the level of the 24 V output voltage are read in. Also the total AC input current of the 230 V side of the whole

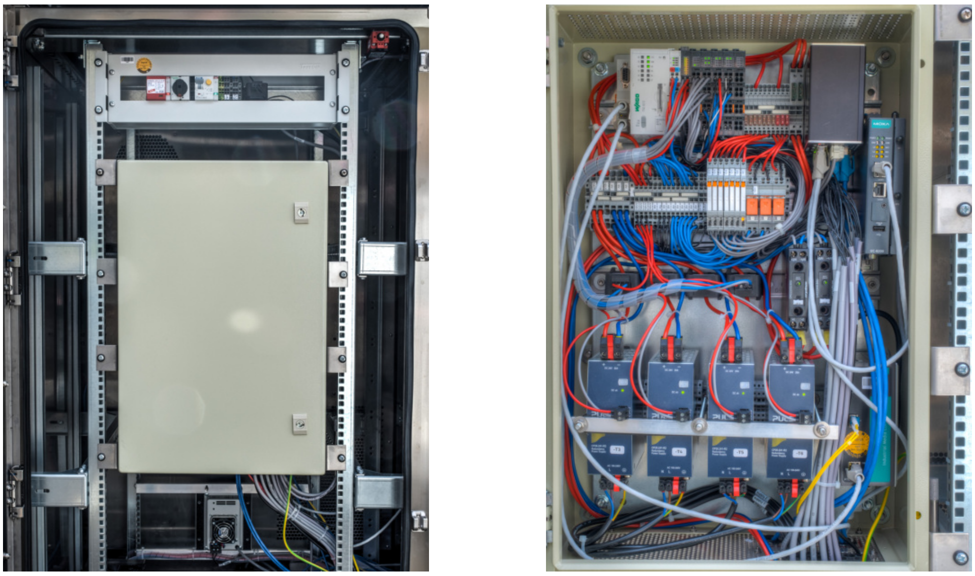

Figure 51 Power and Auxiliaries Box (PAX) in a 19-inch rack. *Left:* 230 V components in a separate unit at the top. Below the 60 cm high box for the 24 V system components. *Right:* Opened box with four DIN rails for placing all components. The heavy power supplies are equipped with a holding bracket to avoid swinging.

system is measured. Mainly for the safety of humans, an interlock system with door contacts is installed. As soon as one of the four doors is open, the HV is disabled. By all the mentioned sensors and the resulting measured values the DAQ node can be well monitored and thus enables a detailed troubleshooting in preparation for any necessary maintenance trips.

Variable	Range	Interface Input	Note
Temperature	-30–80 °C	0–10 V	Combined housing
Rel. humidity	0–100 % r.H.	0–10 V	
Leakage	-	binary	Sensitivity adjustable
Current	0–25/50 A	0–10 V	Response time filtered
Voltage	0–30 V	0–30 V	
Door status	-	binary	NC contact / 4 in series

Table 9 Sensors and measured variables with measurement range for monitoring.

An alternative product to the installed PULS power supply (CP20.241-R2) the model QUINT4-PS/1AC/24DC/20/+ from Phoenix Contact could be deployed. It also allows a parallel operation for redundancy without an additional module and is available with conformal coating. The product from Phoenix Contact has almost the same dimensions except the width which is around 2 cm wider. In addition, it provides more features like configurable switching contacts for status signals. However, since very good experiences have been made with PULS power supply units in previous projects, they are used for the prototype.

6.1.3 *Environmental Control*

The environmental control system has the task to stabilise the environmental conditions inside the cabinet for protecting the electronics and minimise thermal stress. This is realised by means of cooling, heating, ventilation and dehumidification.

Cooling. The main technologies available for closed-loop cooling are vapor-compression refrigerators and thermoelectric coolers. Both types of devices contain sensitive active elements and/or require regular maintenance. Furthermore, the major manufacturers do not certify these devices for high altitudes. It is proposed to evaluate an air-to-air heat exchanger as a potentially more reliable, maintenance-free alternative. A back-of-the-envelope calculation results in $\sim$10–15 $\mathrm{W\,K^{-1}}$ of heat flow for a free-standing double-walled cabinet of that size. Assuming 1 kW of heat load and a maximum outer temperature of 20 °C, $\sim$90 $\mathrm{W\,K^{-1}}$ of cooling capacity is required to limit the inner cabinet temperature to 30 °C. Some buffer should be considered for solar load, which strongly depends on the surroundings. These numbers are based on the online calculator tool *Calcoolator* from Seifert. There is still the option to put insulation plates to the inside of the cabinet if necessary. Currently tested is a custom prototype developed together with Seifert Systems GmbH that includes two fully redundant 75 $\mathrm{W\,K^{-1}}$ circuits (see Figure 52 right). The cooling unit contains a total of four 24 V DC fans which are speed-controlled and monitored using a custom slow control system (GECCO) that is being used in several other experiments at MPIK. The control board of the cooling device is split into two identical circuits for redundancy. It is connected to the fans, the temperature sensors and two heating elements inside the device. There are two temperature sensor installed for each of the circuits, one at the air inlet from the outside and one at the outlet to the inside of the cabinet. As a mechanical protection it includes a sand trap at the inlet to provide potentially maintenance-free operation. Figure 52 on the left shows the front of the cabinet with the air-to-air heat exchanger installed in the right door. While the sand trap is protecting the air inlet, the two air outlets of the redundant circuits are covered with bonnets to avoid ingress of water or sand.

Heating. In case that the desired operating temperature is not reached, for example due to a low ambient temperature, heaters are available. Two 230 V fan heaters with integrated thermostat (FLH-T 400 / Pfannenberg) and a power of 400 W each are implemented in the cabinet (see Figure 53). Additionally two 200 W heating elements are integrated in the air-to-air heat exchanger. Due to the thermal conductivity of the cabinet, a few hundred Watts of heating power are needed to heat up the cabinet from -20 °C to 5 °C in a cold-start scenario. This special scenario is described in Section 6.2. Since the number of planned channels in the prototype cabinet is much less than what would be possible, the heaters can also be used to simulate the heat loss of electronics.

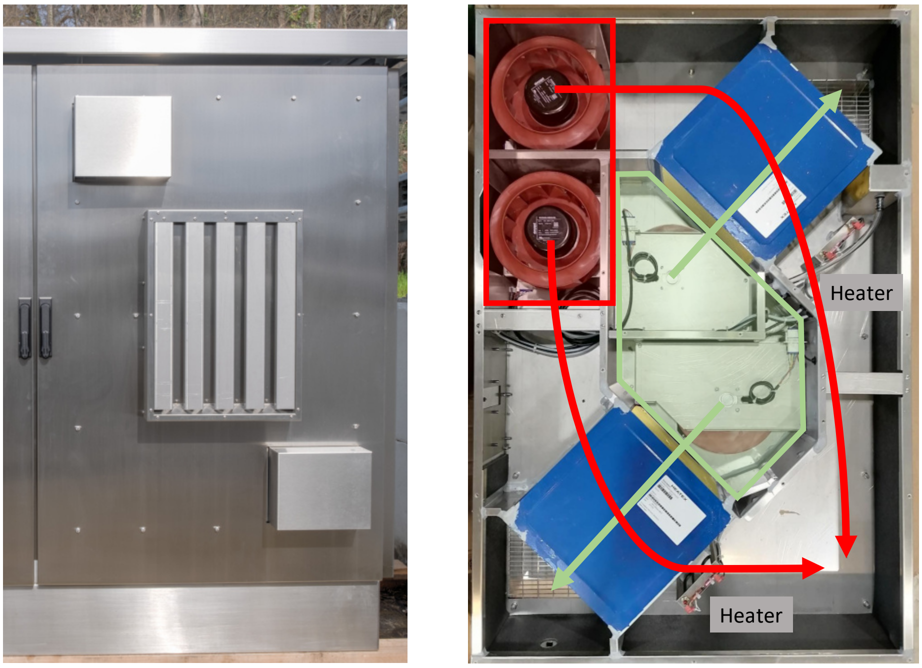

Figure 52 *Left:* Front view of the Häwa outdoor cabinet with the prototype air-to-air heat exchanger installed in the right door. *Right:* Inside view of the air-to-air heat exchanger (120 cm x 80 cm) with two redundant circuits. The inlet air from the outside goes from the middle of the device through the two heat exchanger to the lower left and upper right corner to the air outlets. Each heat exchanger has orthogonal air flow and keeps the inner circuit separate from the outer circuit. The air to be cooled from inside of the cabinet flows through the heat exchanger from the top left to the outlet into the cabinet at the bottom right.

Ventilation. Most components that are part of the DAQ node may be passively cooled via convection. One exception are the physics components like ADCs, FPGAs or the HV modules which may need either front-to-back ventilation or forced convection due to their relitvely high power density. Therefore, high-reliability fan trays in the racks for forced convection distribution inside the cabinet are foreseen. For this purpose, the in-house developed fan trays include 3 individually speed-controlled fans from Sanyo Denki which are built in a 2 U housing (see Figure 53). The fan trays are controlled and monitored with the same GECCO-based system as the air-to-air heat exchanger.

Dehumidification. It is desirable to maintain a low humidity within the cabinet to reduce component stress (which grows with relative humidity and temperature), reduce the probability of high-voltage arcs, and prevent condensation on surfaces. [24] For this, a Peltier-based dehumidifier which drains any condensation to the outside of the cabinet is installed (see Figure 53). Note that such dehumidifiers are ineffective at temperatures below or close to the freezing point. To prevent condensation within the cabinet, temperature and humidity sensors deliver measurement values to the PLC which is programmed to calculate the dew point distance of the coldest sensor and to enable the dehumidifier if needed. The dew point describes the temperature value where the humidity in air begins to condensate. The

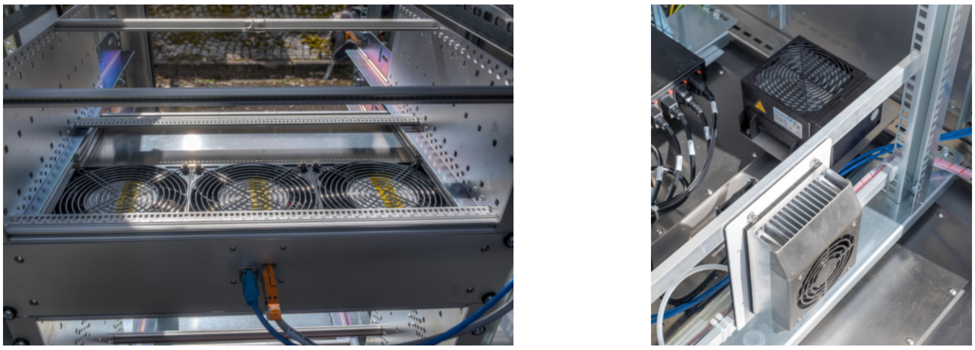

Figure 53 *Left:* Customised fan tray in a 2 U housing. *Right:* Dehumidifier (silver housing) with a small hose for the condensate. 400 W fan heater (black housing) installed at the floor of the cabinet.

dew point distance is a measure of the temperature difference at which condensation begins.

The estimated cost of a field node equipped with the proposed components excluding measurement electronics is listed in Table 10.

Element	Procurement Costs
Cabinet	10 k€
Power & slow control	4 k€
Environmental control	5 k€
Network	1 k€
Total	**20 k€**

Table 10 Summary of cost estimation for this solution. Costs are given per field node and assuming production of 50 nodes at 2022 prices.

6.2 OPERATIONAL STATES AND FAILURE MODES

A first prototype of the PLC firmware has been developed in *Structured text*.[4] It includes readout of voltage, current, temperature, and humidity sensors and allows the individual control of the power to all subsystems. The sensor readings are continuously analysed to derive warnings, alarms and autonomous actions if conditions deteriorate. This should ensure that all equipment is protected even when a node is not accessible via network from outside. Part of the feature set can be seen in Figure 54. This web user interface displays the read-in sensor data, shows warnings and alarms and enters acknowledgements of alarms as well as the command for switching power for the devices. A warning is indicative only and may vanish without any acknowledgement while an alarm requires manual intervention and autonomously takes an action. The PLC determines based on the sensor data in which operational state the system is, executes autonomous actions if conditions deteriorate and restricts the use of devices for protection reasons

---

[4] `https://en.wikipedia.org/wiki/Structured_text`

if necessary. There are four possible operational states which divide the components of the DAQ node into the groups monitoring, environmental control, and physics package. Table 11 shows the effect of the operational states on the component groups. The most restricted group is the physics package like e.g. ADCs or HV modules, as these are the most sensitive components to environmental influences. A more detailed breakdown of all different warning and alarm conditions and their effect on the state is shown in Table 12. The definition of a warning compared to an alarm for e.g. low temperature is in the value which is 0 °C respectively -10 °C. This means that a warning informs about a still acceptable condition while an alarm appears and protects against an unacceptable condition.

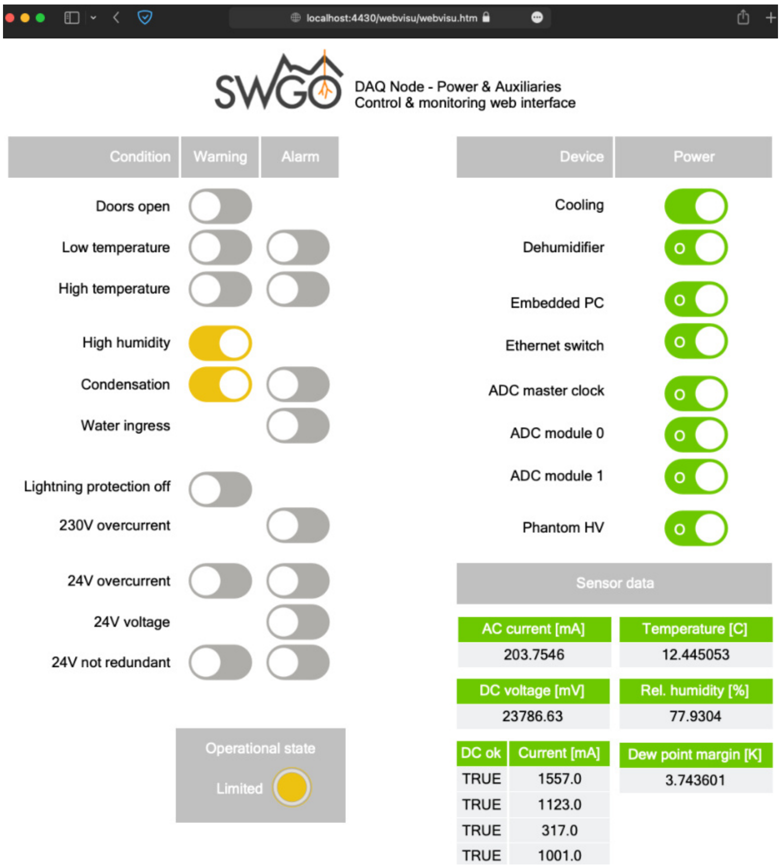

Operational state: Limited

AC current [mA]	Temperature [C]
203.7546	12.445053

DC voltage [mV]	Rel. humidity [%]
23786.63	77.9304

DC ok	Current [mA]
TRUE	1557.0
TRUE	1123.0
TRUE	317.0
TRUE	1001.0

Dew point margin [K]
3.743601

Figure 54 Prototype web UI of the DAQ node PLC.

Operational state	Monitoring	Environmental control	Physics package
Operational	on	on	available
Limited	on	on	kept as is
Safe	on	on	off
Disabled	on	off	off

Table 11 Operational states of the PLC.

State condition	operational	limited	safe	disabled
doors_open_warning	x			
lightning_protection_ineffective_warning	x			
psu_not_redundant_warning	x			
high_humidity_warning	x			
condensation_warning		x		
low_temperature_warning		x		
high_temperature_warning		x		
psu_overcurrent_warning		x		
condensation_alarm			x	
low_temperature_alarm			x	
high_temperature_alarm			x	
water_ingress_alarm			x	
psu_dcok_alarm			x	
psu_overcurrent_alarm				x
psu_voltage_alarm				x
ac_overcurrent_alarm				x

Table 12 Detailed description of the operational states.

The potential impact in case of failing components are shown in Table 13. Possible single points of failure and thus weaknesses in the system can be pointed out. This can indicate where redundancy of components is beneficial for a long and ideally failure-free operation. One single point of failure lies in the 230 V supply path with its components like main switch, RCBO or PDU. A failure there would cause a total breakdown of the system. A very similar impact would result from a failure of the PLC and its I/O modules. In this case, control would be lost for either the connected devices of the failed I/O module or in the worst case the whole PLC system.

Failing Component	Impact	
1 out of 4 power supplies	No	No more redundant
2 out of 4 power supplies	Power budget too low	Operating in safe state
Current sensor	No measured value	Operating in disabled state
Relay	No power	Switched device not usable
Fuse for relay	No power	Switched device not usable
PLC	No control	No function, only PDU controllable
I/O module of PLC	No control	Connected relays or sensors not usable
Fan Tray Master	No control over Fans	Heat exchanger / fan trays not working
1 circuit of the Air-to-Air Heat Exchanger	None	No redundancy
230 V surge filter, main switch, RCBO	No power	System down
230 V PDU	No power	System down
1 out of 2 heaters	Limited heating power	Operational temperature may limited
Ethernet media converter	No fiber connection	Autonomous running / safe state

Table 13 Overview of failure modes and their impact on the operation of the system.

A special scenario in the operation of the electronics cabinet is the cold start scenario. This includes a turned off cabinet without any environmental control and an inside temperature < 0 °C . If the unit is now tried to be switched on, problems with the PDU could occur, as it is only specified down to 0 °C . Without a properly working PDU no power supply can turned on and thus the PLC either. This would not allow the cabinet to be operated. As there are no comparable PDUs on the market with an extended temperature range, this PDU is used for the prototype described.

A possible solution to eliminate this single point of failure would be to install a relay block controlled by the PLC (see Figure 55). Since the PLC is good for operating down to -40 °C , it would just need a separate 24 V power supply which is always on when AC voltage is present. From there, devices can be switched on successively according to their operational range of temperature and rel. humidity. Typically, it would be started with the heaters and, if necessary, the dehumidifier. This solution also has the advantage that only one device in the network is responsible for switching further devices.

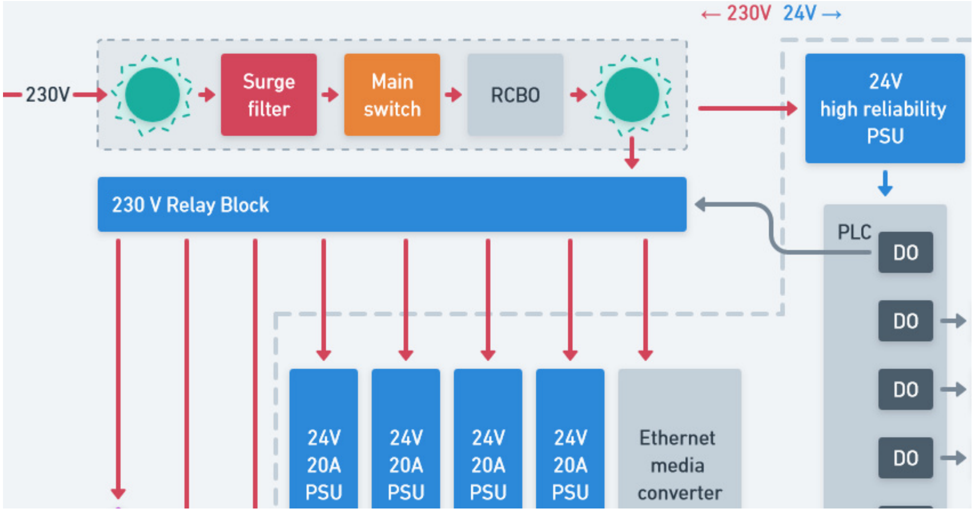

Figure 55 Alternative power distribution scheme (zoomed in) with a separate 24 V power supply for PLC always on. Relays controlled by the PLC replacing the power distribution unit.

A different way of visualising measurement data associated with the field node is shown in Figure 56. It displays environmental, power and physics measurements clearly in one window. This summarises all necessary data for a full regulation and troubleshooting of the field node.

Figure 56 The visualisation of field node related data in one window. The dashboard includes in the top row environmental data, in the middle row measurements of the supplied power and in the bottom row physics data like trigger rates from the FlashCam readout and PMT voltages from the PhantomHV system.

6.3 RELIABILITY ANALYSIS

The majority of implemented electrical components in the DAQ node are commercial products. Because of that, they typically have a value given for the reliability parameter MTBF (Mean Time Between Failures). This value describes the predicted average time between system breakdowns. The duty-cycle, load, ambient temperature and many more contribute to the MTBF. To maximise this number, it is intended to select components with industrial environmental rating or extended operating range if possible. Redundancy of components to increase reliability is attempted where it is possible with reasonable effort. Single points of failure are mostly concentrated in the 230 V power system, e.g., the lightning protection, RCBO, and PDU. Single failures in the PSUs, cooling, heating and network can be tolerated due to redundant components and/or connections. The modular set-up and high degree of monitoring helps in identifying and exchanging failed components.

For most commercial components the MIL-HDBK-217F as a widely used standard for the determination of the MTBF value is used. The latest version of this standard is around 25 years old and thus, considering today's quality standards of electronic components, much more conservative. However, for a comparison between devices rated to the same standard, it still works well to find the more reliable ones.

The basic mathematical expressions for calculating the reliability $R(t)$ with a constant failure rate λ and the MTBF are:

$$R(t) = \exp(-\lambda t)$$

$$MTBF = \frac{1}{\lambda}$$

A slightly more complex model with two parameters is the Weibull distribution. It is more flexible than the one with a constant failure rate and allows a better fit to components which get a higher failure rate the longer they are operated. A good example for this behaviour are fans, which become more prone to failure over time due to mechanical wear. The failure rate $\lambda(t)$, reliability $R(t)$ and the failure distribution (also called probability density function) $f(t)$ are shown below.

$$\lambda(t) = \frac{\beta}{\gamma} * \left(\frac{t}{\gamma}\right)^{\beta-1}$$

$$R(t) = \exp - \left(\frac{t}{\gamma}\right)^{\beta-1}$$

$$f(t) = \frac{\beta}{\gamma} * \left(\frac{t}{\gamma}\right)^{\beta-1} * \left(\exp - \left(\frac{t}{\gamma}\right)^{\beta-1}\right)$$

The scale parameter γ stands for how streched out the lifetime distribution is while the parameter β is the shape parameter which describes the rate of change of failure rate. Depending on β the failure rate is constant ($\beta = 1$), decreasing ($\beta < 1$) or increasing ($\beta > 1$). Out of these three different value ranges for β the much-used 'Bathtub' curve can be expressed with the Weibull distribution [25] [26].

For the design of the field node mainly industrial components are implemented. Even though the components are expected to have a long lifetime, a maintenance concept has to be set up. An internally performed calculation of the MTBFs of the critical components of the field node can be seen in Table 14. It contains the MTBF numbers provided by the manufacturers of the different components and the predicted effective MTBFs for the assembled system.

Assembly	Component MTBF	Duty cycle	Count	Redundancy	Effective MTBF	Note
PLC	8.4 a	1.0	1	none	8.4 a	5
24 V supply	31.0 a	1.0	5	4-out-of-5	14.0 a	6
Dehumidifier	6.8 a	0.2	1	non-critical	34.2 a	

Assembly	Fan L10	Duty cycle	Fan count	Redundancy	Effective MTBF[7]	Note
Cooling unit	35.0 a	1.0	$2+2$	two circuits	79.9 a	8
Fan tray	24.5 a	1.0	3	2-out-of-3	58.9 a	9

Table 14 Summary of manufacturer-provided component MTBFs and predicted effective MTBFs for assemblies.

For some of the component there is a redundancy while for others there is a deviating duty cycle to be considered. Those factors have an impact on the effective MTBF. A possible maintenance concept could be:

- consider the following assemblies as line-replaceable unit (LRUs): 230 V PDU, 24 V supply, PLC, I/O module, dehumidifier, fan tray, cooling unit fan
- operation continues unimpeded when any redundant unit fails (any single fan or 24 V supply)
- when redundancy is lost it will be fixed during the next field trip
- for fan failures[10] in particular:
  - *complete* fan trays are exchanged when one fan fails
  - *both* fans of a cooling circuit are exchanged when one fails

Rolling up the effective MTBFs there is conservatively estimated about one critical failure per field node every 4.5 years, with failure modes dominated by the PLC components and power supplies. These units should not be too difficult to replace if they are easily accessible. It has to be pointed out, however, that the estimates for these components are derived using a standard that is known to be very conservative, and assuming 100 % load. The actual average lifetime is probably significantly higher than the calculated one.

A Monte-Carlo simulation in which any critical failures are repaired next-day along with any outstanding non-critical repairs predicts an average availability of 50 field nodes of 99.98 % (equivalent to 99.2 % full-detector availability) over 10 years of operation, with an average of one action every two months and 3 repairs per action. On average, it can be assumed that the following number of spare parts is required:

- 60 PLC components
- 80 power supplies
- 15 dehumidifiers
- 4 cooling fans
- 8 fan trays

---

[5] incl. transceivers & I/O modules; MIL-HDBK-217F2, ground benign, 100 % load, 25 °C (incl. derating)

[6] MIL-HDBK-217F2, ground benign, 100 % load, 25 °C

[7] derived from Monte-Carlo assuming $\beta = 2.2$

[8] at 25 °C ambient temperature and 1500 RPM

[9] at 40 °C ambient temperature

[10] In contrast to electronics, fans mostly fail due to mechanical wear-out—hence one can reduce the number of trips into the field by exchanging fans of similar age once at it.

6.4 FIELD TEST IN PERU

The implementation of the DAQ node as described in the previous sections is mainly intended for a field test in Peru. There a full measurement chain with water tanks will be built up as a first prototype WCD. Several tasks are taken over by the participating Peruvian institutes, which are mainly related to infrastructure. The contribution of Max Planck Institute for Nuclear Physics covers the whole electronics system with its DAQ node and PMTs. The planned infrastructure includes a fenced area of 30 m × 30 m with three steel tanks, a solar array for power supply and a concrete plinth for the DAQ node.

The exact site is close to the towns called Yanque and Chivay, which are located in the district of Arequipa in southwestern Peru. This region is located in the Central Andes. While Yanque and Chivay lie at an altitude of approx. 3600 m asl, the actual test site is 25 km away and lies at 4800 m asl. This site provides a high altitude plateau of around 2 km^2 which would provide space for the whole detector array of SWGO (see Figure 57).

The environmental conditions that will be faced there include a maximum temperature range of approx. -20 °C to +20 °C whereby the average annual temperature is around 0 °C . The austral winter months from May to August are rather dry and snowfall appears to be rare. In Figure 58 the annual average daily temperature and rainfall is shown for the town Imata close to the acutal site. A weather station has recently been taken to the actual site but has no data available yet. The numbers from Imata can be used as a very good indication, as the external conditions are almost the same for both sites.

Figure 57 View from the nearby road into the open area of gravel and sand at the test side in Peru at an altitude of 4800 m. No infrastructure except for the nearby road available so far (Source Google Streetview 22.02.23).

A big campaign like the field test in Peru involves a lot of preparation work. Since there are the outdoor cabinet, 3 double PMTs, spare parts and tools that need to be shipped to the test site, many tasks have to be done in advance. The outdoor cabinet is planned to be shipped by sea freight due to its dimensions and weight of around 500 kg. Vibration-sensitive components

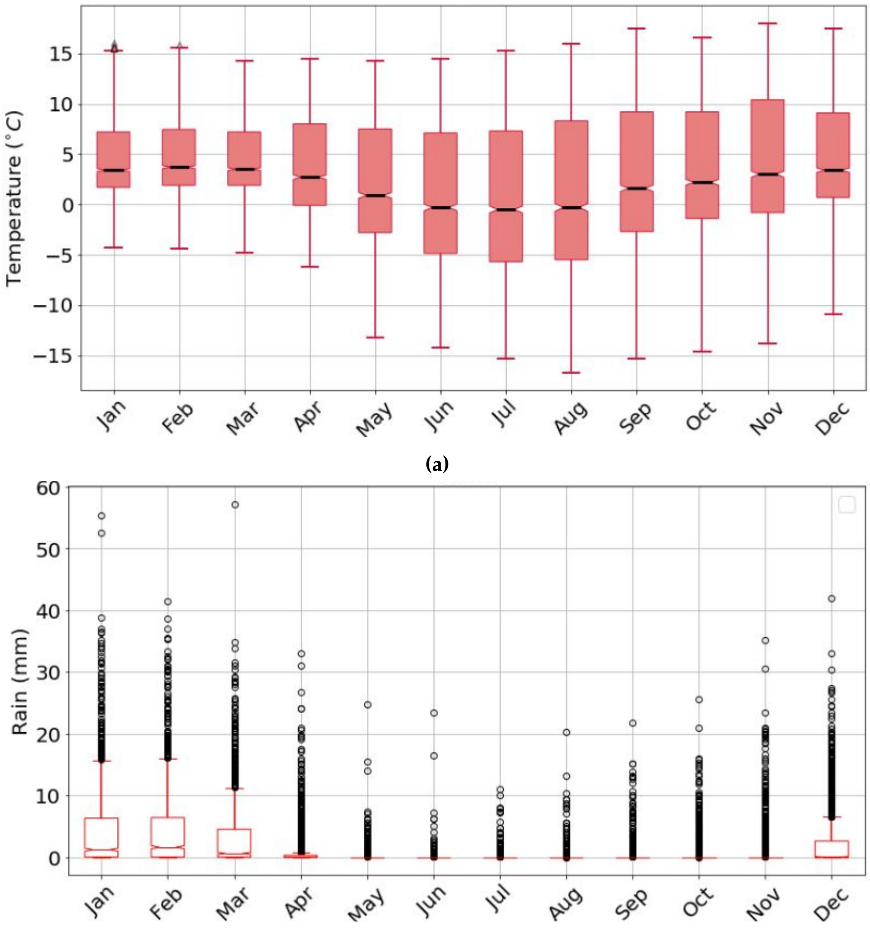

(a)

(b)

Figure 58 (a) The average temperature profile for the high-altitude plateau at Imata, Peru. (b) The average accumulated rainfall per day. Source: SWGO-internal site report

are removed from the cabinet, packed and sent separately. The free space in the cabinet is tried to be filled with less vulnerable parts such as cables or protective tubing. A wooden frame and a protective film around the cabinet should provide further protection against transport damage. The shipping duration by ship is assumed to be 8 weeks. The second part of the cargo will be the 3 boxes, filled with one double PMT each, the electronics like ADCs and PhantomHV units, and a toolbox. All these pieces will be transported on a standard pallet framed with a wooden box. This part of the cargo will be shipped by air freight to reduce the mechanical stress. The typical freight duration with customs is around two weeks but will be much more expensive compared to sea fright. The initial schedule for installation on the test site was planned for January 2023. As this could not be done due to the lack of infrastructure at the test site, the schedule has been postponed. Once the photovoltaic array is set up, the transport process from MPIK to Peru can be started. The delay is used to test the outdoor cabinet further in continuous operation for possible failures or abnormalities. Up to now (May 2023) the system runs without any problems.

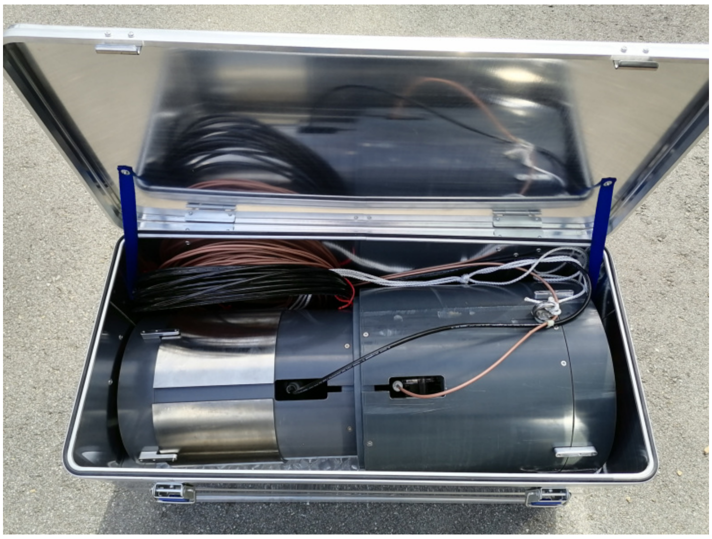

Figure 59 Fully assembled Double PMT in an aluminium transport box ready for shipment. On both ends it is equipped with clamped spacer rings for protecting the glass. The spaces in between will be filled with foam bags.

7

CONCLUSION

The work undertaken in this thesis can be divided into two subject areas. The development and evaluation of robust electronics for measuring Cherenkov light in gamma-ray detectors at high altitude and the design and prototyping of a low-maintenance field node for housing the measurement devices in a controlled environment. Together, this results in a proposal for a potential electronics measurement chain for the next generation gamma-ray observatory called SWGO(Southern Wide-field Gamma-ray Observatory):

- A modular multi-channel and high voltage generating device for the operation of photomultipliers has been developed. The use of electronics in cartridges simplifies installation and replacement, which is particularly advantageous for working at high altitude.
- Its functionality in combination with the 8-inch PMT R5912 from Hamamatsu has been proven. Different configurations have been tested and evaluated regarding charge and time resolution of signal pulses.
- A time resolution of less than 100 ps and a charge resolution below 10 % for an injected charge above 200 p.e. was reached.
- In order to increase the dynamic range of the measurement system, the option of having a controlled saturation of the shaping opamp has been worked out. This was achieved with a custom made opamp evaluation board. Making use of the controlled saturation leads to a dynamic range of sub p.e. up to 10,000 p.e.
- A cost-effective solution for getting PMTs waterproof and compatible with purified water has been shown. This allows the reuse of a large number of recovered PMTs for a potential engineering array.

The SWGO detectors will be spread over an area of around 1 km^2. The described concept requires clustering of about 200 PMT channels respectively 100 detector units per node. For this purpose, a prototype cabinet was developed that controls and houses the readout electronics under safe operating conditions in the field.

- A customised outdoor cabinet made of stainless steel with a earthquake reinforcement was developed together with an established manufacturer.
- To achieve acceptable operating conditions for the measurement equipment inside the field node an environmentally controlled system is provided. It includes a custom air-to-air heat exchanger, heater and a dehumidifier. The whole system is designed with the aim of being maintenance-free or at least low-maintenance with a focus on moving parts like the fan trays and the cooling unit.
- The power distribution as well as the control unit of the field node are installed in a separate control box called PAX. This allows the independent production and testing e.g. by technicians in the host country. Since almost all components are commercially available industrial components, they could be exchanged for other available components if required. This ensures future flexibility in production and maintenance.
- All these measures enable a self-controlled system aimed at preventing climatic stress and damage of the electronics. Based on different sensor readings an automatic grouping of the system into different operational states is done which leads to restricted use or even a shutdown of the system for safety reasons.

Due to the unique maturity of the electronics developed in this work the SWGO collaboration has recently decided to select this readout chain as a reference for developing and testing further prototype setups. Hence, several PhantomHV-based electronics chains from the next production batch are going to be prepared for use at Politecnico di Milano (Italy), Centro Brasileiro de Pesquisas Físicas (Brasil), and the HAWC detector array (Mexico). Fully-equipped field nodes are being prepared for deployment at candidate detector sites in South America.

A

SCHEMATIC OF THE OPAMP TESTBOARD

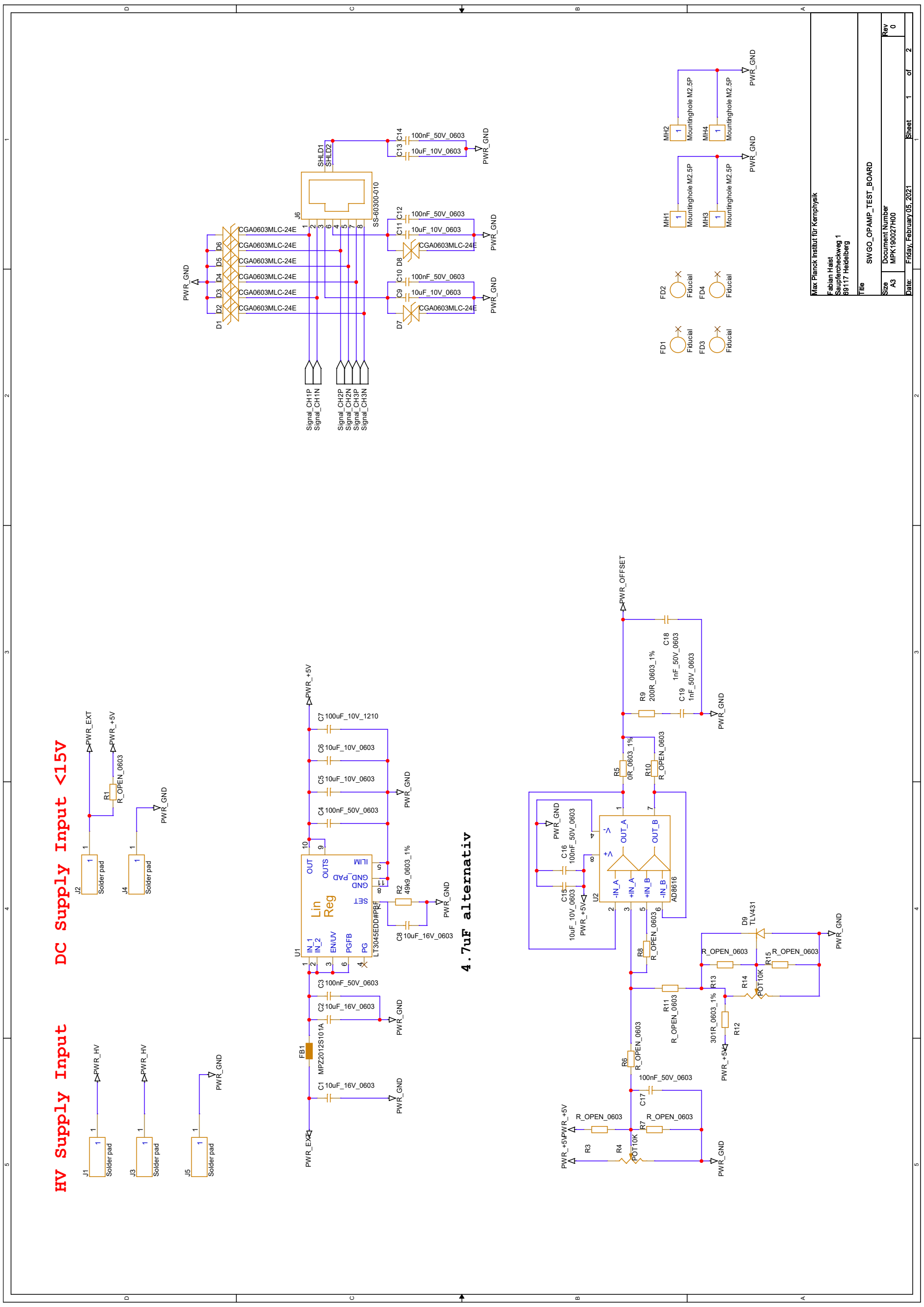

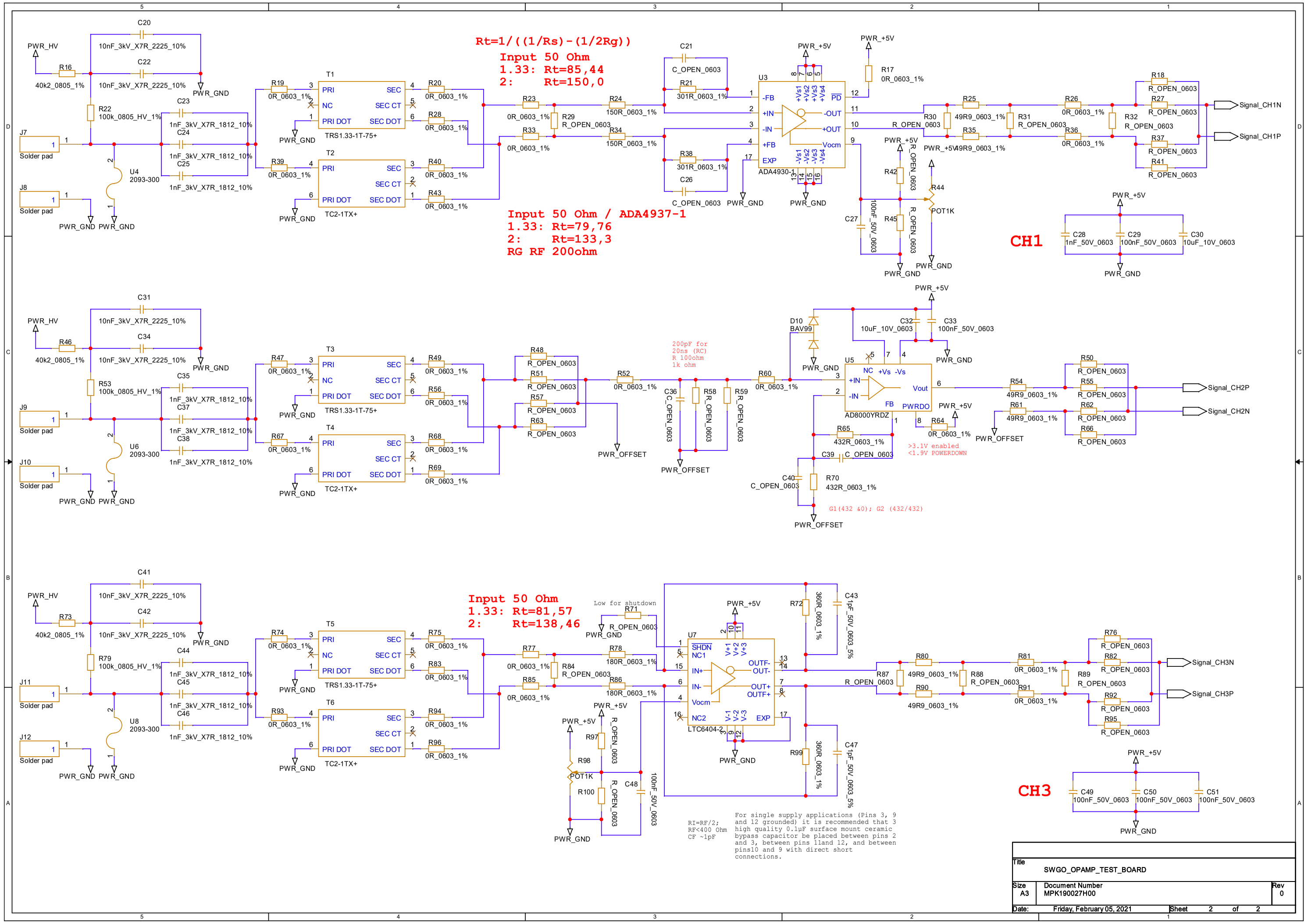
Rt=1/((1/Rs)-(1/2Rg))
Input 50 Ohm
1.33: Rt=85,44
2: Rt=150,0
Input 50 Ohm / ADA4937-1
1.33: Rt=79,76
2: Rt=133,3
RG RF 200ohm
CH1
200pF for 20ns (RC) R 100ohm 1k ohm
>3.1V enabled <1.9V POWERDOWN
G1(432 40); G2 (432/432)
Input 50 Ohm
1.33: Rt=81,57
2: Rt=138,46
Low for shutdown
CH3
RI=RF/2; RF<400 Ohm CF ~1pF
For single supply applications (Pins 3, 9 and 12 grounded) it is recommended that 3 high quality 0.1µF surface mount ceramic bypass capacitor be placed between pins 2 and 3, between pins 11and 12, and between pins10 and 9 with direct short connections.
U3 ADA4930-1
U5 AD8000YRDZ
U7 LTC6404-2
T1 TRS1.33-1T-75+
T2 TC2-1TX+
T3 TRS1.33-1T-75+
T4 TC2-1TX+
T5 TRS1.33-1T-75+
T6 TC2-1TX+
U4 2093-300
U6 2093-300
U8 2093-300
D10 BAV99
J7 Solder pad
J8 Solder pad
J9 Solder pad
J10 Solder pad
J11 Solder pad
J12 Solder pad
Signal_CH1N
Signal_CH1P
Signal_CH2P
Signal_CH2N
Signal_CH3N
Signal_CH3P
PWR_HV
PWR_+5V
PWR_GND
PWR_OFFSET
Title SWGO_OPAMP_TEST_BOARD
Size A3
Document Number MPK190027H00
Rev 0
Date: Friday, February 05, 2021
Sheet 2 of 2

B

SCHEMATIC OF THE PHANTOMHV PICK-OFF CIRCUIT

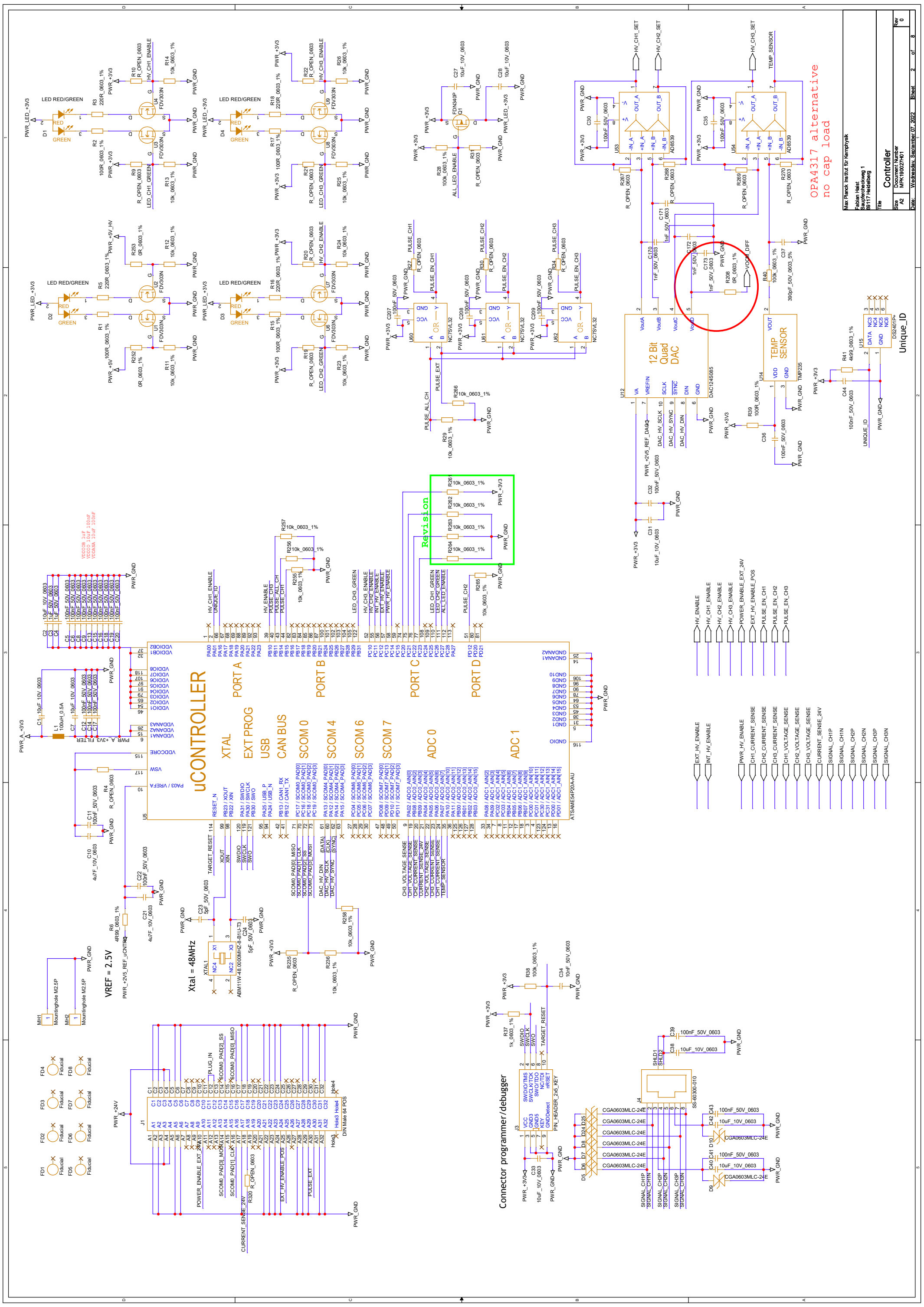
uCONTROLLER
PORT A
PORT B
PORT C
PORT D
XTAL
EXT PROG
USB
CAN BUS
SCOM 0
SCOM 4
SCOM 6
SCOM 7
ADC 0
ADC 1
12 Bit Quad DAC
TEMP SENSOR
Unique_ID
Connector programmer/debugger
Xtal = 48MHz
VREF = 2,5V
Revision
OPA4317 alternative
no cap load
Max Planck Institut für Kernphysik
Fabian Haist
Saupfercheckweg 1
69117 Heidelberg
Title
Controller
Size
A2
Document Number
MPK1900027H01
Rev
0
Date:
Wednesday, September 07, 2022
Sheet
2
of
8

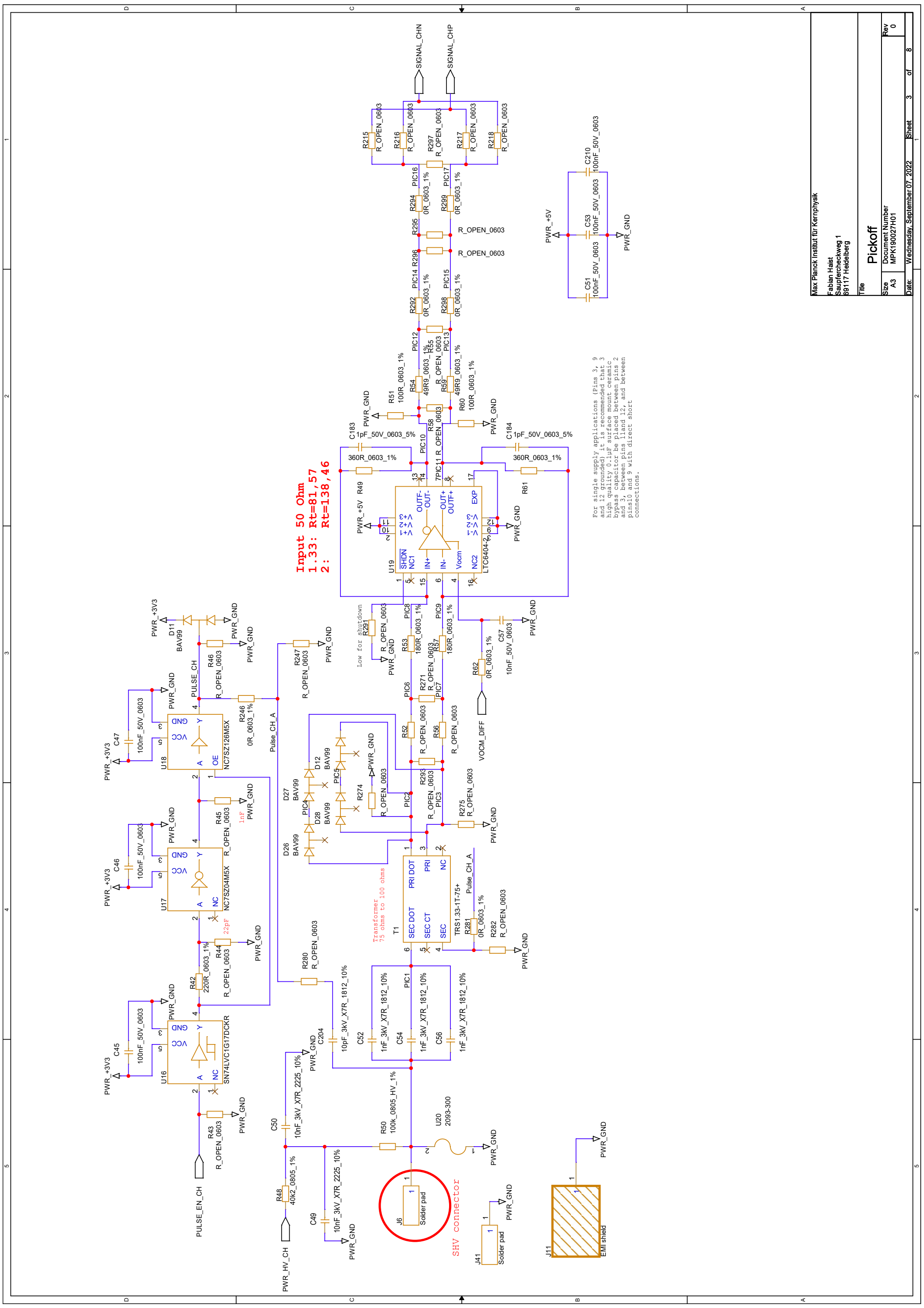
SIGNAL_CHN
SIGNAL_CHP
R215 R_OPEN_0603
R216 R_OPEN_0603
R297 R_OPEN_0603
R217 R_OPEN_0603
R218 R_OPEN_0603
PIC16
PIC17
R294 0R_0603_1%
R299 0R_0603_1%
R295 R_OPEN_0603
R296 R_OPEN_0603
PIC14
PIC15
R292 0R_0603_1%
R298 0R_0603_1%
PIC12
PIC13
R55 R_OPEN_0603
R51 100R_0603_1%
R54 49R9_0603_1%
R57 49R9_0603_1%
R60 100R_0603_1%
R58 R_OPEN_0603
PWR_GND
C183 1pF_50V_0603_5%
C184 1pF_50V_0603_5%
360R_0603_1%
R49
R61
PIC10
PIC11
Input 50 Ohm
1.33: Rt=81,57
2: Rt=138,46
PWR_+5V
U19
LTC6404-2
SHDN NC1 IN+ IN- Vocm NC2
OUT- OUT- OUT+ OUT+ EXP
V+1 V+2 V+3 V-1 V-2 V-3
For single supply applications (Pins 3, 9 and 12 grounded) it is recommended that 3 high quality 0.1µF surface mount ceramic bypass capacitor be placed between pins 2 and 3, between pins 11and 12, and between pins10 and 9 with direct short connections.
PWR_+5V
C51 100nF_50V_0603
C53 100nF_50V_0603
C210 100nF_50V_0603
Max Planck Institut für Kernphysik
Fabian Haist
Saupfercheckweg 1
69117 Heidelberg
Title
Pickoff
Size A3
Document Number MPK190027H01
Rev 0
Date: Wednesday, September 07, 2022
Sheet 3 of 8
Low for shutdown
R281 R_OPEN_0603
R53 180R_0603_1%
R52 180R_0603_1%
PIC8
PIC9
C57 10nF_50V_0603
R62 0R_0603_1%
VOCM_DIFF
R271 R_OPEN_0603
PIC6
PIC7
R52 R_OPEN_0603
R56 R_OPEN_0603
R293 R_OPEN_0603
R274 R_OPEN_0603
R275 R_OPEN_0603
PIC2
PIC3
PIC4
PIC5
D12 BAV99
D26 BAV99
D27 BAV99
D28 BAV99
T1
TRS1.33-1T-75+
PRI DOT PRI NC
SEC DOT SEC CT SEC
Transformer 75 ohms to 100 ohms
Pulse_CH_A
R281 0R_0603_1%
R282 R_OPEN_0603
C52 1nF_3kV_X7R_1812_10%
C54 1nF_3kV_X7R_1812_10%
C56 1nF_3kV_X7R_1812_10%
PIC1
C204 10pF_3kV_X7R_1812_10%
R280 R_OPEN_0603
R247 R_OPEN_0603
R246 0R_0603_1%
Pulse_CH_A
C50 10nF_3kV_X7R_2225_10%
R50 100k_0805_HV_1%
U20 2093-300
R48 40k2_0805_1%
C49 10nF_3kV_X7R_2225_10%
PWR_HV_CH
J6 Solder pad
SHV connector
J41 Solder pad
J11 EMI shield
PWR_+3V3
D11 BAV99
R46 R_OPEN_0603
PULSE_CH
U18 NC7SZ126M5X
VCC GND A Y OE
C47 100nF_50V_0603
U17 NC7SZ04M5X
VCC GND A Y NC
C46 100nF_50V_0603
R45 R_OPEN_0603
1nF
R44 R_OPEN_0603
22pF
R42 220R_0603_1%
U16 SN74LVC1G17DCKR
VCC GND A Y NC
C45 100nF_50V_0603
R43 R_OPEN_0603
PULSE_EN_CH
A B C D
1 2 3 4 5

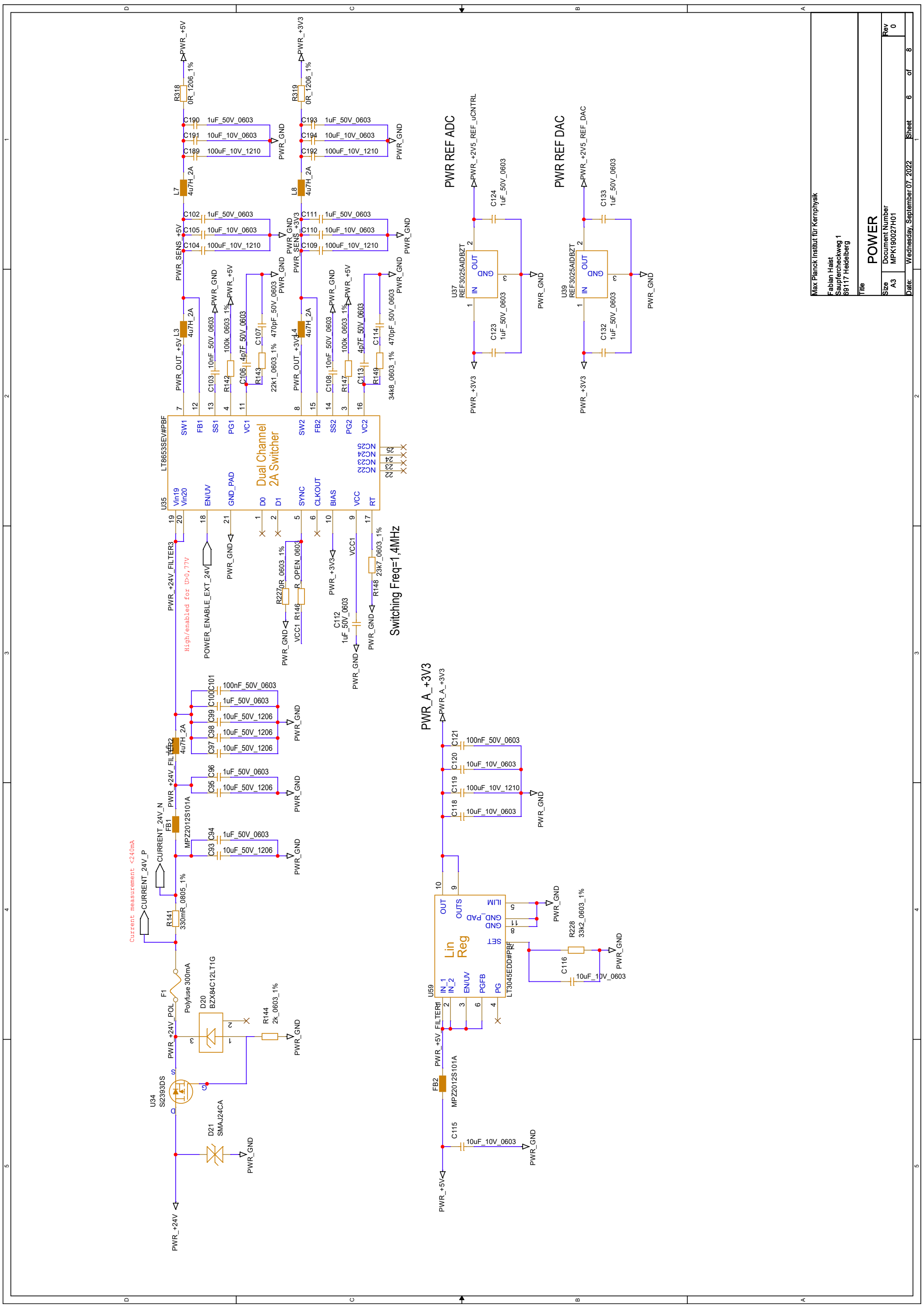
PWR_+24V
D21
SMAJ24CA
U34
SI2393DS
PWR_+24V_POL
F1
Polyfuse 300mA
D20
BZX84C12LT1G
R144
2k_0603_1%
R141
330mR_0805_1%
CURRENT_24V_P
CURRENT_24V_N
Current measurement <240mA
FB1
MPZ2012S101A
PWR_+24V_FILTER1
C93 10uF_50V_1206
C94 1uF_50V_0603
C95 10uF_50V_1206
C96 1uF_50V_0603
L2
4u7H_2A
PWR_+24V_FILTER2
C97 10uF_50V_1206
C98 10uF_50V_1206
C99 10uF_50V_1206
C100 1uF_50V_0603
C101 100nF_50V_0603
PWR_+24V_FILTER3
High/enabled for U>0,77V
POWER_ENABLE_EXT_24V
PWR_GND
U35
LT8653SEV#PBF
Dual Channel
2A Switcher
Vin19
Vin20
EN/UV
GND_PAD
D0
D1
SYNC
CLKOUT
BIAS
VCC
RT
SW1
FB1
SS1
PG1
VC1
SW2
FB2
SS2
PG2
VC2
NC22
NC23
NC24
NC25
R227 0R_0603_1%
R146 R_OPEN_0603
VCC1
PWR_+3V3
C112
1uF_50V_0603
R148 23k7_0603_1%
Switching Freq=1,4MHz
PWR_OUT_+5V
L3
4u7H_2A
C103 10nF_50V_0603
R142 100k_0603_1%
C106 4p7F_50V_0603
R143 22k1_0603_1%
C107 470pF_50V_0603
PWR_SENS_+5V
C102 1uF_50V_0603
C105 10uF_10V_0603
C104 100uF_10V_1210
L7
4u7H_2A
C190 1uF_50V_0603
C191 10uF_10V_0603
C189 100uF_10V_1210
R318
0R_1206_1%
PWR_+5V
PWR_OUT_+3V3
L4
4u7H_2A
C108 10nF_50V_0603
R147 100k_0603_1%
C113 4p7F_50V_0603
R149 34k8_0603_1%
C114 470pF_50V_0603
PWR_SENS_+3V3
C111 1uF_50V_0603
C110 10uF_10V_0603
C109 100uF_10V_1210
L8
4u7H_2A
C193 1uF_50V_0603
C194 10uF_10V_0603
C192 100uF_10V_1210
R319
0R_1206_1%
PWR_+3V3
PWR REF ADC
PWR_+2V5_REF_uCNTRL
U37
REF3025AIDBZT
IN
OUT
GND
C124 1uF_50V_0603
C123 1uF_50V_0603
PWR REF DAC
PWR_+2V5_REF_DAC
U39
REF3025AIDBZT
C133 1uF_50V_0603
C132 1uF_50V_0603
PWR_+5V
FB2
MPZ2012S101A
C115 10uF_10V_0603
PWR_+5V_FILTER
U59
LT3045EDD#PBF
Lin
Reg
IN_1
IN_2
EN/UV
PGFB
PG
OUT
OUTS
ILIM
GND_PAD
GND
SET
R228 33k2_0603_1%
C116 10uF_10V_0603
PWR_A_+3V3
C118 10uF_10V_0603
C119 100uF_10V_1210
C120 10uF_10V_0603
C121 100nF_50V_0603
Max Planck Institut für Kernphysik
Fabian Haist
Saupfercheckweg 1
69117 Heidelberg
Title
POWER
Size A3
Document Number MPK190027H01
Rev 0
Date: Wednesday, September 07, 2022
Sheet 6 of 8

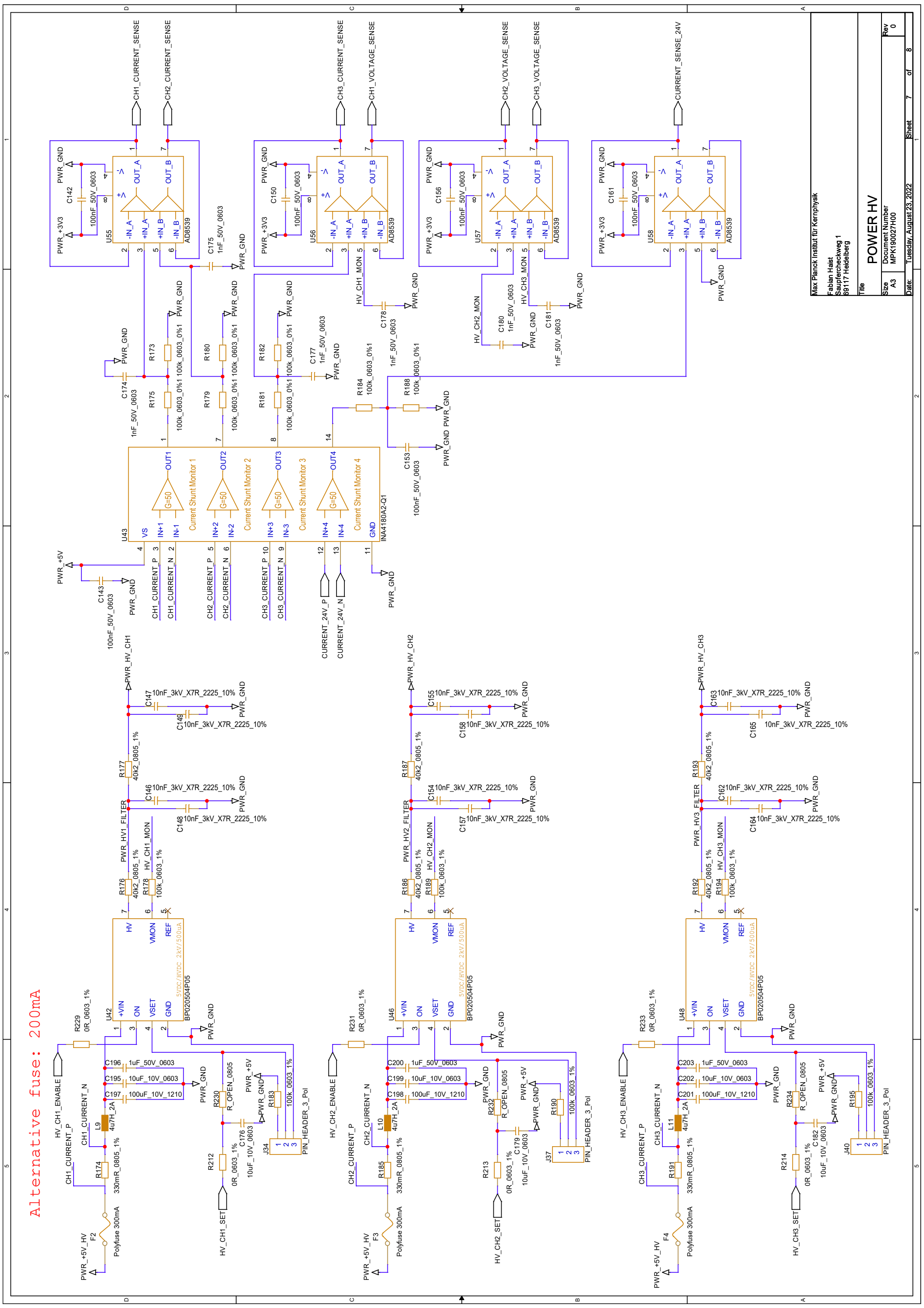
CH1_CURRENT_SENSE
CH2_CURRENT_SENSE
CH3_CURRENT_SENSE
CH1_VOLTAGE_SENSE
CH2_VOLTAGE_SENSE
CH3_VOLTAGE_SENSE
CURRENT_SENSE_24V
AD8539
U55
U56
U57
U58
PWR_GND
PWR_+3V3
100nF_50V_0603
1nF_50V_0603
100k_0603_0%1
HV_CH1_MON
HV_CH2_MON
HV_CH3_MON
U43
INA4180A2-Q1
Current Shunt Monitor 1
Current Shunt Monitor 2
Current Shunt Monitor 3
Current Shunt Monitor 4
G=50
PWR_+5V
CH1_CURRENT_P
CH1_CURRENT_N
CH2_CURRENT_P
CH2_CURRENT_N
CH3_CURRENT_P
CH3_CURRENT_N
CURRENT_24V_P
CURRENT_24V_N
PWR_HV_CH1
PWR_HV_CH2
PWR_HV_CH3
10nF_3kV_X7R_2225_10%
40k2_0805_1%
PWR_HV1_FILTER
PWR_HV2_FILTER
PWR_HV3_FILTER
BP020504P05
U42
U46
U48
HV
VMON
REF
+VIN
ON
VSET
GND
HV_CH1_ENABLE
HV_CH2_ENABLE
HV_CH3_ENABLE
HV_CH1_SET
HV_CH2_SET
HV_CH3_SET
1uF_50V_0603
10uF_10V_0603
100uF_10V_1210
4u7H_2A
330mR_0805_1%
Polyfuse 300mA
PWR_+5V_HV
R_OPEN_0805
0R_0603_1%
PIN_HEADER_3_Pol
J34
J37
J40
Alternative fuse: 200mA
Max Planck Institut für Kernphysik
Fabian Hast
Saupfercheckweg 1
69117 Heidelberg
Title
POWER HV
Size
A3
Document Number
MPK190027H00
Rev
0
Date: Tuesday, August 23, 2022
Sheet 7 of 8

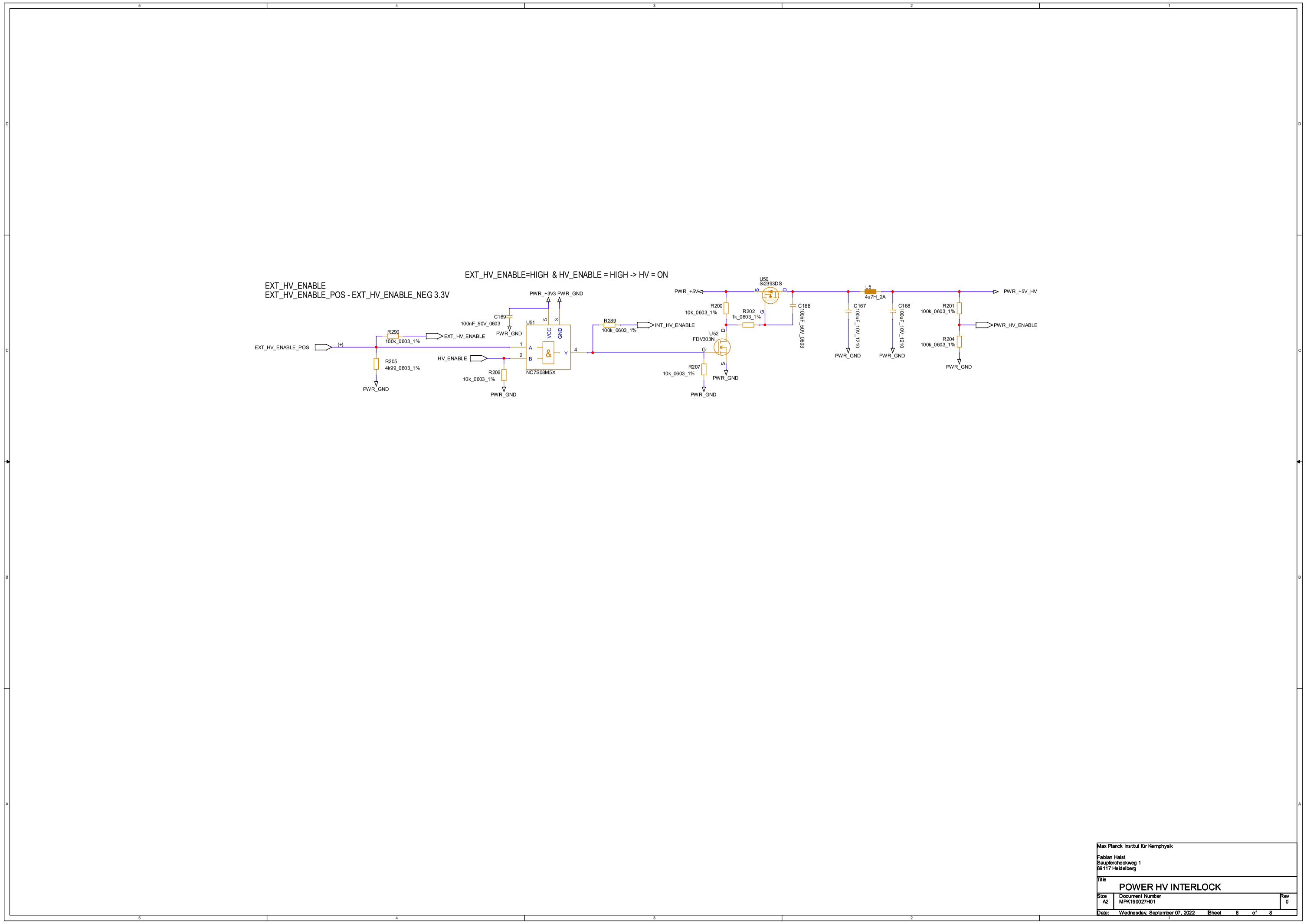
EXT_HV_ENABLE
EXT_HV_ENABLE_POS - EXT_HV_ENABLE_NEG 3.3V
EXT_HV_ENABLE=HIGH & HV_ENABLE = HIGH -> HV = ON
EXT_HV_ENABLE_POS
{+}
R290
100k_0603_1%
EXT_HV_ENABLE
R205
4k99_0603_1%
PWR_GND
C169
100nF_50V_0603
PWR_GND
PWR_+3V3
PWR_GND
U51
VCC
GND
5
3
1
2
4
A
B
&
Y
NC7S08M5X
HV_ENABLE
R206
10k_0603_1%
PWR_GND
R289
100k_0603_1%
INT_HV_ENABLE
R207
10k_0603_1%
PWR_GND
PWR_+5V
R200
10k_0603_1%
U52
FDV303N
G
D
S
PWR_GND
U50
Si2393DS
S
D
G
R202
1k_0603_1%
C166
100nF_50V_0603
C167
100uF_10V_1210
PWR_GND
L5
4u7H_2A
C168
100uF_10V_1210
PWR_GND
R201
100k_0603_1%
R204
100k_0603_1%
PWR_GND
PWR_+5V_HV
PWR_HV_ENABLE
Max Planck Institut für Kernphysik
Fabian Haist
Saupfercheckweg 1
69117 Heidelberg
Title
POWER HV INTERLOCK
Size
A2
Document Number
MPK190027H01
Rev
0
Date:
Wednesday, September 07, 2022
Sheet
8
of
8
1
2
3
4
5
A
B
C
D

C

SIGNAL ANALYSIS ALGORITHM FOR FLASHCAM

A pulse generator triggers both the laser and the FlashCam ADC readout. For this, the generator's signal is filtered with a 10 MHz low-pass (to remove most of the frequency contents above the Nyquist frequency of the FlashCam ADC) and split passively.

To recover the phase between the uncoupled ADC clock and pulse generator clock, the sampled trigger signal is upsampled by a factor of 32 to a time base of 125 ps. The most simple method to reconstruct the phase is then to find the time bin in which the upsampeled signal crosses a given threshold.

This recovered phase is now used to sort the PMT waveform samples into 125 ps time bins. If sufficient statistics are collected within each time bin, an average amplitude profile of the PMT waveform can be generated with a time resolution of 125 ps. Pulse-to-pulse variations of the PMT are averaged out.

This method is mainly limited by:

- the jitter between the ADCs that sample the trigger and PMT signals (better than 30 ps RMS for FlashCam)
- the jitter between the laser trigger and the actual production of the light pulse (10 ps)
- the pulse shape stability of the signal generator

The main advantage of this method compared to using a dedicated high-sampling rate digitiser (e.g., an oscilloscope) is that the final signal path (including ADC frontend) is used; thus, no additional systematic uncertainties are being introduced.

REFERENCES

[1] D. Bose et al. “Galactic and extragalactic sources of very high energy gamma rays”. In: *The European Physical Journal Special Topics* 231.1 (2022), pp. 27–66. DOI: 10.1140/epjs/s11734-022-00434-8.

[2] C. Grupen. *Astroparticle Physics*. Springer, 2005, p. 441. ISBN: 978-3-540-25312-9.

[3] R. M. Ulrich. “Measurement of the proton-air cross section using hybrid data of the PierreAuger Observatory”. PhD thesis. Universität Karlsruhe (TH), 2008.

[4] S. Pürckhauer. “Characterising light concentrators for CTA and optimising the data selection to improve angular resolution and sensitivity”. PhD thesis. University of Heidelberg, 2018.

[5] S. N. Ahmed. *Physics and Engineering of Radiation Detection*. Elsevier Science and Technology Books, 2015, p. 784. ISBN: 9780128013632. DOI: 10.1016/c2013-0-15270-1.

[6] R. J. Lauer. “Gamma-Ray Astronomy with the HAWC Observatory”. In: *International Journal of Modern Physics: Conference Series* 28 (2014), p. 1460185. DOI: 10.1142/s2010194514601859.

[7] X.-H. Ma et al. “Chapter 1 LHAASO Instruments and Detector technology”. In: *Chinese Physics C* 46.3 (2022), p. 030001. DOI: 10.1088/1674-1137/ac3fa6.

[8] The Pierre Auger Collaboration. “The Pierre Auger Cosmic Ray Observatory”. In: *Nuclear Instruments and Methods in Physics Research A, 798 (2015) 172-213* 798 (Feb. 4, 2015), pp. 172–213. DOI: 10.1016/j.nima.2015.06.058. arXiv: 1502.01323 [astro-ph.IM].

[9] Jim Hinton on behalf of the SWGO Collaboration. “The Southern Wide-field Gamma-ray Observatory: Status and Prospects”. In: *PoS(ICRC2021) 023* (Nov. 2021). DOI: 10.48550/ARXIV.2111.13158. arXiv: 2111.13158 [astro-ph.IM].

[10] Felix Werner and Lukas Nellen on behalf of the SWGO Collaboration. “Technological options for the Southern Wide-field Gamma-ray Observatory (SWGO) and current design status”. In: *PoS(ICRC2021)714*. 2021. DOI: 10.22323/1.395.0714.

[11] A. Aab et al. “Spectral calibration of the fluorescence telescopes of the Pierre Auger Observatory”. In: *Astroparticle Physics* 95 (2017), pp. 44–56. DOI: 10.1016/j.astropartphys.2017.09.001.

[12] S. Kunwar et al. “A double-layered Water Cherenkov Detector array for Gamma-ray astronomy”. In: *Nuclear Instruments and Methods in Physics Research Section A: Accelerators, Spectrometers, Detectors and Associated Equipment* 1050 (2023), p. 168138. DOI: `10.1016/j.nima.2023.168138`.

[13] Hamamatsu Photonics K.K. *Photomultiplier Tubes: Basics and Applications*. Tech. rep. 2007. URL: `https://www.hamamatsu.com/content/dam/hamamatsu-photonics/sites/documents/99_SALES_LIBRARY/etd/PMT_handbook_v3aE.pdf`.

[14] B. K. Lubsandorzhiev et al. “Photoelectron backscattering in vacuum phototubes”. In: *Nucl.Instrum.Meth. A567 (2006) 12-16* 567.1 (Jan. 20, 2006), pp. 12–16. DOI: `10.1016/j.nima.2006.05.047`. arXiv: `physics/0601157 [physics.ins-det]`.

[15] F. Werner et al. “Performance Verification of the FlashCam Prototype Camera for the Cherenkov Telescope Array”. In: *Nuclear Instruments and Methods in Physics Research Section A: Accelerators, Spectrometers, Detectors and Associated Equipment* 876 (Dec. 30, 2016), pp. 31–34. DOI: `10.1016/j.nima.2016.12.056`. arXiv: `1612.09528 [astro-ph.IM]`.

[16] Linear Technology. *LTC6404 600MHz, Low Noise,High Precision Fully DifferentialInput/Output Amplifier/Driver*. Accessed on 10-04-2023. URL: `https://www.analog.com/media/en/technical-documentation/data-sheets/6404f.pdf`.

[17] Analog Devices, Inc. *ADA4930-1/ADA4930-2 Ultralow NoiseDrivers for Low Voltage ADCs*. Rev. D. Accessed on 11-04-2023. URL: `https://www.analog.com/media/en/technical-documentation/data-sheets/ADA4930-1_4930-2.pdf`.

[18] Analog Devices, Inc. *AD8000 1.5 GHz, Ultrahigh Speed Op Amp*. Rev. C. Accessed on 11-04-2023. URL: `https://www.analog.com/media/en/technical-documentation/data-sheets/ad8000.pdf`.

[19] R. Arora and W. Mosch. *High Voltage Insulation Engineering. Behaviour of Dielectrics - Their Properties and Applications*. Wiley Eastern Limited, 2008. ISBN: 9788122406191.

[20] J. Hu et al. “Enhanced Gate Driver Design for SiC-Based Generator Rectifier Unit for Airborne Applications”. In: *2021 IEEE Applied Power Electronics Conference and Exposition (APEC)*. IEEE, 2021. DOI: `10.1109/apec42165.2021.9487425`.

[21] The Dow Chemical Company. *DOWSIL™ 3145 RTV MIL-A-46146 Adhesive Sealant -Clear*. Accessed on 10-05-2023. URL: `https://www.dow.com/en-us/document-viewer.html?docPath=/content/dam/dcc/documents/en-us/productdatasheet/11/11-32/11-3215-01-dowsil-3145-rtv-mil-a-46146-adhesive.pdf`.

[22] Wacker Chemie AG. *ELASTOSIL® RT 625 A/B. Room Temperature Curing Silicone Rubber (RTV-2)*. Accessed on 10-05-2023. URL: `https://www.wacker.com/h/de-gb/medias/ELASTOSIL-RT-625-AB-en-2022.02.23.pdf`.

[23] F. An et al. “The muon system of the Daya Bay Reactor antineutrino experiment”. In: *Nuclear Instruments and Methods in Physics Research Section A: Accelerators, Spectrometers, Detectors and Associated Equipment* 773 (2015), pp. 8–20. DOI: `10.1016/j.nima.2014.09.070`.

[24] İ. Baylakoğlu et al. “The detrimental effects of water on electronic devices”. In: *e-Prime - Advances in Electrical Engineering, Electronics and Energy* 1 (2021), p. 100016. DOI: `10.1016/j.prime.2021.100016`.

[25] R. D. Leitch. *Basic Reliability Engineering Analysis Butterworths Basic Series. Butterworths Basic Series*. Elsevier Science and Technology Books, 2013. ISBN: 9781483135632.

[26] D. J. Smith. *Reliability, Maintainability and Risk*. Newnes, 2001, p. 370. ISBN: 9780750651684.

LIST OF PUBLICATIONS

[1] Jim Hinton on behalf of the SWGO Collaboration. "The Southern Wide-field Gamma-ray Observatory: Status and Prospects". In: *PoS(ICRC2021) 023* (Nov. 2021). DOI: 10.48550/ARXIV.2111.13158. arXiv: 2111.13158 [astro-ph.IM].

[2] Ruben Conceição for the SWGO Collaboration. "The Southern Wide-field Gamma-ray Observatory". In: *PoS(ICRC2023)963*. 2023. URL: https://pos.sissa.it/444/963/pdf.

[3] Pat Harding for the SWGO Collaboration. "Beyond the Standard Model with the Southern Wide-field Gamma-ray Observatory". In: *PoS(ICRC2023)1399*. 2023. DOI: 10.22323/1.444.1399.

[4] Jose Bellido on behalf of the SWGO Collaboration. "Manufacture Details of a SWGO Double-Layer Tank Design - Water Cherenkov Detector Prototype". In: *PoS(ICRC2023)803*. 2023. DOI: 10.22323/1.444.0803.

[5] U. Barres de Almeida, G. Giacinti, F. Longo on behalf of the SWGO collaboration. "Benchmarking the Science for the Southern Wide-Field Gamma-ray Observatory (SWGO)". In: *PoS(ICRC2021)893*. 2021. DOI: https://doi.org/10.22323/1.395.0893.

[6] Hazal Goksu for the SWGO Collaboration. "Updates on Lake Deployment of Southern Wide-field Gamma-ray Observatory (SWGO) Detector Units". In: *PoS(ICRC2023)653*. 2023. DOI: 10.22323/1.444.0653.

[7] F. Leitl; V. Joshi and S. Funk for the SWGO Collaboration. "Status of the SWGO air shower reconstruction using a template-based likelihood method". In: *PoS(ICRC2023)593*. 2023. DOI: 10.22323/1.444.0593.

[8] S.D. Quispe Mamani, A.A. Baldárrago Alcántara, Rolando Perca, Christian Levita, Raul Yanyachi, Luis Otiniano, Juan Vega, Sayri Garcia, Sandro Arias, Jose Bellido, Hazal Göksu and Werner Hofmann for the SWGO Collaboration. "Low-cost Oceanographic Buoy for Evaluating the Mechanical Resistance of a Water Cherenkov Detector to be deployed on a high-altitude Natural Lake in Peru." In: *PoS(ICRC2023)614*. 2023. DOI: 10.22323/1.444.0614.

[9] Felix Werner and Lukas Nellen on behalf of the SWGO Collaboration. "Technological options for the Southern Wide-field Gamma-ray Observatory (SWGO) and current design status". In: *PoS(ICRC2021)714*. 2021. DOI: 10.22323/1.395.0714.